SLAC-266
HEPL-937
UC-34D
(E)

SEARCH FOR CHARMED F MESONS IN e^+e^- COLLISIONS WITH THE CRYSTAL BALL*

Roland Paul Horisberger

Stanford Linear Accelerator Center
Stanford University
Stanford, California 94305

January 1984

Prepared for the Department of Energy

under contract number DE-AC03-76SF00515

Printed in the United States of America. Available from the National Technical Information Service, U.S. Department of Commerce, 5285 Port Royal Road, Springfield, Virginia 22161. Price: Printed Copy A08, Microfiche A01.

* Ph.D. dissertation.

ABSTRACT

In this work an experimental search for the production of the charmed F and F^* mesons in e^+e^- collisions is presented. The data for this analysis were obtained over a center of mass energy region from 3.86 GeV to 4.5 GeV with the Crystal Ball detector at SPEAR. The inclusive η production cross section has been measured as a function of the center of mass energy . It was found to be almost constant with no indication for an significant increase which was cited as evidence for F production by a previous experiment . A search for $F\overline{F}$, $F^*\overline{F}$ and $F^*\overline{F}^*$ production with the decay $F^\pm \rightarrow \eta\pi^\pm$ has also been made, but no signal was observed. Upper limits for $\sigma_{F^{(*)}\overline{F}^{(*)}} \cdot BR(F^\pm \rightarrow \eta\pi^\pm)$ are given for various F and F^* masses. The measurements presented here are inconsistent with results from earlier experiments which had been used to establish the existence of the F mesons. The inclusive γ spectrum at $E_{cm} = 4.33$ GeV has also been used to obtain upper limits on F^* production . These results disagree with theoretical expectations for the $F^*\overline{F}^*$ production cross section for the F and F^* masses quoted by other experiments. In connection with this analysis the cross section for D^* production was also measured at $E_{cm} = 4.33$ GeV and was found to be $7.4nb \pm 1.1nb \pm 1.3nb$.

ACKNOWLEDGEMENTS

My sincerest thanks go to my advisor Robert Hofstadter for his most encouraging support and advice throughout the years of my graduate work. It was through his encouragement that I was able to attend the Graduate Program in Physics at Stanford University and participate in the Crystal Ball experiment. Having been part of the Crystal Ball collaboration was a great experience for me and I would like to thank each member of the group for all their efforts and contributions to the experiment that made this whole team effort so successful:

C.Edwards , R. Partridge , C. Peck , F. C. Porter , P. Ratoff , (Caltech); D. Antreasyan, Y. F. Gu, J. Irion, W. Kollman, M. Richardson , K. Strauch, K. Wacker , A. Weinstein (Harvard); D. Aschman, T. Burnett , M. Cavalli-Sforza , R. Cowan , D. Coyne , M. Joy , C. Newmann , H. Sadrozinski (Princeton); D. Gelphman , R. Hofstadter , I. Kirkbride , H. Kolanoski , K. Koenigsmann , R. Lee , A. Liberman , J. O'Reilly, A. Osterheld , B. Pollock , J. Tompkins (Stanford); E. Bloom , F. Bulos , R. Chestnut , G. Godfrey , J. Gaiser , C. Kiesling , S. Leffler , W. Lockman, S. Lowe , M. Oreglia , D. Scharre (SLAC).

I would especially like to thank John Tompkins whose experience and whose suggestions have been of great value to me. Also special thanks for the many fruitful discussions I had with all the other people who were somewhat closer related with this analysis project: Frank Porter , Don Coyne , Hartmut Sadrozinski and Brian Pollock .

I am very thankful to my wife Kathy for supporting me in this effort through all its stages and for proofreading the manuscript. Finally ,many thanks go to my parents who always encouraged me in my interests.

Table of Contents

List of Figures

List of Tables

Chapter 1

PHYSICS OF CHARMED MESONS

§1.1 BRIEF REVIEW OF CHARM

In this section I would like to review a few of the major ideas of modern weak interaction theory of heavy quarks which I think are of importance for an experimental search for the charmed F meson. For details the reader shall be referred to other more complete sources.[1]

Charm was first introduced by Bjorken and Glashow[2] for reasons of symmetry between quarks and leptons in weak interactions. Later Glashow-Iliopoulos-Maiani (GIM)[3] carried the idea further and put the charmed quark together with the strange quark in a I-spin doublet which is rotated in weak isospin space.

$$q_1 = \begin{pmatrix} u \\ d' \end{pmatrix}, \; q_2 = \begin{pmatrix} c \\ s' \end{pmatrix} \tag{1.1}$$

with

$$d' = d \cdot \cos\theta_c + s \cdot \sin\theta_c \tag{1.2}$$

$$s' = -d \cdot \sin\theta_c + s \cdot \cos\theta_c \tag{1.3}$$

---

[1] SLAC Summer Institute 1980 THE WEAK INTERACTION

[2] J.D. Bjorken, S.L. Glashow, Phys. Lett. 11 (1964) 255.

[3] S.L. Glashow, J. Iliopoulos, L. Maiani, Phys. Rev. D2 (1970) 1285.

and the Cabibbo angle $\theta_c = 13.2 \pm .7^0$. This naturally explained the experimental smallness of strangeness changing weak neutral currents.

The charged hadronic weak current then has the form

$$j^{\mu}_{h\pm} = \sum_{i=1}^{2} \overline{q}_i \gamma^{\mu}(1-\gamma_5) T_{\pm} q_i \tag{1.4}$$

Where $(1-\gamma_5)$ projects out the left handed components of the quark fields and $T_{\pm}$ are the Pauli raising and lowering matrices. The charged leptonic weak current has the same form but having l_i instead of q_i

$$l_1 = \begin{pmatrix} \nu_e \\ e^- \end{pmatrix}, \; l_2 = \begin{pmatrix} \nu_\mu \\ \mu^- \end{pmatrix} \tag{1.5}$$

In 1975 , Perl[4] established the existence of the charged τ lepton with its presumably neutral ν_τ. This lepton doublet together with another quark doublet , containing the established b quark and the not yet found t quark ,complicates the scheme slightly by having four different mixing angles[5] instead of the Cabibbo angle θ_c . Only the τ leptons are of importance here since their masses allow them to appear in semileptonic decays of the charmed mesons , whereas the b quark and t quark can only manifest themselves in higher order loop corrections.

The discovery of the J/ψ in 1974 with its interpretation as a $c\bar{c}$ system provided the first strong experimental evidence for charm. The heavy mass of the c quark ($m_c \approx 1.8\,\mathrm{GeV}$) allowed the application of nonrelativistic potential models to the $c\bar{c}$ system. These calculations matched nicely with the masses of further excited states of the $c\bar{c}$ system which where subsequently discovered.

Open charmed mesons ($C = \pm 1$) are formed by binding a c quark together with any of the light quarks $\overline{u}, \overline{d}, \overline{s}$ .These D^0, D^+, F^+ mesons enlarge the "old" pseudoscalar meson octet $J^P = 0^-$ to a hexadecimet as shown in Figure 1. The D^+ and D^0 form a I-spin doublet , whereas the F^+ is a I-spin singlet. The vector meson octet $J^P = 1$ gets enlarged correspondingly by D^{*+}, D^{*0}, F^{*+}

[4] M. L. Perl et al., Phys. Rev. Lett. 35 (1975) 1489.

[5] M. Kobayashi, T. Maskawa, Prog. of Theor. Phys. 49 (1973) 652.

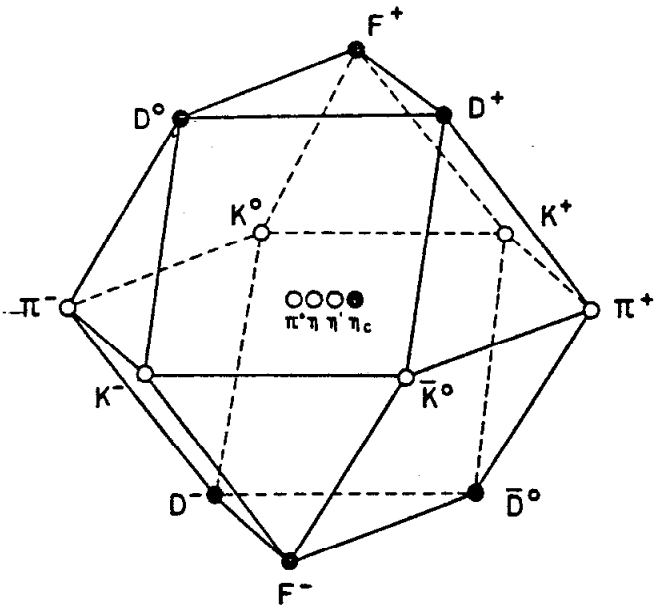

Figure 1. The hexadecimet of the pseudoscalar mesons in SU(4)

Potential models have also been applied reasonably successfully to open charm mesons[6] although one should regard these results with some skepticism since the problem becomes relativistic due to the light quark mass. In the context of this model the $D^* - D$ and $F^* - F$ mass difference are attributed to a "hyperfine" splitting. In case of the D^* mesons this mass difference is just above threshold for the decay $D^* \to \pi^0 + D$. The limited phase space of the pionic transition allows the electromagnetic transition $D^* \to \gamma + D$ to be of comparable strength. Both the π^0 transition and the γ transition complicate the understanding of the inclusive γ spectrum substantially in the center of mass energy region 4.0 GeV to 4.5 GeV. The F^* can only decay through $F^* \to \gamma + F$ since the pionic transition is forbidden by isospin conservation and the $F^* - F$ mass difference is not expected to be large enough for a decay of the form $F^* \to \pi + \pi + F$.

[6] E. Eichten et al., PRL 34 (1975) 369.

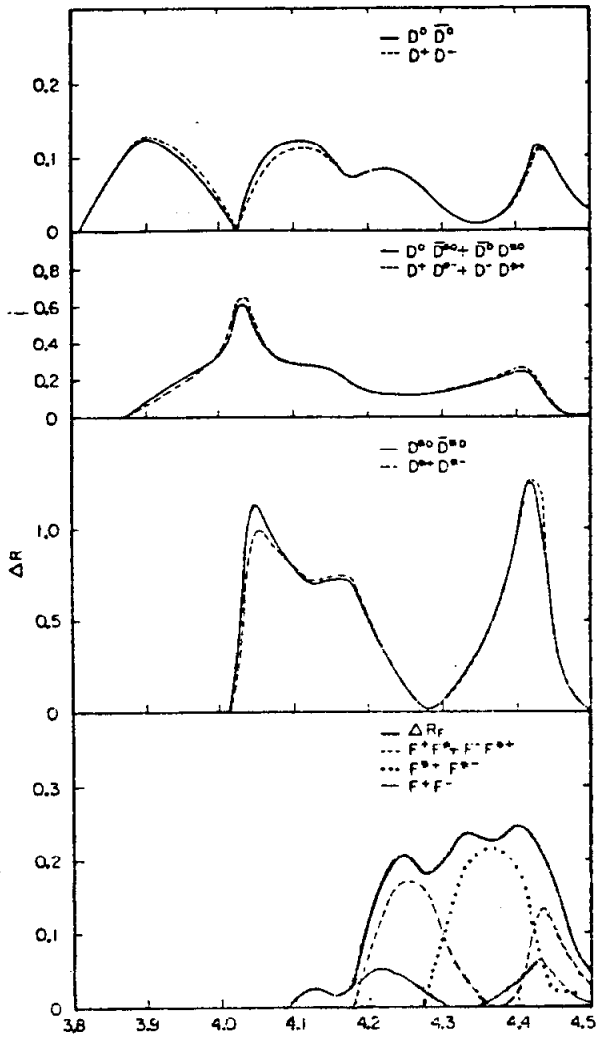

Figure 2. The calculated cross sections for $D\overline{D}$,$D\overline{D}^*$,$D^*\overline{D}^*$ and $F\overline{F}$,$F\overline{F}^*$,$F^*\overline{F}^*$ production as given by the coupled channel model.

A significant extension of the potential model is achieved by incorporating a coupling to charmed meson decay channels.[7] This coupling provides a connection between the discrete set of $c\bar{c}$ states of the initially formed charmonium system and the continuous set of $c\bar{q}, \bar{c}q$ final states. The connection is done via a second quantized interaction Hamiltonian that reduces , for the $c\bar{c}$ system , to the phenomenological binding potential (linear term plus Coulomb term) as is used in the naive nonrelativistic potential models for the bound $c\bar{c}$ states .It also provides terms that allow transition amplitudes to open charm final states. This coupled channel model makes predictions for open charm production in the center of mass energy region from open charm threshold up to $\approx 4.5\,\mathrm{GeV}$. The production cross section has an oscillatory behavior as a function of E_{cm} , which is a direct consequence of the radial nodes of the $c\bar{c}$ particle state. Figure 2 shows the calculated cross sections for $D\bar{D}$,$D\bar{D}^*$,$D^*\bar{D}^*$ and $F\bar{F}$,$F\bar{F}^*$,$F^*\bar{F}^*$ quasi-two-body production . F and F^* production were calculated using a F mass of 2030 MeV and a F^* mass of 2140 MeV , as measured by the *DASP* experiment. The total charm cross section is dominated by $D^{(*)}$ production, and $F^{(*)}$ production is relatively small . The overall calculated cross section seems to explain reasonably well the observed behavior of $R = \frac{\sigma_{hadron}}{\sigma_{\mu^+\mu^-}}$ in this E_{cm} region.

The decay of open charm mesons goes mainly through the weak interaction , and strong interaction effects are thought to be relatively small and perturbatively calculable. Figure 3 shows the lowest order diagrams for the c quark decay by coupling the weak current (1.4) to the intermediate vectorboson $W^{\pm}$. Their relative strength ,due to the different Cabibbo factors , are also shown.

The weak decay of D and F mesons can proceed via two different types of diagrams: One type is called the spectator diagrams since the light quark is only a passive spectator to the decay of the heavy charmed quark. These diagrams have a relative strength that is proportional to the square of the Cabibbo factors that are shown in Figure 3. The Cabibbo favored decays

[7] E. Eichten et al., Phys. Rev. D 21 (1980) 203.

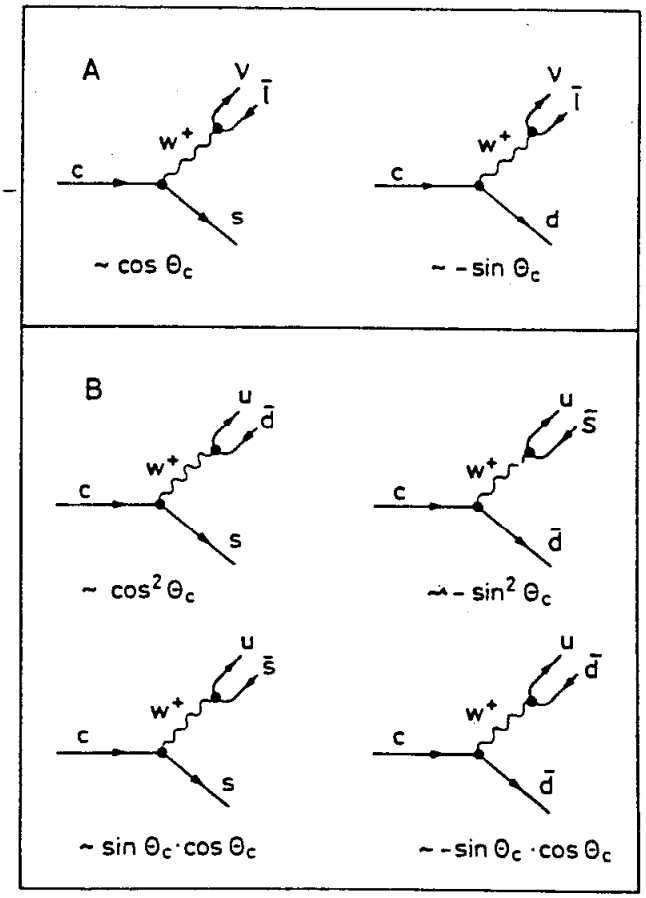

Figure 3. Weak decays of charm quark. a) semileptonic b) hadronic

(diagrams with no $\sin\theta_c$ factor) for the D mesons are of the type $(\overline{K}n\pi)$for hadronic decays and $(l\overline{\nu_l})(K...)$ for the semileptonic decays. For F mesons one expects $F \rightarrow (\eta n\pi),(\eta' n\pi),(K\overline{K}n\pi)$ for the hadronic decays and $F \rightarrow (l\overline{\nu_l})(\eta,\eta',\overline{K}K,\Phi,....)$ for the semileptonic ones.

The second type of diagrams are called annihilation diagrams where the light quark interacts with the $W^{\pm}$ from the c decay. Cabibbo favoured annihilation diagrams are only possible for the D^0 and for the F . In case of the F meson this diagram is suppressed by helicity mismatch , which can be removed by emission of a gluon prior to the annihilation. For the F meson this would result in decays like $F \rightarrow (n\pi),(\omega\pi)$.

Although the spectator process was initially expected to be the dominant diagram for charmed meson decays , one started to consider annihilation diagrams to account for the initial experimental difference in the $D^{\pm}$ to D^0 lifetime and the different observed semileptonic branching ratios. For the situation where the spectator diagrams dominate the decays one would expect $\tau(D^{\pm}) \approx \tau(D^0) \approx \tau(F^{\pm})$ and similarly for the semileptonic branching ratios. Nevertheless , one thinks that the spectator diagrams could account for the present experimental situation as given by the D mesons, especially since the currently best estimate of the ratio of the $D^{\pm}$ to D^0 lifetime has been moving towards unity. For the F meson this means that one expects substantial branching ratios into $\eta + X$, where X stands for 'anything' .[8]

The first experimental results for F production had been presented by the DASP collaboration .[9] They claimed to observe an indication for F production in e^+e^- collisions in the center of mass energy region of 4.36 GeV $-$4.49 GeV and possibly also between 4.10 GeV and 4.23 GeV . They measured the inclusive η production cross section over the E_{cm} range from 4.0 GeV $-$5.0 GeV and found a strong enhancement at the two above mentioned energy steps which they interpreted as coming from F production . This finding was supported by their observation of the decay $e^+e^- \rightarrow$

---

[8] M.Einhorn, C.Quigg, Phys. Rev. D12, 2015(1975); J.Ellis, M.Gaillard, D.Nanoupulos, Nucl. Phys. B100, 313(1975); C. Quigg, J.Rosner, Phys. Rev. D17, 239(1978); D. Fakirov, B.Stech, Nucl. Phys. B133, 315(1978).

[9] R. Brandelik et. al., Phys. Lett. 70B, 132(1977); 80B, 80B, 412(1979); R. Brandelik et. al., Z. Physik, C1, 233(1979).

$F^*\bar{F}^{(*)} \rightarrow \gamma F\bar{F}^{(*)}$, with $F^{\pm} \rightarrow \eta\pi^{\pm}$ at $E_{cm} = 4.36\,\text{GeV} - 4.49\,\text{GeV}$ The final event fits left them with six events which resulted in a $\sigma_{F^*\bar{F}^{(*)}} \cdot BR(F^{\pm} \rightarrow \eta\pi^{\pm}) = 0.41nb \pm 0.18nb$. They were not able to clearly decide between the process $F^*\bar{F}$ and $F^*\bar{F}^*$, but they prefered the first assignment. The masses they obtained were 2030 MeV for the F mass and 2140 MeV for the F^* mass. For the second interpretation both masses were shifted down by 20 MeV . The mass splitting between the F^* and F mass was determined to be 110 MeV $\pm$4.6 MeV. The results of the inclusive η cross section measurement are shown in the lower plot of Figure 5 and results of the exclusive fits in the upper plot.

The MARK II experiment failed to confirm this result and set upper limits for $F\pm$ production $\sigma \cdot BR$ of $0.33nb$ at $E_{cm} = 4.16\,\text{GeV}$ and $0.26nb$ at $E_{cm} = 4.42\,\text{GeV}$.

The Crystal Ball experiment also did a similar inclusive η measurement and failed to confirm the DASP result.

Evidence for $F\pm$ production also exists in photoproduction experiments. The CERN WA4 experiment[10] using the OMEGA spectrometer with a $20-70\,\text{GeV}$ photon beam had seen $F^{\pm}$ signals in $\eta\pi$, $\eta 3\pi$, $\eta 5\pi$,$\eta' 3\pi$ and $\Phi\rho$. The invariant mass plots for the first four decay channels are shown in Figure 5. Similar signals had been obtained later by an upgraded version of this experiment. Using the obtained cross sections times branching ratios for these channels one can obtain an upper limit for the branching ratio of $BR(F^{\pm} \rightarrow \eta\pi^{\pm}) < 0.16$.

Further evidence on $F^{\pm}$ production comes also from emulsion experiments[11] in neutrino interactions , but all these experiments have only a few events each ,and there are not enough statistical data to make an invariant mass plot that would show significant clustering of events at a specific mass.

The best current estimate of the F mass given by the Particle Data Group is $m_{F\pm} =$ 2021.1 MeV $\pm$15.2 MeV.

---

[10] D. Aston et.al. CERN/EP/80-189.

[11] R. Ammar et.al. Phys. Lett. 94B, 118 (1980). N. Ushida et.al. Phys. Lett. 45, 1049, (1980).

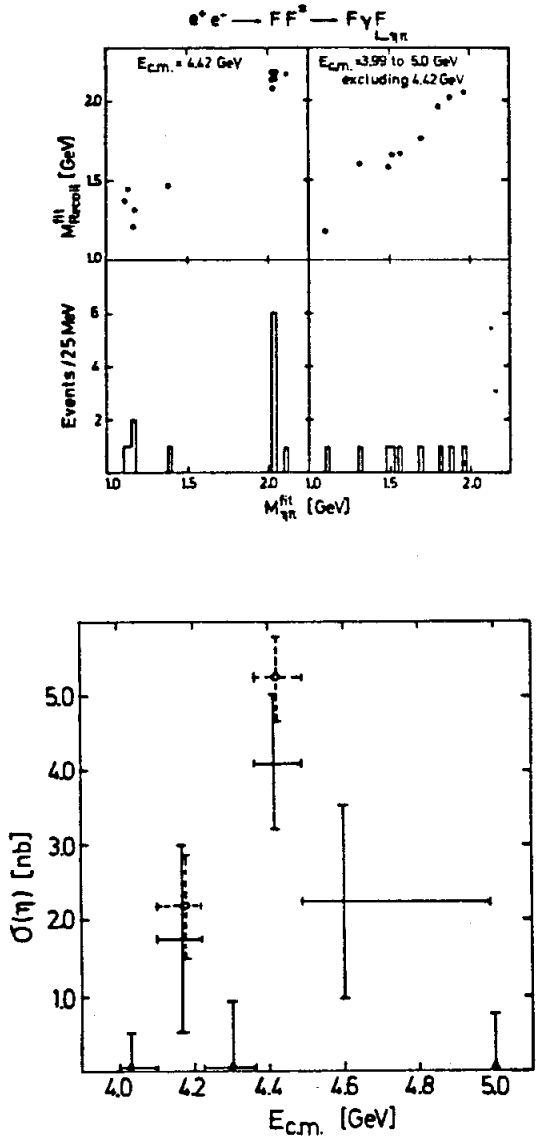

Figure 4. DASP results on F production. Upper plot shows the resulting F and F^* masses for the fit $e^+e^- \to F^*\overline{F} \to \gamma F\overline{F}$, with $F^\pm \to \eta\pi^\pm$. The lower plot shows the inclusive η measurement which indicates strong η production at $E_{cm} = 4.42\,\text{GeV}$ and $4.17\,\text{GeV}$.

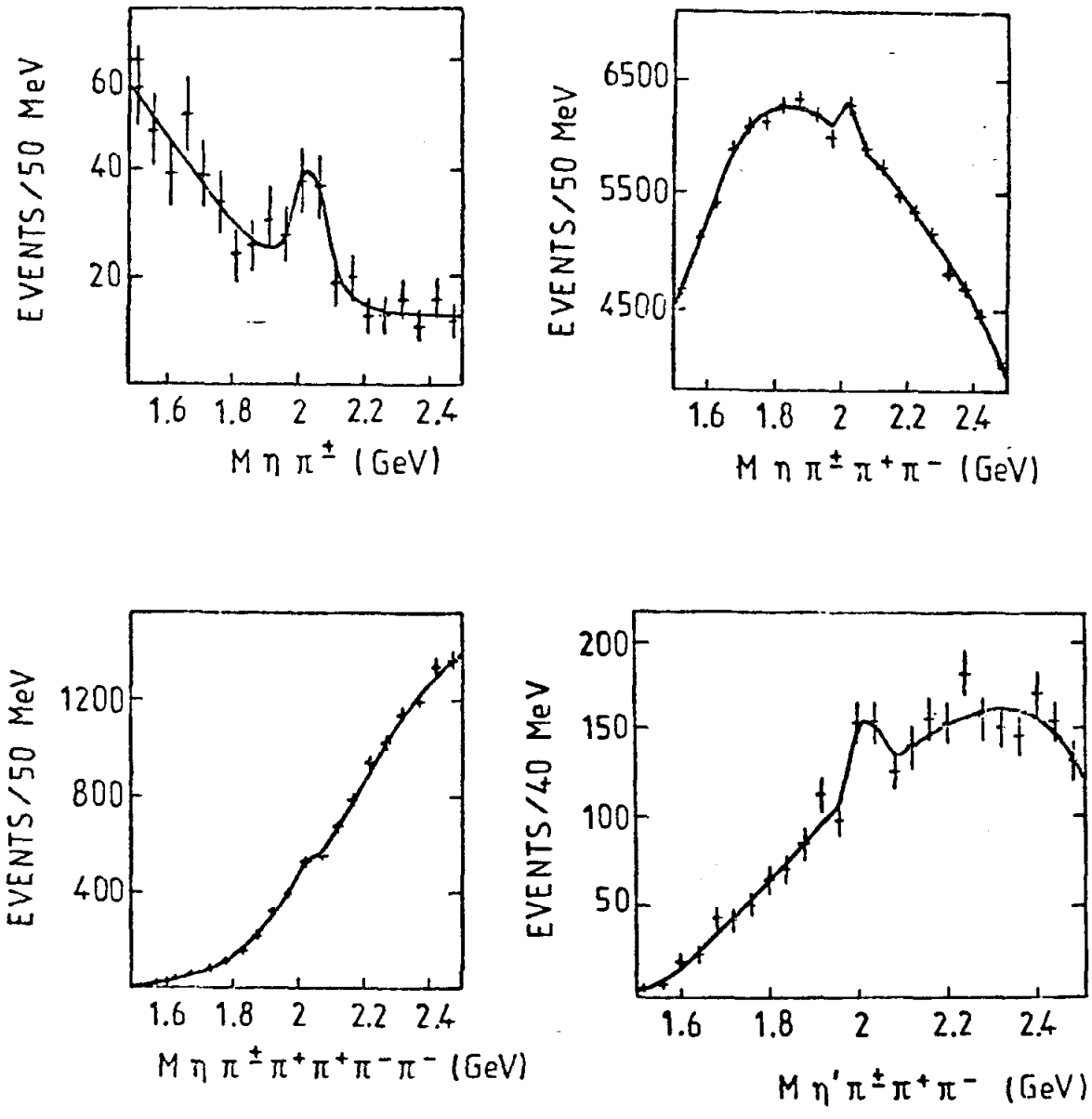

Figure 5. Invariant mass plots for various decay channels of the F meson as seen by the OMEGA photoproduction experiment.

§1.2 SEARCH FOR F MESONS WITH THE CRYSTAL BALL

The search for the charmed F and F^* meson with the Crystal Ball detector was motivated by the fact that this detector has a very good capability for measuring η's and low energy γ's . The data were taken at SPEAR in the center of mass energy region from 3.86 GeV to 4.50 GeV . The search was done in three different ways and each method with the obtained results is described in one of the subsequent chapters of this thesis.

The three methods are :

A measurement of the inclusive η cross section over the above mentioned center of mass energy region in order to confirm the increase in η production due to F's as claimed by the DASP experiment.

A search for a monochromatic γ line in the inclusive γ spectrum that would result from F^* production with the subsequent decay $F^* \rightarrow \gamma F$. This method only works if the center of mass energy is not too high above the energy threshold for $F^*\overline{F}$ or $F^*\overline{F}^*$ production. With the F mass of 2021 MeV $\pm$15 MeV and the $F^* - F$ mass splitting of 110 MeV $\pm$4.6 MeV this gives an energy threshold of 4262 MeV . Using the inclusive γ spectrum obtained from data taken at $E_{cm} =$ 4330 MeV it would ,therefore , be possible to observe $F^*\overline{F}^*$ production.

A search for $F\overline{F}$, $F\overline{F}^*$, $F^*\overline{F}^*$ events with one F having the decay $F^{\pm} \rightarrow \eta\pi^{\pm}$ and the other F going to "anything" . For the case of $F\overline{F}^*$ production and $F^*\overline{F}^*$ production the transition γ's also have to be measured . This permits semi-exclusive fits that are similar to the ones that were used for the DASP result.

Chapter 2

EXPERIMENTAL APPARATUS

§2.1 INTRODUCTION

The Crystal Ball was designed to be a photon detector of good energy resolution over a broad range of photon energies of 10 MeV −4000 MeV . By using a highly segmented array of NaI(Tl) crystals , which covers almost the full solid angle , an accurate measurement of the photon direction is also possible. This makes the experiment especially well suited for the detection of monochromatic photons and neutral particles which decay into all photon final states like the π^0 or η .

In addition , the experiment has also limited capabilities for charged particle detection. A set of central tracking chambers allows discrimination between neutral and charged particles along with an accurate measurement of the charged particle direction. Since the Crystal Ball is a nonmagnetic detector , no measurement of the charged particle momentum is possible . In the following sections a more detailed description of the experimental location and of various parts of the detector itself will be given.

§2.2 SPEAR

The Crystal Ball experiment was located in the East Pit (see Figure 6) of the e^+e^- storage ring SPEAR at SLAC between Fall 1978 and Winter 1981-1982. The SPEAR ring was constructed in 1972 and upgraded in 1974 to the present energy range of $E_{cm} = 2.4\,\mathrm{GeV} - 8.2\,\mathrm{GeV}$. Single bunches of electrons and positrons orbit in opposite directions in the same evacuated beampipe ($\approx 10^{-9}$torr) and collide in two interaction regions. SPEAR is a separated function machine with dipole magnets used for bending in the horizontal plane and quadrupoles used for focussing the beam. The LINAC normally injects first e^+ and then e^- into SPEAR with a injection energy up to 2.5GeV. The two counter-rotating bunches of electrons and positrons typically contain 5×10^{10} particles each and have a revolution frequency of 1.28 MHz . The particles oscillate around their design orbit in the transverse horizontal x-direction (betatron-oscillations) as well as along the longitudinal z-direction (synchrotron-oscillations). The betatron-oscillations also couple to oscillations in the vertical y-direction, mainly due to lattice imperfections. These vertical oscillations are roughly an order of magnitude smaller than the betatron-oscillations. At the interaction point , the gaussian shaped beams have a width of $\sigma_x \approx 0.6mm$ and $\sigma_y \approx 0.04mm$. The particles also lose energy due to synchrotron radiation. This loss is proportional to E^4_{beam} and amounts to 60KeV per turn at $E_{beam} = 2.15\,\mathrm{GeV}$. This loss is compensated with 4 RF cavities which run at a frequency of 280 times the bunch revolution frequency. The energy spread of the beam is determined by quantum fluctuations in synchrotron radiation. The resulting energy width is $\approx 1\,\mathrm{MeV}$ at the ψ' and is only of concern if running at narrow resonances. The longitudinal bunch width σ_z is also a result of synchrotron fluctuations . The width of the luminous region is a factor $\sqrt{2}$ smaller than the bunch length and was measured to be 24mm at $E_{cm} = 4.33\,\mathrm{GeV}$. The beam energy is determined by a measurement of the magnetic field of the bending dipole magnets , using a correction factor from the measured orbit geometry. The uncertainty in the calibration of the beam energy is estimated to be 0.1% .

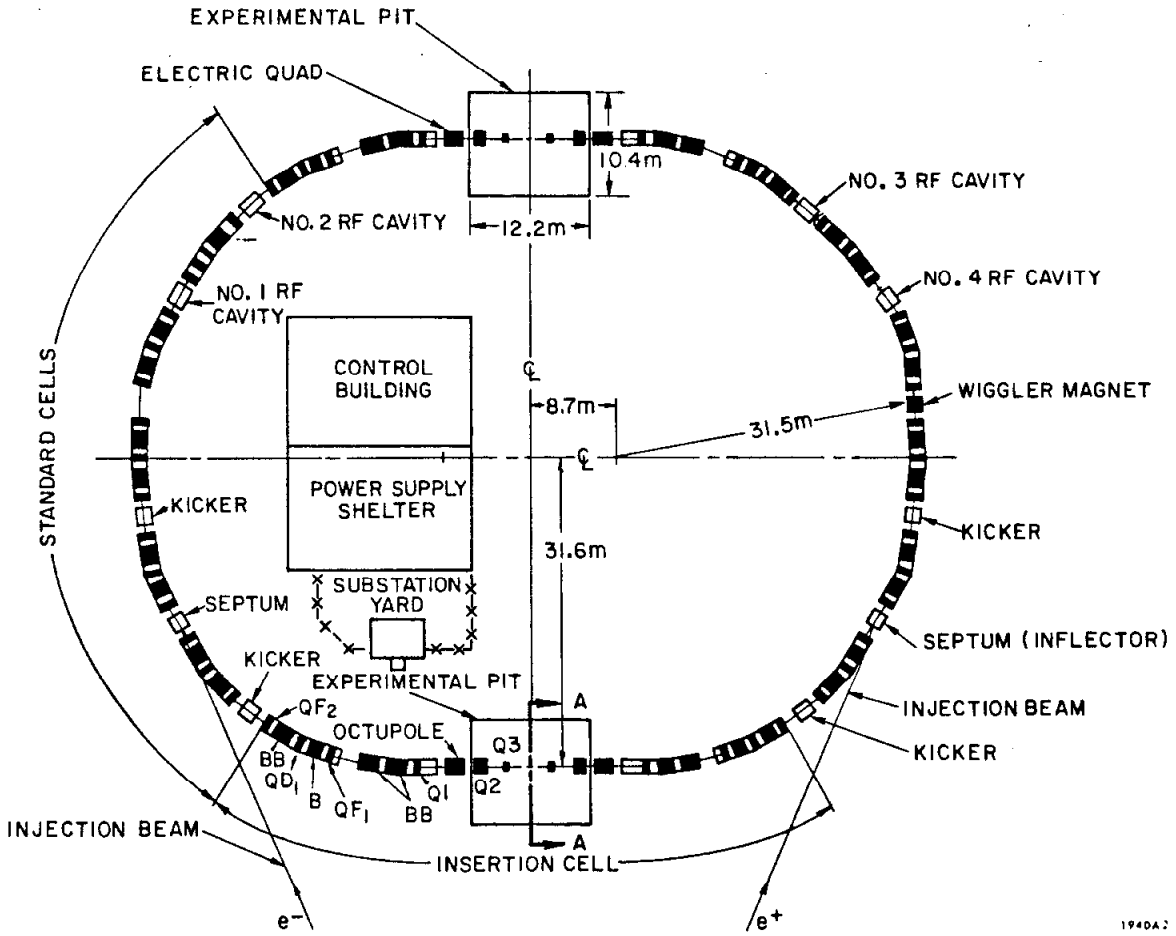

Figure 6. The SPEAR storage ring. The upper experimental hall is the East Pit , hosting the Crystal Ball experiment.

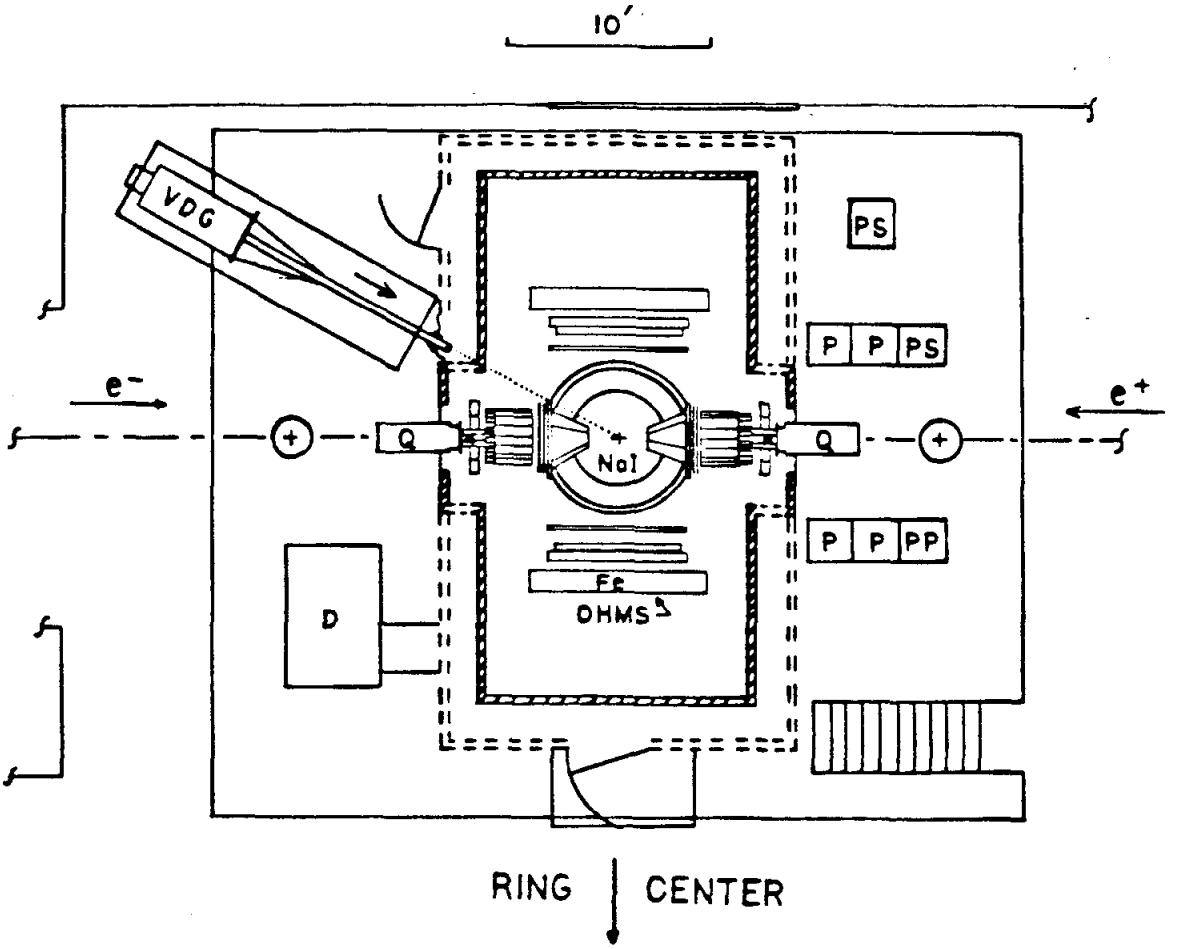

Figure 7. East Pit interacton region with Crystal Ball experiment. VDG = Van de Graaff system; D = Dehumidifier; PS = Power supply for MWPC or spark chambers; P = HV pulser; PP = Prepulser for spark chamber; Q = Quadrupole magnet; Dotted wall denotes the ball room.

The luminosity $\mathcal{L}$ is defined by

$$\frac{dN}{dt} = \mathcal{L} \cdot \sigma$$

where $\frac{dN}{dt}$ is the rate per second for a certain process with the cross section σ. At $E_{cm} = 4.33\,\mathrm{GeV}$ the typical starting luminosity at the beginning of a fill was $2 - 4 \times 10^{30} cm^{-1} sec^{-1}$ with e^+ and e^- currents of $\approx 10 - 15 mA$. For most of the data taken in the $4.0 - 4.5\,\mathrm{GeV}$ region , a wiggler magnet was inserted into the beamline. This improves the luminosity by increasing the beam size and therefore allowing higher currents to be stored.The luminosity increased up to the order of 20%. Averaged over longer running periods , data could be collected with an integrated luminosity of about $100 nb^{-1}$ per day.

§2.3 LAYOUT OF THE EXPERIMENT

The general layout of the Crystal Ball experiment in the East Pit of SPEAR is shown in Figure 7 . The e^- bunch enters the interaction region from the left , the e^+ bunch from the right side. The last two quadrupole magnets ,which focus the beam to the interaction point , are just half inside the dryroom , which provided a temperature stabilized ($20^0\mathrm{C} \pm 1^0\mathrm{C}$) and dehumidified (-42^0 dew point) environment for the Crystal Ball . This dry atmosphere was additional security for the hygroscopic NaI crystals , in case that one of the two sealed and partially evacuated hemispheres of the "Ball" would leak. The environmental conditions in the "Ball room", as well as inside the hemispheres themselves , were remotely sensed and displayed in the control room , which contained also most of the signal processing electronics together with the online computer. Outside of the "Ball room" there was a 500KeV proton Van de Graaf accelerator as shown in Figure 7 . It was mounted on rails so that its 14 foot long beam pipe could be inserted in between the almost closed ball hemispheres for energy calibration of the NaI crystals.

The central detector is schematically shown in Figure 8 .Going from the interaction point towards outside, one first has the beampipe which consists of an aluminum tube of 51 mm radius

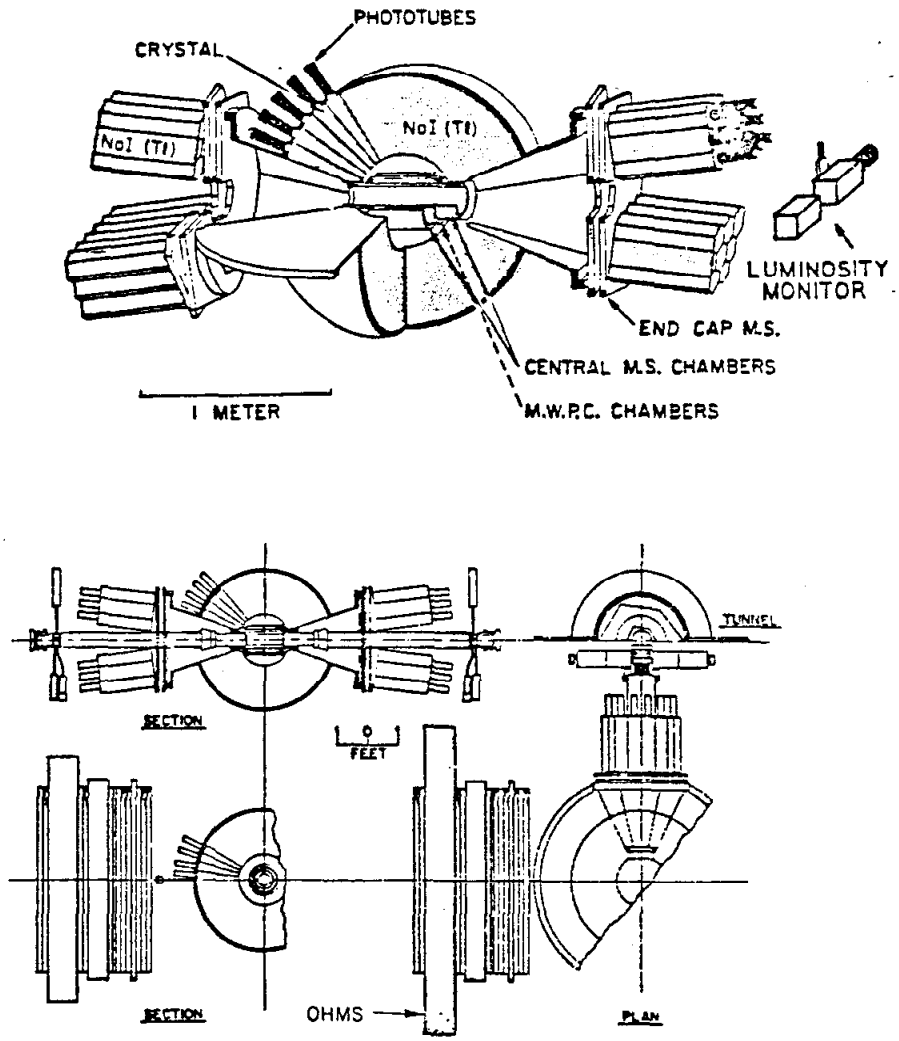

Figure 8. The Crystal Ball detector

and of 0.065 inch wall thickness. This corresponds to 1.83% radiation length in direction normal to the beampipe. Outside the beampipe there is a set of charged particle tracking chambers. Initially these were 4 layers of sparkchambers interleaved with 2 layers of multiwire proportional chambers. They were replaced in the summer of 1981 by 6 layers of proportional gas tube chambers with charge division readout.

The Crystal Ball proper consists of two separate enclosed hemispheres containing the 672 thallium doped sodium iodide (NaI(Tl)) crystals. The two hemispheres could be opened and closed vertically around the beampipe with a hydraulic lift mechanism. This allowed access to the central tracking chambers and also protected the ball from unwanted radiation during SPEAR machine physics running or synchrotron radiation running. Accumulated radiation doses were monitored with thermoluminescent dosimeters. Total integrated dosage for all SPEAR running amounts to $\approx$ 300 rad and did not result in any observable degradation of the NaI(Tl) crystals.

In order to increase the solid angle coverage of the central ball , additional endcap crystals were installed around the beampipe together with 2 modules of planar spark chambers for charged particle tracking.[1] The endcaps were not used in this data analysis . Therefore further discussion is omitted.

In between the last quadrupole magnets of SPEAR and the endcap crystals there was also a luminosity monitor , measuring small angle Bhabha scattering.

Outside of the central detector was the Outer-Hardon-Muon-Separator (OHMS) , placed inside the "ballroom" on each side of the beamline. It consisted of vertical layers of iron , along with proportional chambers and scintillator counters. The solid angle covered of OHMS was 15% of 4π . OHMS was intended to allow the identification of Muons by requiring a single noninteracting track across all the layers. On the other hand, hadrons that had not interacted in the NaI(Tl) shell would have a high probability of interacting in one of the iron layers. A more detailed

[1] J. Tompkins Crystal Ball-note 232 (1977).

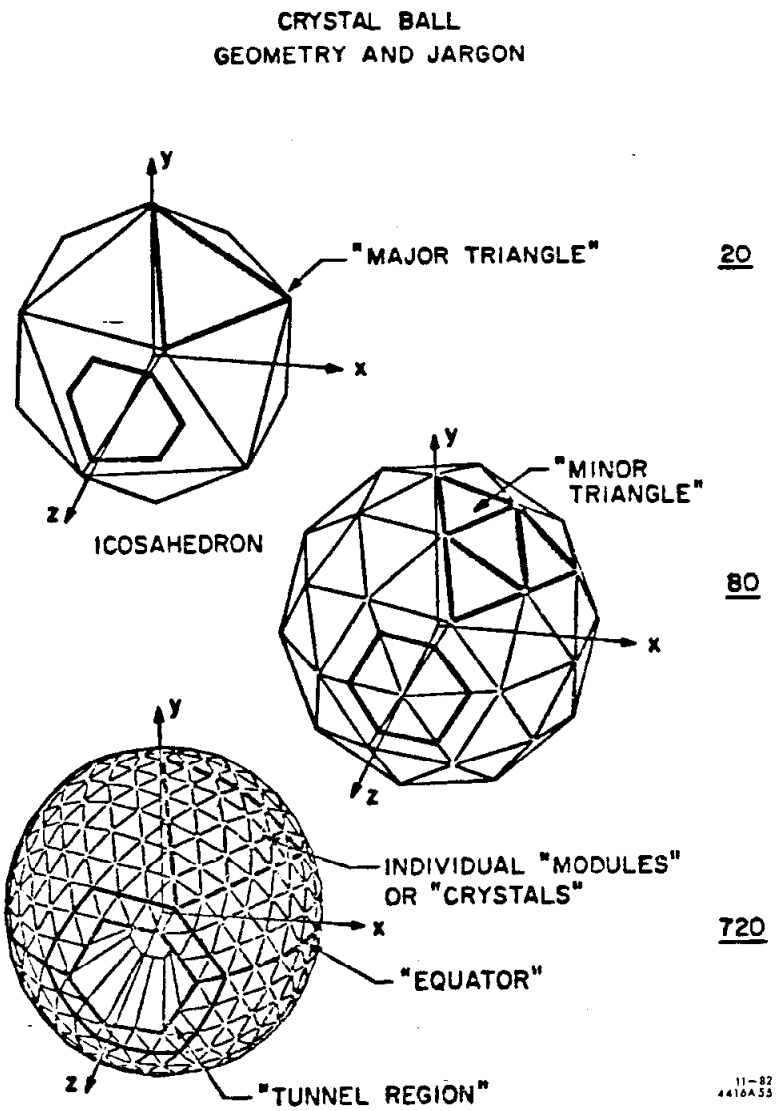

Figure 9. The Crystal Ball Geometry

discussion of OHMS is omitted since no OHMS data were used for this analysis.

Subsequent sections will give a more detailed description of the above mentioned elements of the experiment that are shown in Figure 9 .

§2.4 THE CRYSTAL BALL (NaI(Tl))

The Crystal Ball (NaI(Tl)) is the central component of the detector and has given its name to the whole experiment. It consists of a segmented spherical shell of 672 optically isolated crystals made of thallium doped sodium iodine (NaI(Tl)). The outer ball radius is 26 inches ,and the inner cavity radius is 10 inches. The choice of NaI(Tl) as a scintillation material is mainly due to its good energy resolution ($\sigma_E = \frac{2.6\%}{E^{\frac{1}{4}}}$) down to very low photon energies and its high percentage of light output ($\approx$ 10% of deposited energy). However,the fact that NaI(Tl) is very hygroscopic and cannot be exposed to open air substantially complicates its handling .

The segmentation that is used for the Crystal Ball starts with a 20-sided regular icosahedron (see Figure 9) . Each side of these 20 regular "major" triangles is bisected and the new vertices projected onto a sphere. This results in 4×20 "minor" triangles. Then each side of the 80 "minor" triangles is trisected and the new vertices projected onto the sphere again. The obtained 720 crystals have 11 slightly different triangular shapes (up to about 15% difference in solid angle).To create space for the beampipe to enter , 48 crystals forming two opposite tunnels are removed. The resulting 672 crystals still cover 94% of 4π solid angle. This segmentation allows a division of the crystal shell along an equatorial plane into two separate hemispheres.These are hermetically sealed into two cans that are made of an outer aluminum shell and a thin equatorial sheet of stainless steel together with a inner shell of 0.0625 inch of stainless steel.The inner and the outer shell are connected with radial wires . Since the upper hemisphere has only about 0.8 times atmospheric pressure inside , most of the weight of the crystals is carried by the atmospheric pressure acting on the equatorial plane.

The 16 inch thick NaI(Tl) shell is equivalent to $15.7L_{RAD}$ for showering particles ($\gamma, e^{\pm}$) and corresponds to roughly one nuclear radiation length for strongly interacting hadrons (π,K,p,n).

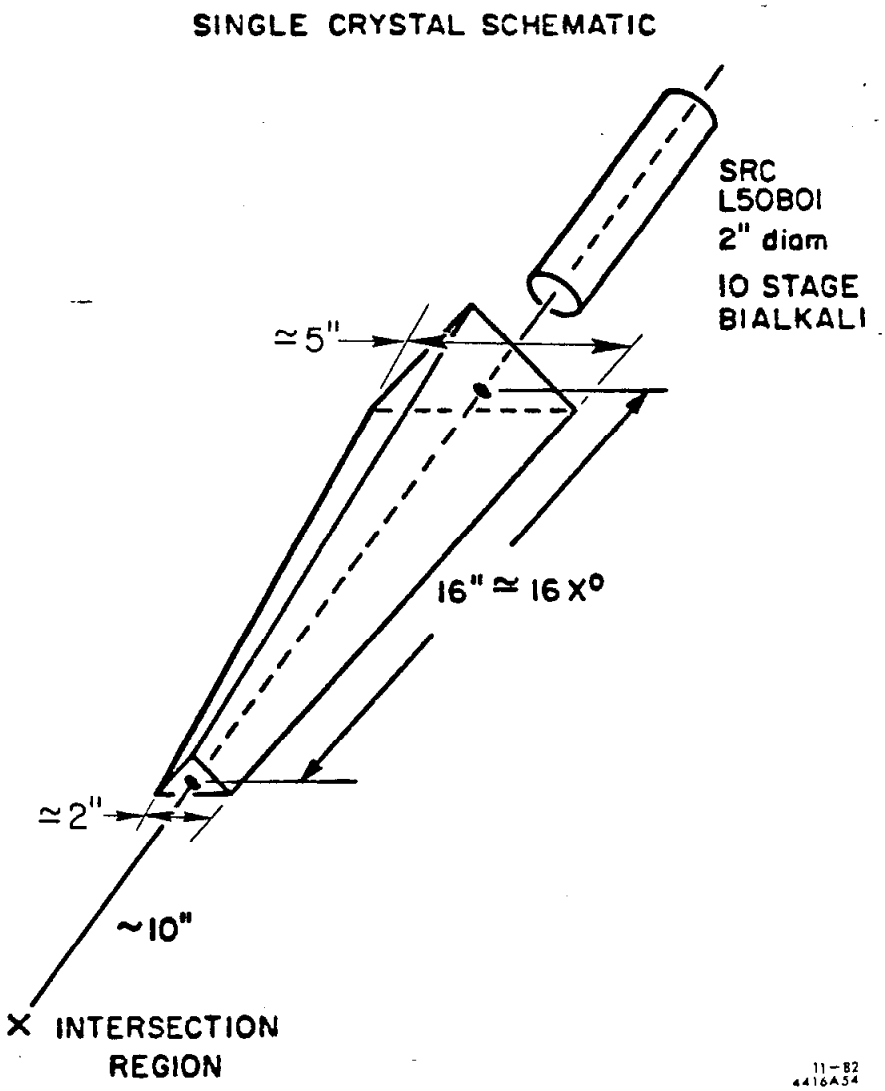

Figure 10. A single module: crystal with photomuliplier tube

One would ,therefore, expect roughly 1/3 of the charged hadrons to be noninteracting and therefore deposit an average of 210 MeV of energy along their paths through the crystal by energy loss through minimum ionization. The light produced by the scintillation in the crystal is detected by a 2 inch diameter , 10 stage bialkali photomultiplier , which is separated from the crystal by a 2 inch air gap and a glass window. Figure 11 shows a schematic drawing of a NaI(Tl) crystal with its photomultiplier tube.

§2.5 CENTRAL TRACKING CHAMBERS

Inside the 10 inch cavity of the ball ,there was a set of charged particle tracking chambers . They allowed the separationof charged particles from neutral ones and an accurate direction measurement of the charged particle track along with a determination of the position of the primary event vertex . There were two different types of chambers installed during the time data were taken for this analysis . Between fall 1978 and summer 1981 4 layers of spark chambers together with 2 layers of multiwire proportional chamber were used.[2] In the summer of 1981 a new set of proportional tube chambers containing 6 layers was installed.

The magnetostrictive spark chambers consisted of an inner chamber set covering a solid angle of 94% of 4π and an outer chamber set covering 71% of 4π . Both chambers had 2 spark gaps that were formed by three concentric cylindrical shells made out of two copper coated mylar foils (4 mils) . They formed a sandwich construction with 40 mils of styrofoam in between. The copper foils (1.5 mils) served as HV planes and had traces edged in them that were 0.3mm wide and had a 1.0mm center to center spacing. Figure 11 shows a schematic drawing of the spark chambers. One plane in each gap had inclined traces to get the z position of a spark. The inclination angle was 30^0 for the inner chamber and 45^0 for the outer chamber. Using inclined planes for the z measurement introduced also the problem of combinatorics for the track reconstruction in events with several

[2] actually there was a slightly diffrent set of spark chambers installed in summer 1979

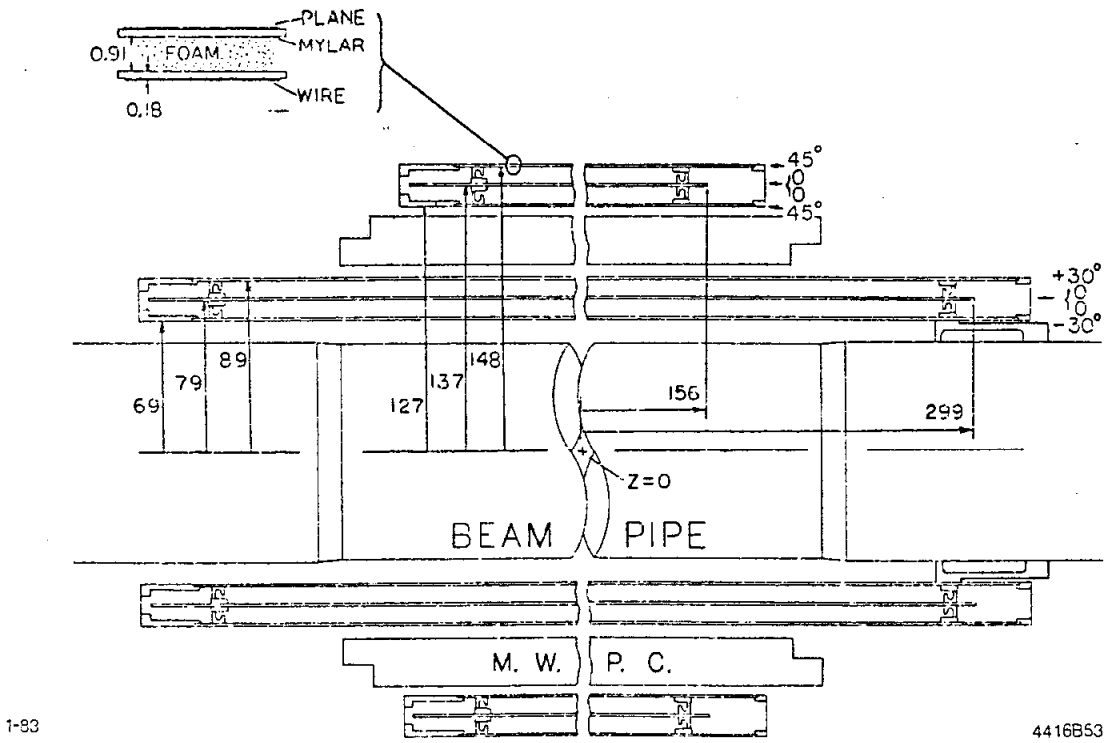

Figure 11. The central spark chambers.

All measures are in millimeters.

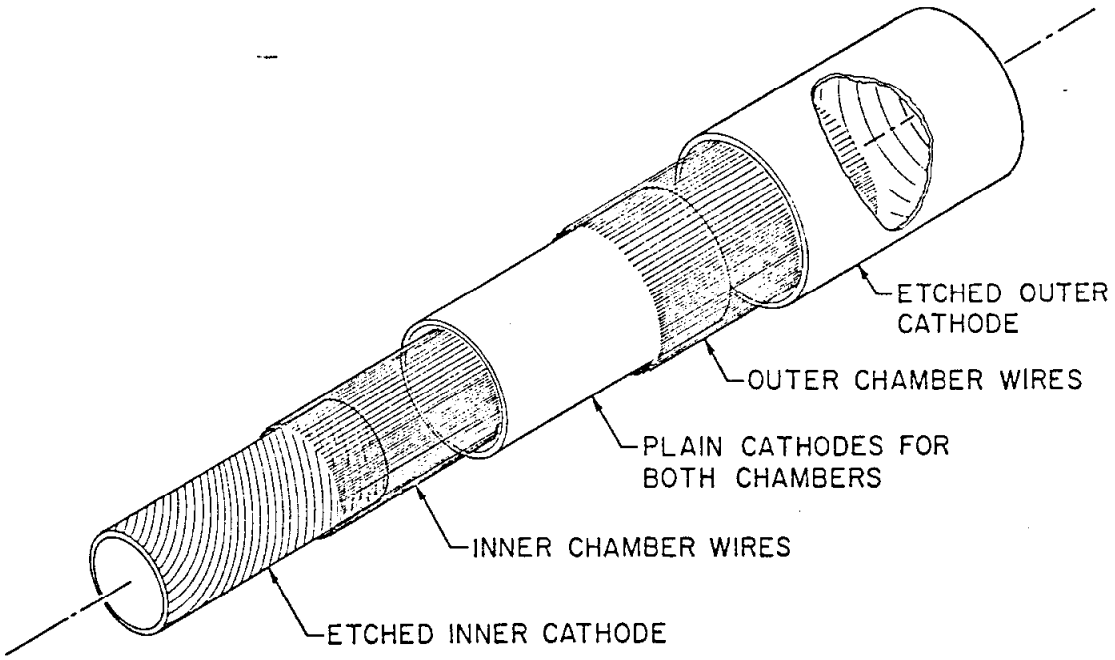

Figure 12. Exploded view of the Multi-Wire-Proportional-Chamber

charged tracks. The existence of noise hits also complicated the track reconstruction as is described in Appendix B. More details about these chambers can be found in reference.[3]

If a charged particle passed through the chambers and a trigger was formed, then a 9KV high voltage pulse was applied across the 9mm spark gaps with a spark developing along the ionisation track left by the passing particle in the noble gas mixture ($90\%Ne$,$10\%He$). The spark current generated a sound wave in a magnetostrictive wire that was wound across the copper tracings. This traveling sound wave along with fiducial signals for chamber calibration were then sensed by a pickup coil and the time difference between signals was digitized.

The Multi-Wire-Proportional-Chamber (MWPC) was located in between the two spark chambers and had a similar mechanical construction , but used aluminum coated mylar . The anode wires in this case consisted of 144 gold-plated tungsten wires of 0.02mm diameter. The 36 edged cathode strips were inclined by 62^0 (90^0) for the inner (outer) gap. Figure 13 gives a schematic view of the MWPC geometry. The solid angle covered by the MPWC was 83% of 4π. Both gaps used the same gas mixture ($90\%Ar$,$10\%CO_2$) and both cathodes were held at -1.7KV relative to the sense wires. Since the chambers ran in a proportional mode , their signals could be used to form the trigger along with the NaI(Tl)-ball . More details about contruction and performance of the MWPC can be found in reference.[4]

After the summer of 1981 the above described chambers were replaced by 6 layers of proportional tube chambers with charge division readout. Figure 14 schematically shows the geometry of the these tube chambers. The 640 tubes were arranged in 3 double layers with 160 tubes per layer for the innermost double layer , and 80 tubes per layer for the outer two double layers. The solid angle covered by the 3 double layers was 98^0, 96^0 and 75^0 of 4π. The aluminum tubes used had a diameter of 4.83mm and 5.6mm and were chemically etched down to a wall thickness of 0.08mm in order to minimize the conversion probabilty for photons. Each tube had a

[3] F. Bulos , Crystal Ball - note 117 (1976).

[4] J. Gaiser et al, IEEE Trans. Nucl. Sci. NS-26 No. 1, 1 73 (1979).

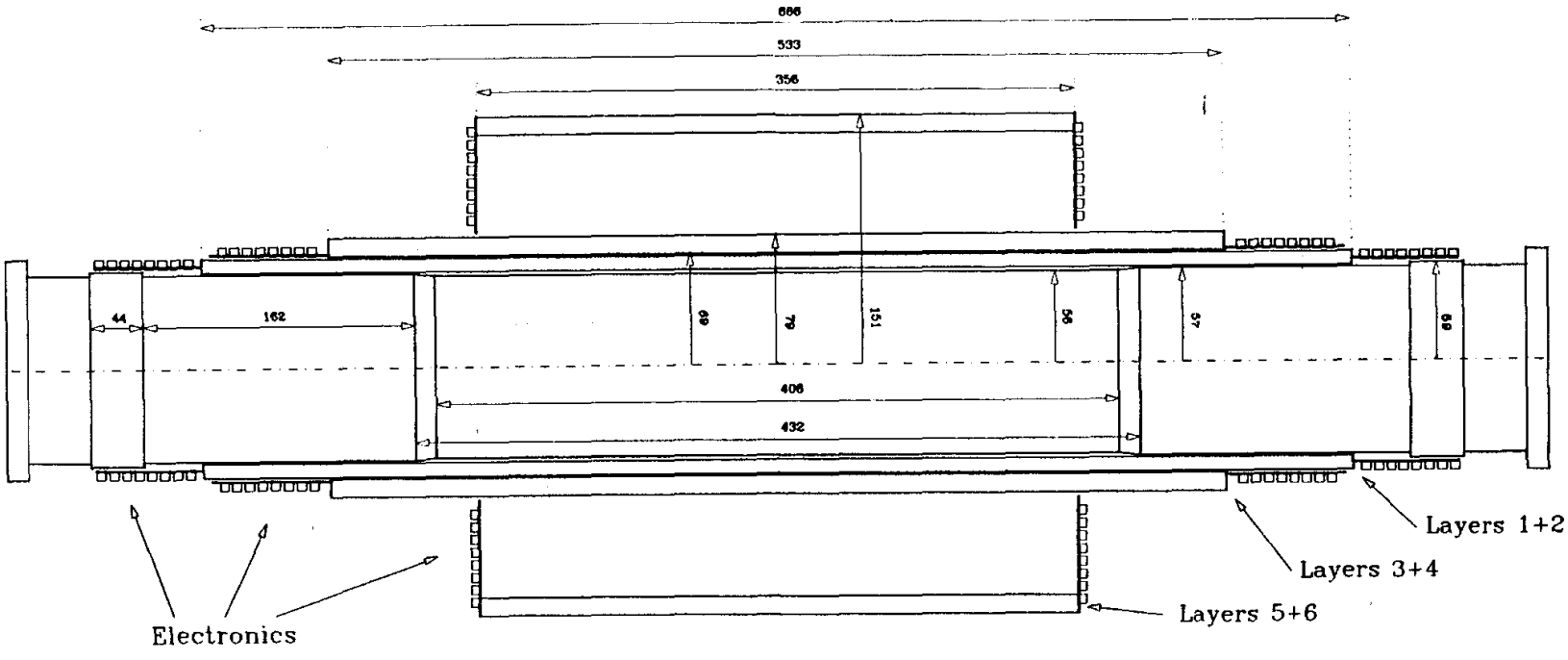

Figure 13. **The proportional tube chambers.**

All measures are in millimeters.

stainless steel anode wire (0.045 mm) with a total resistance of $\approx 300\Omega$ over the full tube length. Both ends had a charge sensitive amplifier that was directly mounted onto the chamber. This allowed the z measurement of the charged track hits without the combinatorics problem that plagued track reconstruction in case of the spark chambers and MWPC. The chambers operated with "magic" gas (20%Iso butane,1%Methylal,.25%Freon 13B1, complete Argon to 100%) which ideally gives a big pulse height on the anode wire that is almost independent of the amount of primary ionisation. The chambers were typically operated at a high voltage of 2200V-2500V. More details about construction and performance of the tube chambers and their calibration are discussed in Appendix A .

§2.6 LUMINOSITY MONITOR

The luminosity at the interaction point was measured by recording the counting rate $\frac{dN}{dt}$ of small angle Bhabha events by four counter telescopes as shown in Figure 18 . Each telescope had 2 aperture defining scintillation counters (P,C) and a shower counter (S) for a rough energy measurement of the Bhabha event. The Q-counter only served for diagnostics. The signature of a Bhabha event is $P_iS_iC_jS_j$ with $i = 1,2,3,4$ and j being opposite to i. The counter telescopes were positioned at an angle of 4.25^0 with respect to the incoming beam. The Bhabha rate has a very steep angular dependence , and so the sum of the four counter telescope rates was used to get a result that was to first order independent of possible beam displacements. Ratios of the telescope rates could be used to calculate a horizontal displacement of the interaction point. Finally , the luminosity was calculated by dividing the measured Bhabha counting rate $\frac{dN}{dt}$ by the integrated Bhabha cross section σ of the counter telescopes. This cross section σ was calculated by using a Monte Carlo program developed by Berends et al.[5] that also includes radiative corrections to the lowest order Bhabha cross section. The electronics of the luminosity monitor consisted of a fast logic for the trigger decision and a CAMAC electronics for data transfer to $PDP-11/T55$

[5] F. A. Berends, K. J. F. Gaemers, R. Gastmans, Nucl. Phys. B68, 541 (1974)

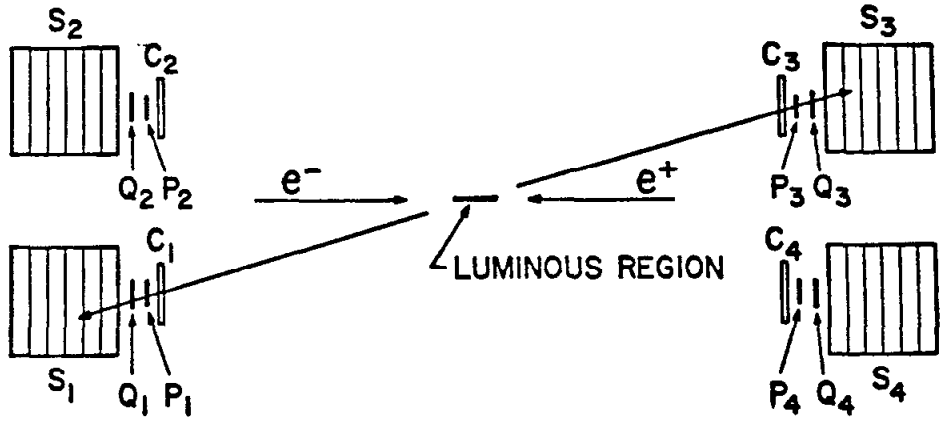

Figure 14. Schematic of the four counter telescopes of the luminosity monitor. Counters P define the telescope solid angle. The Bhabha signature is $P_i S_i C_j S_j$ with $i = 1, 2, 3, 4$ and j being opposite to i with the shower counters S required to measure more than half of the beam energy.

computer. The luminosity monitor has been shown to agree with an error of less than 4% with a measurement of the luminosity using Bhabha events in the ball. More details about the luminosity monitor can be found in reference.[6]

§2.7 TRIGGER

There were two independent trigger systems used in the experiment. The first trigger system, called the tower trigger, was a compact TTL logic system.[7] The other trigger , called the fast trigger, was built from modular NIM logic.[8] Both triggers performed analog summations of signals coming from the ball and the MWPC. The ball signals used were fast-out analog sums of 9 crystals (minor triangle). The MWPC signal required a coincidence of wire hits from the two MWPC layers.

For the formation of a trigger , at least one of the following trigger conditions had to be fulfilled:

a.) $E_{ball} > 1150\,\mathrm{MeV}$

b.) At least 60 MeV in two opposing major triangles.

c.) More than 2 major triangles with at least 140 MeV and at least one MWPC signal.

d.) $E_{hemi} > 144\,\mathrm{MeV}$ for both hemispheres and $E_{ball} > 770\,\mathrm{MeV}$

E_{ball} is the total energy in the ball without the tunnel modules, and E_{hemi} is the total energy in a hemisphere excluding the tunnel modules.

For data taken after Spring 1981 , another trigger condition was installed, called the topology trigger . The ball was conceptually divided into 3 virtual pairs of hemispheres by rotating the true equatorial plane around the z axis by 60^0. The trigger requirement was that no such hemisphere should have less than 150 MeV and $E_{ball} > 460\,\mathrm{MeV}$. The total trigger rate was

---

[6] H. Kolanoski ,Crystal Ball- note 244 (1978).

[7] G. Godfrey , Crystal Ball- note 131 (1978).

[8] M. Oreglia , SLAC-Report-236 (1980)

about $2-3Hz$ and led to a deadtime of the experiment of $\approx 10\%$. This deadtime was basically determined by the spark chamber recovery time which was $\approx 40msec$.

§2.8 DATA ACQUISITION SYSTEM

All the signals from the detector were digitized and read into the $PDP-11/T55$ online computer via a CAMAC data acquisition system. The data were then stored in memory buffers and written on tape for further offline data analysis. Before events were written to tape the data were compressed in order to fit more events on the tapes. The compression consisted of a pedestal subtraction of the digitized signals from the NaI(Tl) crystals and of a suppression of all the crystal energies with less than 80KeV. For the proportional tube chambers a similar pedestal subtraction was done. Every 128th event was written to tape in uncompressed format in order to have later in the offline calibration the possibilty to monitor any pedestal drift and to correct for it. The online data acquisition program[9] also did numerous hardware control checks and allowed an online analysis for some fundamental physics quantities , such as the total hadronic cross section. A link was established between the PDP-11 and the SLAC Triplex computer system (two IBM 370/168 and one IBM 360/91) that allowed to transfer events to the Triplex for a more complicated analysis of the data taken.

[9] R. Chestnut et al., IEEE Trans. on Nucl. Sci. NS-26,4395(1979).

Chapter 3

DATA

§3.1 DATA AQUISITION

The data used for this analysis were taken at SPEAR in Spring 79 , Spring 80 and Fall 81.

The Spring 79 and Spring 80 data were both taken in a "scanning" mode by changing the center of mass energy E_{cm} in steps of of bewteen 6 to 12 MeV. The energy range covered in this way extends from 3.87 GeV $-$4.5 GeV. The total integrated luminosity of the Spring 79 data is $3397nb^{-1}$ and $5468nb^{-1}$ for the Spring 80 data . Figure 15 shows the accumulated luminosity as a function of E_{cm} for both data samples combined. These data were taken with magnetostrictive sparkchambers and the MWPC as the central tracking detector.

In Fall 81 , another run was made at a fixed center of mass energy $E_{cm} = 4.33$ GeV . The total integrated luminosity accumulated by this run is $1506nb^{-1}$. This data set was taken with the proportional tube chambers as a central charged tracking detector.

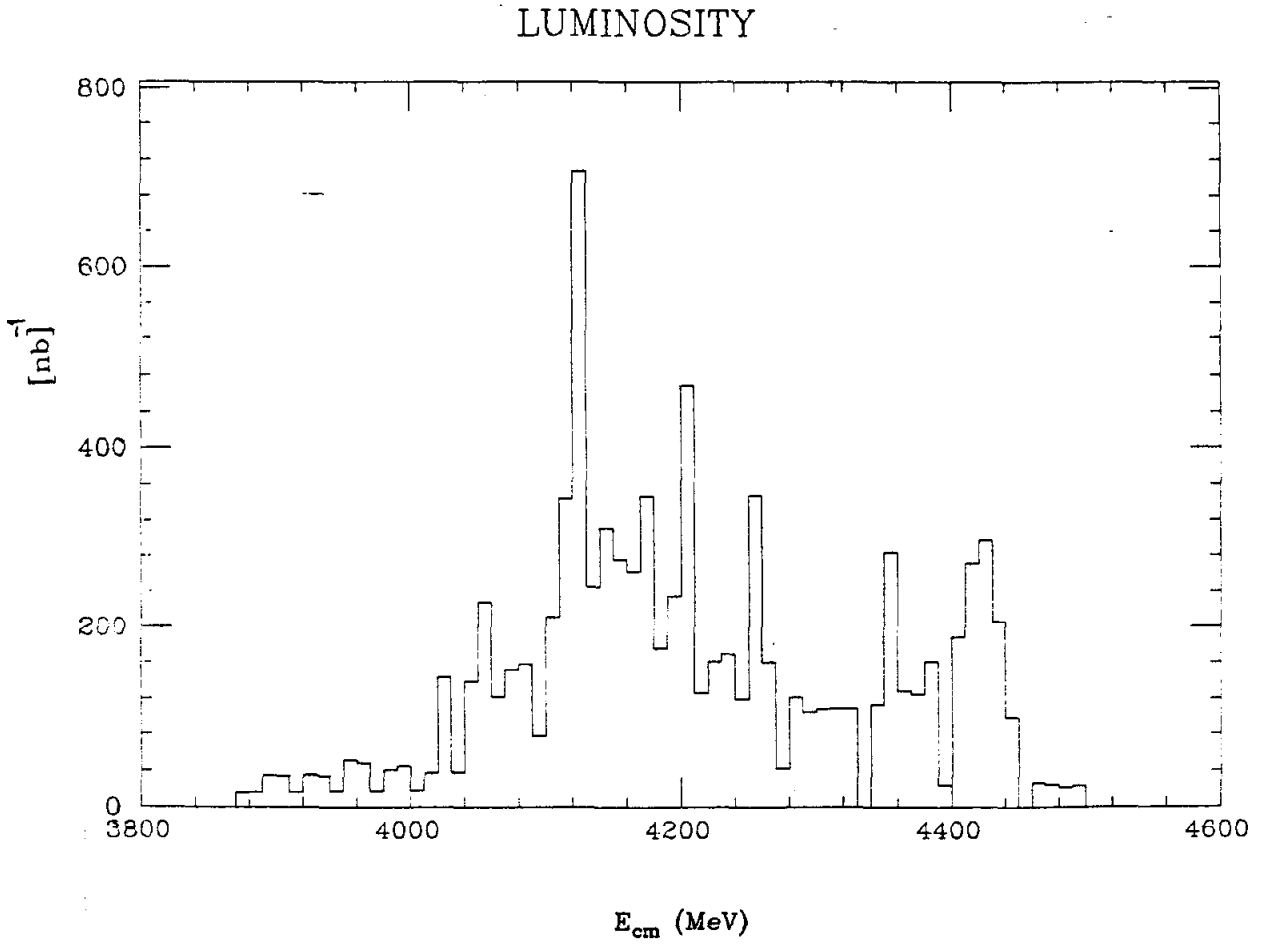

Figure 15. Accumulated luminosity as a function of center of mass energy (E_{cm}) from Spring 79 and Spring 80 data.

Data taking was normally interrupted about every two weeks for special calibration runs[1] of the NaI(Tl)-crystals. Two different sources of gamma rays of known energy were used to calibrate the response of the NaI(Tl)-crystals and their associated electronics, in order to correct for any longterm changes of the system.

One calibration was done by using 0.661 MeV photons from ^{137}Cs. The second calibration used 6.31 MeV photons , which were obtained by bombarding ^{19}F with 340 KeV protons from the Van de Graaff accelerator and inducing the nuclear reaction

$$p + {}^{19}F \rightarrow {}^{20}Ne^{*} \rightarrow {}^{16}O^{*} + \alpha$$

with $^{16}O^{*} \rightarrow {}^{16}O + \gamma$.

§3.2 DATA CALIBRATION

Before the detector's raw signals for each recorded event could be analysed by the offline analysis program, one had first to find calibration constants for the NaI(Tl) crystals and the central tracking chambers.

For the NaI(Tl) crystals ,this was done by first using the ^{137}Cs calibration data and the Van de Graaff calibration data and finally Bhabha events and $\gamma\gamma$ events for the so called Bhabha calibration.

The NaI(Tl) electronics split the incoming photomultiplier signal into two seperate channels: a low chanel for measuring energies in the range 0−160 MeV and a high channel (attenuated by a factor 20) to cover the range 0−3200 MeV . Both channels were then digitized with a 13-bit ADC[2] . The ADC-channel is assumed to depend linearly on the deposited energy in the crystal.One has therefore to determine two pedestals and two slopes for each crystal. The two pedestals and the ratio of the high channel slope to the low chanel slope were derived from uncompressed events. The

[1] I. Kirkbride et. al. , IEEE Trans. on Nucl. Sci. NS-26, 1535 (1979).

[2] G. Godfrey , Crystal Ball - note 121 (1978).

slope ratio was calculated by requiring the same energy to be measured in the overlap region of the two chanels . The low channel slope itself was found by first using the ^{137}Cs calibration and then the Van de Graaff calibration . These preliminary constants allowed one to do a first pass analysis of the data and to strip Bhabha events and $\gamma\gamma$ events from the data set. The final slopes were then extracted by constraining the energy of the observed Bhabha shower to the beam energy . The resulting slopes give a resolution of $\frac{\sigma_E}{E} = 1.8\%$ for selected 2.3 GeV Bhabha electrons. The Spring 79 and Spring 80 data have 12 different Bhabha calibrations. More details about the calibration procedure can be found in Reference[3] .

The central tracking chambers also have to be calibrated periodically. These calibrations allow one to correct for any possible physical displacement of the chambers and for changes in the read out system that might occur over longer time periods.

The magnetostrictive sparkchambers and the MWPC, as well as the proportional tube chambers ,were calibrated by using Bhabha events. The calibration constants were then adjusted so that collinearity of the chamber tracks and agreement with the direction cosines from the Bhabha electron shower centers in the NaI ball was achieved. More details about the tube chamber calibration are given in Appendix A .

§3.3 OFFLINE ANALYSIS PROGRAM

The standard offline analysis program reads the recorded detector signals for each event and attempts to reconstruct the event final state. The program consists of five separate analysis steps:

ENERGY - uses the appropriate energy calibration and calculates the deposited energy in each NaI-crystal.

CONREG - finds sets of crystals , that are neighbors to each other that and surpass a

[3] M. Oreglia , SLAC-report-236 (1980).

certain energy threshold (10 MeV),calling it "connected region".

BUMPS - searches for local maxima of energy deposition in each connected region and calls them "bumps". Starting with the biggest crystal energy ,it checks the other connected region crystals to see if they can be explained as being part of the bumps already found. This is done with the "bumps discriminator " function. This function requires the energy E_i of the crystal i in the connected region to be smaller than the energy threshold $E(\phi)$, where ϕ is the opening angle between the bump center and the crystal i . If $E_i > E(\phi)$ then a new bump is formed and the remaining crystals are checked. The function $E(\phi)$ was derived on a numerical basis by looking at data and has the form[4]:

$$E(\phi) = \begin{cases} E_b, & \text{if } \phi < 12^0 \\ E_b \cdot 0.72 \cdot e^{-9.4(1-\cos\phi)}, & \text{if } 12^0 < \phi < 45^0 \\ 0, & \text{if } \phi > 45^0 \end{cases} \tag{3.1}$$

with E_b being a estimate of the bumps energy based on the $\sum$4-energy (energy deposited in the biggest bump crystal (bump module) and its closest 3 neighbor crystals) .

The "bumps discrimator" function has also deficiencies which are due to fact that the routine does not know whether a bump stems from a charged hadron or from a electromagnetic shower. It has to use some average criterion, although the two types of showers behave quite differently. Since hadronic showers have a very irregular behavior , the routine tends to label shower fluctuations as new bumps ("split offs") . Electromagnetic showers occasionally also yield low energy "split off" bumps , but in general ,the routine does not separate neighboring electromagnetic showers as well as it could if charged tracking information would be available at this step of the event analysis. The opening angle between two electromagnetic showers which gets resolved as two bumps with 50% probability is $\approx 18^0$. For π^0 particles ,this means that the two resulting γ particles can be separated with this probability at a π^0 energy of $E_{\pi^0} \approx 800\,\text{MeV}$.

A second deficiency of the routine is that the energy fraction $E(\phi)/E_b$ is only a function of the angle ϕ , although it is well known that low energy electromagnetic showers fluctuate more

[4] R. Partridge , Crystal Ball - note 6 (1976).

than high energy ones.

At a later step of the data analysis , when charged tracking information is available , another attempt is made to suppress "split off" tracks with the routine *SPLIT*.[5] The routine *GAMFIND* is also used at a later stage to achive better neutral track separation.

CHGTKS - is the fourth step in standard offline analysis program . It tries to reconstruct the charged particle trajectories from the tracking chamber information.[6] In a first step it searches and reconstructs charged tracks by using only the tracking chamber information alone. These Interaction-Region-tracks (IR-tracks) also fix the z-position of the primary event vertex, assuming $x = y = 0$. In a second step ,the routine tries to match these IR-tracks with the bumps found in the previous analysis stage. Charged tracks , that did not produced enough sparks in the tracking chambers to establish them as IR-tracks , are also reconstructed by "tagging" the associated bumps with the the so far unassociated chamber sparks. The direction cosines of "tagged" tracks are given by the bump module. More details about the angular resolution of the charged tracks will be given later in connection with the errors used for the kinematic fitting program SQUAW.

Matching the chamber information with the ball information is not always successful. If a charged track leaves few sparks in the chambers and cannot be found as a IR-track , it sometimes happens that the associated energy bump in the ball will not be tagged as a charged track. Since these bumps will be called neutral tracks , they will manifest themselves later in the γ spectrum as a peak at $\approx$ 210 MeV , which is typical for the observed charged particle spectrum due to energy loss by minimum ionisation in the NaI-shell. This contamination of charged particle tracks in the γ spectrum is called "charged punch through". One reason for "charged punch through" is an incorrect reconstructed z-vertex , causing the charged track to tilt so much that it cannot be successfuly associated with the corresponding track bump anymore. If this charged track was a IR-track ,then it will be given zero energy. A second possibilty for "charged punch through"is that

---

[5] K. Koenigsmann, F. Bulos , Crystal Ball -note 254(1980).

[6] M. Oreglia, SLAC-report-236 (1980),Appendix F .

the hadronic shower was very irregular towards one side, or that there was a second high energy shower close by, which made the bump discriminator suppress the first bump. The amount of "charged punch through" is dependent on the chamber efficiency as well as on the angular windows ("tagging windows") used to match the sparks with the bumps of energy deposition in the ball. How to determine the fraction of "charged punch through" will be described later in Chapter 5.

Increasing the size of the angular "tagging windows" decreases the amount of "charged punch through" , but at the same time increases the probabilty for "overtagging" true γ particles with nearby chamber hits. There are basically three sources for these chamber hits.

One source consists of sparks from charged tracks of the primary event vertex, where a wrong z-vertex was reconstructed. Chamber hits from tracks of secondary vertices (strange particle decays like K^0,Λ) are also likely to be misused for "overtagging" of neutral tracks. A second source corresponds to chamber noise hits that are either randomly distributed or that are at well localized positions due to breakdowns in the chambers or due to wandering fiducials that are not perfectly traced by the analysis program. More details about the removal of the localized noise hits will given later. The third source of chamber hits for "overtagging" are the combinatorical hits that were inherent in the spark chambers and MWPC. This problem did not exist for the tube chambers that were later installed.

The fraction of overtagged neutral tracks can be measured by comparing the number of π^0's , that can be found by pairing charged tracks with neutral tracks with the number of π^0's from pairing neutral tracks among each other.

The proportional tube chambers with charge division read out that were used in the Fall 81 data had a different tracking code which used only ϕ information for track reconstruction.

ESORT -[7] this routine assigns the measured crystal energies to each bump, assuming that they stem from electromagnetic showers. The direction cosines of neutral tracks are also determined by this routine . The bump module is divided into 16 hypothetical submodules , and the routine

[7] A. Liberman, F. Bulos, Crystal Ball-note 233 (1977).

then compares the observed energy distribution in the bump module and its neighbor crystals with the expected average energy distribution in these crystals , assuming that the photon impacted at a certain submodule center. In an iterative procedure ,it searches for the submodule that minimizes the difference between the observed and the predicted energy distribution. The direction cosines for that submodule are then used as the direction for the photon . The resulting energy and angular resolution of this routine for photons will be given later in connection with the discussion of the errors used for the kinematic fitting program SQUAW.

The result of the standard offline analysis program is a list of charged and neutral tracks in the "track bank". These reconstructed tracks do not ,of course , always correspond to true physical particles , which means that one measures the correct charged and neutral event multiplicity only with a certain probabilty. This detector efficiency has to be estimated with the help of a Monte Carlo simulation of the Crystal Ball experiment. More details about the Monte Carlo program will be given later.

§3.4 HADRON SELECTION

Most of the events that the experiment had triggered on are not of the desired type $e^+e^- \rightarrow hadrons$. In the center of mass energy region $E_{cm} \approx 4\,\mathrm{GeV}$ at which the data for this analysis were taken, only about 2% of the recorded events are hadronic events. The main sources of the background events are : beamgas events , cosmics , QED events such as (radiative) Bhabha events and $e^+e^- \rightarrow \gamma\gamma(\gamma)$, two photon events and τ-events. Most hadronic events can be distinguished from these other events ,since they tend to have high multiplicity and an isotropic energy flow. The background events are either asymmetric (cosmics, beamgas events,two photon events) or have low multiplicity(QED).

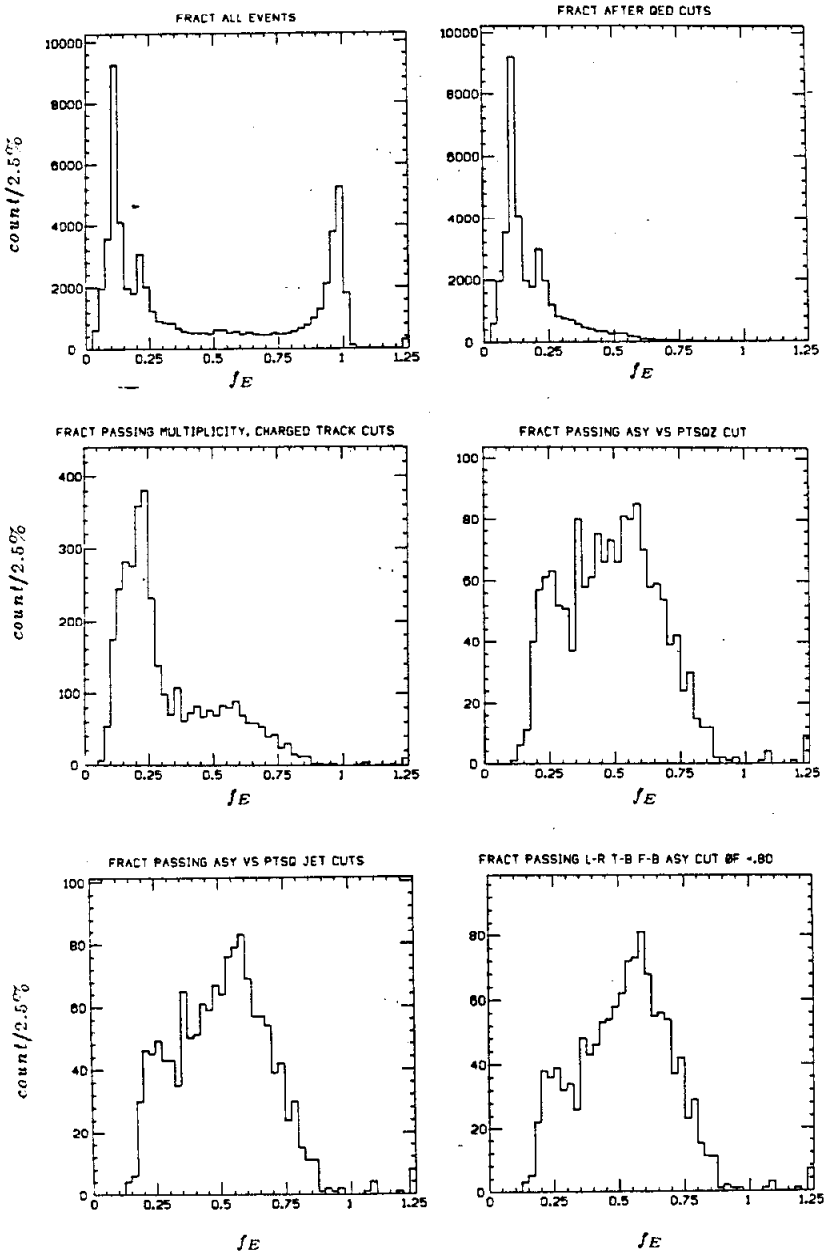

Figure 16. Total energy fraction f_E before and after each of the five hadron selection cuts.

Since in this analysis we are only interested in hadronic events , criteria were developed to select hadrons and write them out to tape for further analysis. The specific set of hadron selection cuts used is decribed in detail else where.[8] Only a brief summary of the cuts will be given here.

An event is assumed to be a hadron if none of the following cuts is fullfilled:

1). QED-cut: an event is called a showering QED-event if there are either more than 2 tracks with the second most energetic track having $x > .5$ ($x = E_{track}/E_{beam}$) or if the event has $N_{conreg} < 4$ (N_{conreg} = number of connected regions) and the most energetic track has $x > .75$.

2). Multiplicity-cut: if $N_{conreg} < 3$ or if there is no charged track and $f_E < .35$, with f_E beeing the total energy fraction . ($f_E = E_{ball}/E_{cm}$)

3). low $p_{t_z}^2$-cut : (p_{t_z} = transverse momentum to z-axis)

$$A_{sy} > c_1(f_E) \cdot (log(p_{t_z}^2) - c_2)$$

with $A_{sy} = \sum_i \vec{E}_i/E_{ball}$ and $p_{t_z}^2 = \sum_i p_{z,i}^2$, where i runs over all crystals of the ball. c_2 is an offset constant that varies with E_{cm} and c_1 is a function of f_E that becomes very big for $f_E > .5$, making the cut effectively independent of A_{sy}. This cut mostly removes beam gas events.

4). $p_{t_{jet}}^2$-cut : ($p_{t_{jet}}$= transverse momentum to jet axis)

$$A_{sy} > c_3 \cdot (log(p_{t_{jet}}^2) - c_4)$$

with $p_{t_{jet}}^2 = \sum_i \vec{E}_i^2 - (\vec{E}_i \cdot \vec{n}_{jet})^2$,where i runs over all crystals of the ball and $\vec{n}_{jet}$ is the normalized vector of the jet axis. c_3, c_4 are beeing constants. This cut removes cosmics as well as $e^+e^- \rightarrow \mu^+\mu^-$ events.

5). Forward-Backward-Asymmetry-cut: this cut removes residual beamgas events that survived tha low $p_{t_z}^2$-cut, by requiring

$$A_{FB} > .8$$

[8] W. Lockmann SLAC-Pub 3030(1983).(in preparation)

with $A_{FB} = |E_{+z} - E_{-z}|/E_{ball}$, where $E_{\pm z}$ is the energy in the forward(backward) ball hemisphere.

Figure 16a shows the observed total energy fraction f_E for all events. Figure 16b-f gives the same plot after each of the five cuts described above. In order to get optimal separation of beamgas events from hadrons , separate beam runs were used to tune the cuts . This also allows one to estimate the fraction of beam gas event that were mislabeled as hadrons. The beam gas contamination of the final hadron selected sample is $\approx 10\%$. About 50% of the $e^+e^- \to \tau^+\tau^-$ events are also misidentified as hadrons. This is due to the fact that τ-leptons decay into hadrons with a substantial branching fraction , which makes the events look very similar to ordinary hadrons.

The hadron selection efficiency for open charm events has been determined by Monte Carlo events. $F^{(*)}\overline{F}^{(*)}$-events and $D^{(*)}\overline{D}^{(*)}$-events were generated and allowed to decay into various final states according to branching ratios that are given by the contant matrix element model of Quigg and Rosner.[9] These generated events were then run through a detector simulation program that propagates all long-living, final-state particles through the Crystal Ball detector. Hadronic interactions ,as well as electromagnetic interactions between these final state particles and the detector material ,are then simulated using the High-Energy-Transport-Code (HETC)[10] and the Electron-gamma-Shower (EGS3)[11] Finally these simulated events are given the same data structure as normal data events , so that the same analysis programs can be run on the Monte Carlo events as well as on the normal data events. The hadron selection efficiency was then determined by running the Monte Carlo events through the hadron selection cuts. For $F\overline{F}$- events the resulting efficiency ϵ_{hadsel} is 0.95 ± 0.01. For $F^*\overline{F}^{(*)}$- events the efficiency is $\epsilon_{hadsel} = 0.96 \pm 0.01$, which is almost the same. Although the event multiplicity is higher due to the additional transition γ particles, the measured energy distribution is almost the same , since these additional γ particles carry only a small fraction of the event energy. For $F^{(*)}\overline{F}^{(*)}$-events , where one of the F mesons has the specific

[9] C. Quigg, J. Rosner, Phys. Rev. D17 (1978)p.239

[10] T. A. Gabriel et. al., Oak Ridge National Laboratory Report, ORNL/TM-7123, (1981)

[11] R. L. Ford, W. R. Nelson, Stanford Univ. Report, SLAC-210 (1978).

decay mode $F^{\pm} \rightarrow \eta\pi^{\pm}$, the hadron selection efficiency was also determined. The obtained number is $\epsilon_{hadsel} = 0.97 \pm 0.01$. The resulting ϵ_{hadsel} for Monte Carlo events of different center of mass energy E_{cm} indicate that the efficiency appears to be almost independent of the energy difference $E_Q = E_{cm} - E_{threshold}$, with $E_{threshold}$ being the energy threshold for the process $e^+e^- \rightarrow F^{(*)}F^{(*)}$.

The result of the hadron selection from all the data are shown in Figure 17. The plot shows the raw value of $R = \sigma_{hadron}/\sigma_{\mu\mu}$ as a function of E_{cm}. The hadronic cross section σ_{hadron} used is only a "raw" number that was calculated by dividing the number of selected hadrons in a certain E_{cm}-bin by the corresponding total integrated luminosity that was measured by the small angle Bhabha luminosity monitor. Figure 17 is not intended to be a precise measurement of R in the 4 GeV region , but it should give the qualitative behavior of R in the range of 3.87 GeV $-$4.50 GeV . This plot could serve the reader as an illustration when , in subsequent chapters , the whole data sample in the 4 GeV region is divided into several center of mass energy steps.

The plotted R values in Figure 17 ,are on the average about $25\% - 30\%$ too large, since no corrections have been applied . There are several sources for corrections of the R values. Some corrections vary from point to point and some vary only slowly over the whole E_{cm} region. The following list gives some very rough average numbers: beam gas contamination $\approx -10\%$, radiative corrections to the hadronic cross section (initial state radiation and vacuum polarisation) $\approx -20\%$, τ-event contamination $\approx -5\%$, 2 photon events $< -3\%$, correction for hadron selection efficiency $\approx 5 - 10\%$.

In connection with the hadron selection a monitoring of the tracking chamber efficiencies was done. The efficiencies were obtained using Bhabha events and measuring with what efficiency a spark was found for a certain gap. The measured efficiencies where then used in the Monte Carlo program . Localized noise hits ("pips") that occured in the spark chambers were also removed at this point of the data preparation. These "pips" were traced and removed by cutting out about 0.62% of the solid angle covered by the chambers and removing in this way an average of

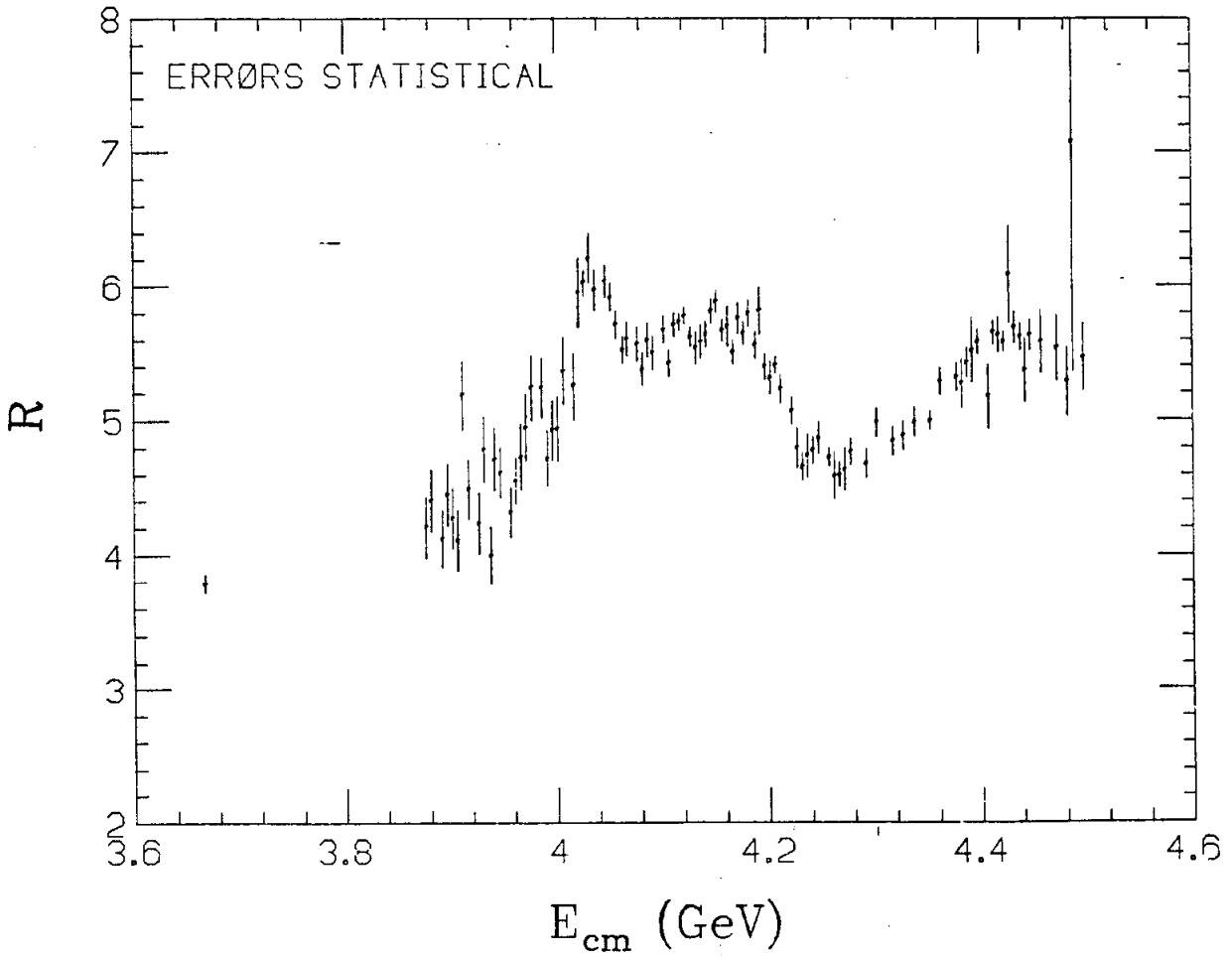

Figure 17. Uncorrected values of $R = \sigma_{hadron}/\sigma_{\mu\mu}$ in 4 GeV region.

of 14.4% of the chamber hits. More details about the monitoring of the chamber efficiencies and the removal of the localized noise hits are described in Appendix B.

§3.5 NEUTRAL TRACK SEPARATION

After the data had been hadron selected a routine was applied to all neutral tracks in the event in order to find tracks that actually were energy depositions from more than one γ but had not been separated by the standard offline analysis code. The merged γ pairs come either from fast π^0's or from randomly overlapping γ's . A routine called *GAMFIND*[12] had been writen and applied to the data that attempted to separate such merged energy depositions. *GAMFIND* assumes every neutral energy deposition to come from one or two γ's and decides between one of the two possibilities. The decision is done by first assuming that there were two γ's and using an energy division algorithm that gives the energies of the two "photons" and their opening angle as well as the maximum likelihood ratio of fitting the observed energy distribution to a two γ hypothesis and to a one γ hypothesis. After having obtained these four quantities a cut is made in this four-dimensional parameter space to distinguish two γ showers from single γ showers. The cuts were developed on Monte Carlo data . The design philosophy for this cut was to minimize the fraction of truly single photon showers that get lost by dividing them and creating two fake photons. The routine is able to decrease the opening angle between two γ's where 50% of them get merged by the standard offline analysis program from $\approx 18^0$ down to $\approx 11^0$. More details about the performance of this routine are given in Appendix C.

[12] R. Horisberger "Neutral track separation with GAMFIND" Crystal Ball Offline Workshop (August 29- September 2, 1983).

Chapter 4

INCLUSIVE η CROSS SECTION

§4.1 INTRODUCTION

The charmed F meson is expected in most theoretical models to have a substantial branching ratio for the inclusive η decay $F^{\pm} \rightarrow \eta X$, where X stands for "anything".[1] The DASP collaboration[2] had reported the observation of a strong increase in the inclusive η production $(e^+e^- \rightarrow \eta + X)$ at $E_{cm} \approx 4.4\,\mathrm{GeV}$ (and possibly at 4.17 GeV) compared to 4.03 GeV. They interpreted this as evidence for production of F mesons. This was supported by their observation of $e^+e^- \rightarrow F^*F \rightarrow \gamma FF$, with $F^{\pm} \rightarrow \eta\pi^{\pm}$ at $E_{cm} = 4.42\,\mathrm{GeV}$.

Since the Crystal Ball detector can measure electromagnetic showers very well it is possible to detect η's with good efficiency and with good mass resolution via its 2 γ decay mode. In this chapter a measurement of the inclusive η production cross section will be presented that covers an E_{cm} range similar to that of the DASP measurement. (The Crystal Ball collaboration has also made such such a measurement.)[3]

---

[1] M.Einhorn, C.Quigg, Phys. Rev. D12, 2015(1975); J.Ellis, M.Gaillard, D.Nanoupulos, Nucl. Phys. B100, 313(1975); C. Quigg, J.Rosner, Phys. Rev. D17, 239(1978); D. Fakirov, B.Stech, Nucl. Phys. B133, 315(1978).

[2] R. Brandelik et. al., Phys. Lett. 70B, 132(1977); 80B, 80B, 412(1979); R. Brandelik et. al., Z. Physik, C1, 233(1979).

[3] R.Partridge et. al. , Phys.Rev.Lett.47,760,1981.

The analysis presented here differs from the previous Crystal Ball study in that it looks only for η's with $E_\eta > 700\,\mathrm{MeV}$. This selection significantly improves the signal to background ratio in the η region of the invariant $\gamma\gamma$ mass plot. The η energy spectrum generated by the F meson decay Monte Carlo program also indicates that there is still a substantial fraction ($\approx 70\%$) of η's above the energy cut $E_\eta > 700\,\mathrm{MeV}$. In addition is the Fall 81 data set at $E_{cm} = 4.33\,\mathrm{GeV}$ included here which was not available in the previous analysis. The older data sets of Spring 79 and Spring 80 have also both been recalibrated and reanalyzed . This should minimize any systematic differences between the two separate data sets. Since the previous measurement, the offline analysis code has also undergone various changes which have improved the charged particle tracking .

§4.2 DATA ANALYSIS

The whole data sample in the center of mass energy range $E_{cm} = 3.86\,\mathrm{GeV} - 4.50\,\mathrm{GeV}$ has been divided into 8 different energy steps. The way these energy steps were determined was partially motivated by the structure of R and by the distribution of the accumulated luminosity over the whole E_{cm} region. The Fall 81 data set with $E_{cm} = 4.33\,\mathrm{GeV}$ forms a separate energy "step" since it has good statistics and a different central tracking chamber. Table 1 gives a list of the different center of mass energy steps with their ranges , the average step energy ,and the total integrated luminosity for each step. The different ranges of the center of mass energy steps were by part motivated by the distribution of the integrated luminosity over the center of mass energy region and by part by the center of mass energy steps that had been chosen by the DASP experiment and by the Crystal Ball experiment in its previous inclusive η measurement.

E_{cm} steps for inclusive η measurement			
Step	E_{cm}-range [GeV]	$<E_{cm}>$[GeV]	Luminosity$[nb^{-1}]$
1	3.860-4.000	3.943	405
2	4.000-4.060	4.040	604
3	4.060-4.140	4.110	2015
4	4.140-4.220	4.179	2197
5	4.220-4.300	4.256	1225
6	– 4.330	4.330	1506
7	4.300-4.380	4.344	976
8	4.380-4.500	4.422	1442

Table 1. Energy steps used for measurement of inclusive η cross section

The actual measurement of the number of η's in a given E_{cm} step consists of two parts. The tracks labeled neutral in the trackbank of a given event are first paired with each other ,and the invariant mass of each pair is plotted. After having run through all the events of a certain E_{cm} step , the number of entries forming a peak at the η-mass is then calculated. This is done with the help of a curve fitting program that fits a gaussian curve together with a background function to the η peak in the invariant mass histogram.

There are several cuts that a neutral track from the trackbank has to pass before it is used to calculate invariant masses.

1). $|\cos\theta_\gamma| < 0.92$, with θ_γ being the angle between the γ direction and the direction of the $e^\pm$ beam. This cut excludes tracks that were found by the endcap crystals , but allows tracks in the central ball that are fairly close to the tunnel boundary. For γ showers entering the tunnel modules this results in a somewhat worsened energy resolution , but on the other hand the larger solid angle allows one to reconstruct more η's .

2). $E_\gamma > 20\,\mathrm{MeV}$

3). Cut on the lateral shower distribution (pattern cut): This cut is supposed to reject neutral tracks with an energy distribution , that is inconsistent with coming from a single electromagnetic shower. The cut calculates the ratios $r_{1,4} = E(\sum 1)/E(\sum 4)$ and $r_{4,13} = E(\sum 4)/E(\sum 13)$, where $E(\sum 1)$ is the energy of the central crystal , $E(\sum 4)$ is the energy of the bump module and its 3 closest neighbors ,and $E(\sum 13)$ is the energy of the bump module and its 12 neighbors. The actual pattern cut is done by cutting along a boundary of the two ratios $r_{1,4}$ and $r_{4,13}$, where the shape of the boundary region changes as a function of $E(\sum 13)$. This cut is supposed to have a transmission efficiency for electromagnetic showers that is independent of the shower energy. The pattern cut was not applied to neutral tracks found by the routine *GAMFIND* because ,in general, they would not pass the cut due to the overlapping showers. More details about the routine *PATCUT* and its performance is given in Appendix D.

4). Split off cut: This routine attempts to remove fake low energy neutral tracks ("split offs") , that are actually part of the energy deposition of a nearby track. There are several criteria used to label a neutral track a split off track. In order to remove "split offs" from close-by interacting hadrons one requires the opening angle between the two tracks to be less than a certain critical angle , which is a linear function of the "split off" energy itself. For "split offs" from electromagnetic showers a similar cut is applied but with a different critical angle. "Split offs" that don't seem to be associated with any nearby tracks are removed by only using the energy distribution in the crystals. These "split offs" tend to be low in energy and are assumed to come from interacting neutrons that were released from a hadronic shower in a different place in the ball. A neutral track can also be called a "split off" when there is a zero energy IR-track pointing towards its vicinity. More information about the routine

SPLIT and the energy spectrum of "split offs" can be found in Reference.[4]

5). π^0-subtraction: The idea of π^0-subtraction is to remove all γ's in an event that can be explained as coming from $\pi^0 \rightarrow \gamma\gamma$. Since in the 4 GeV region the number of η decays with $\eta \rightarrow \gamma\gamma$ is only about 4% of the number of π^0 decays, a removal of γ's from π^0 decays would greatly reduce the combinatorical background under the η peak and ,therefore, improve the signal to noise of the η peak. The π^0-subtraction used in this analysis is based on the global π^0 reconstruction routine *PAIR* . The routine searches simultaneously for all possible pairs of γ's that have an invariant mass close to the π^0 mass , without pairing a single γ more than once. The deviation of the invariant mass m_i of the pair i from the π^0 mass m_{π^0} is measured by $\chi_i^2 = (m_i - m_{\pi^0})^2/\sigma^2_{m_{\gamma\gamma}}$. A certain configuration of pairs is then accepted when $\chi_i^2 < 5$ for all pairs i and when the combined $\chi^2 = \sum_i \chi_i^2$ for the whole configuration is less than a certain χ^2_{min} , that corresponds to a confidence level cut of 0.05. From all the configurations passing the above cuts the one with the lowest χ^2 is finally used. The neutral tracks that were used for π^0-subtraction had to pass the $|\cos\theta_\gamma|$-cut [1).] and the minimal energy cut [2).] and the split off cut [3).]. More details about the routine *PAIR* are given in Chapter 6 .

The $\gamma\gamma$ invariant mass plots were generated with three different sets of cuts. The following list gives the cuts that the neutral tracks had to pass:

a.) Cut 1).+2). "minimal cut"

b.) Cut 1).+2).+5). "π^0-subtraction"

c.) Cut 1).+2).+4).+5). "π^0-subtraction and pattern cut"

Figure 18 shows the 3 invariant mass plots that were obtained with the 3 different sets of cuts . These plots combine all the data of the 8 energy steps taken together. Also shown are the results from the curve fitting program.

---

[4] K. Koenigsmann, F. Bulos, Crystal Ball-note 254(1980).

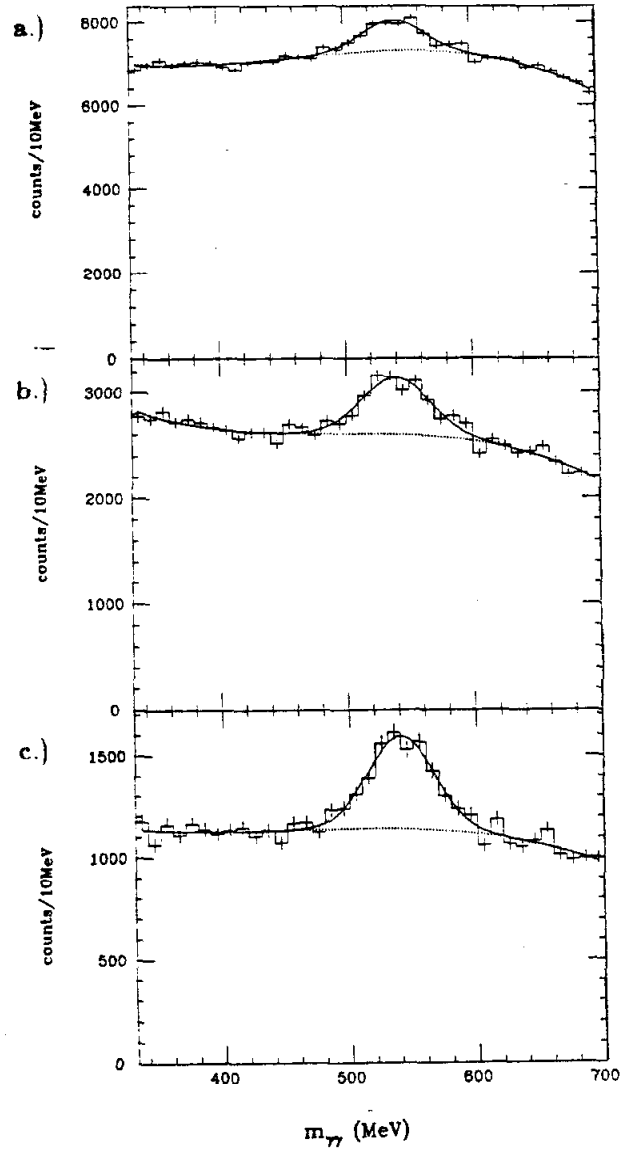

Figure 18. Invariant mass plots with fit curves to the η peak for all E_{cm} steps combined. The 3 different plots correspond to the sets of cuts that are discussed in the text. a). "minimal cut". b). "π^0-subtracted". c)."π^0-subtracted and pattern cut".

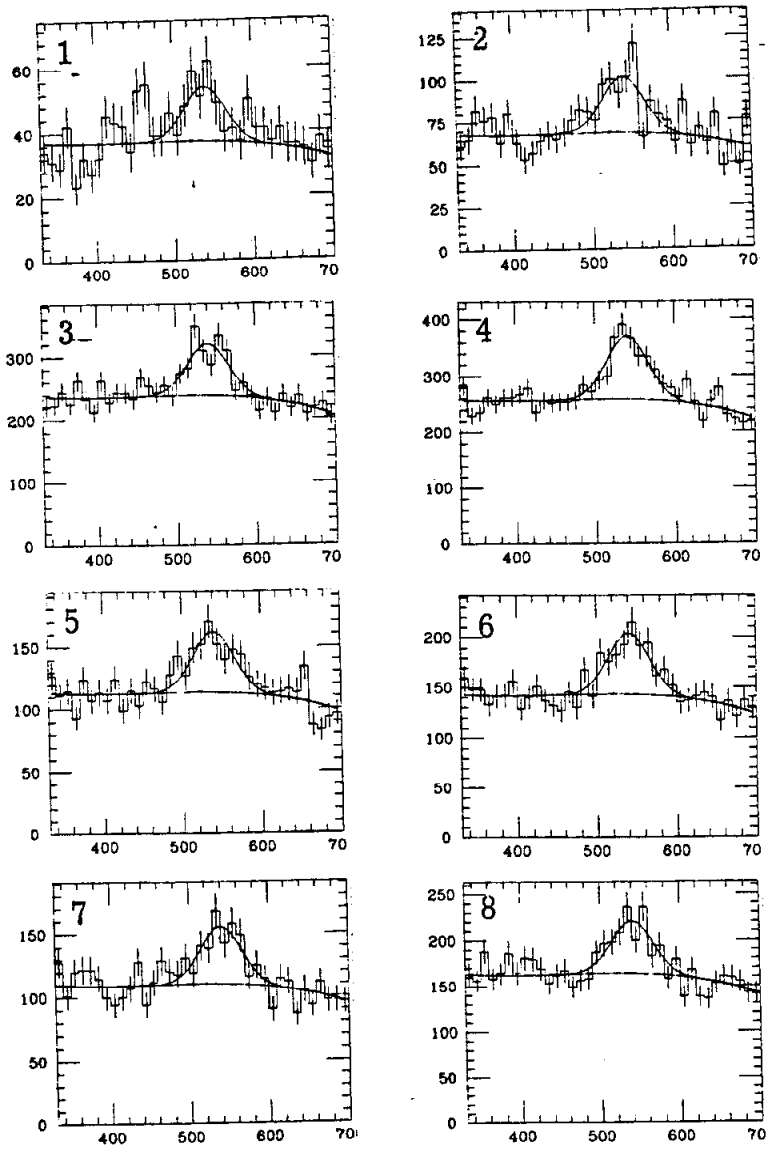

Figure 19. Invariant mass plots with fit curves to the η peak for the 8 different E_{cm} steps. The plots are π^0-subtracted and pattern cut .

The fit function used consists of a gaussian with variable mean,width and amplitude together with a background function which is a linear combination of Chebyshev polynomials up to the 4^{th} order. The resulting means,widths and ratios of the Chebyshev coefficients of these combined statistic plots were then used to fix he shape of the fit functions for the plots of the individual E_{cm} steps. Fixing this shape for the different E_{cm} steps was done because there is no systematic change of the background shape noticeable over the whole E_{cm} region .This is also confirmed by the good confidence levels of the fits . Fits were also done without fixing the background shape .These results were consistent with the previous fits. Fixing the background shape seems to help stabilizing the fits, especially for the plots with poorer statistics. Figure 19 shows the $\gamma\gamma$ invariant mass plots for the 8 different energy steps with the superimposed fitted curves . Although fit results were obtained for all three sets of cuts only the plots with the third set of cuts ("π^0-subtraction and pattern cut") are shown . These plots have the best signal to noise and are the ones that are used for the final results.

§4.3 EFFICIENCIES

Before the η production cross section can be calculated the efficiency ,ϵ_{det}, for detecting the two photons has to be known. This efficiency was obtained by using Monte Carlo events. A certain number of Monte Carlo events with η's were generated and analyzed in exactly the same manner as data events. The efficiency ,ϵ_{det}, was then defined as the number of η's that could be reconstructed divided by the number of η's that were generated . The number of reconstructed η's can be obtained by either fitting the η peak in the invariant mass plot or by correlating the energy and direction cosines of the two generated photons with the tracks found by the analysis code. For the finals result the second method was used.

Since the average event multiplicity changes for the different E_{cm} steps one has to apply multiplicity corrections , to get the correct efficiencies ϵ_{det}. In order to obtain these corrections one needs to know how ϵ_{det} changes as a function of the observed average event multiplicity $< n_{obs} >$

. This dependence was obtained by generating Monte Carlo event with different average event multiplicity and then plotting the obtained ϵ_{det} as a function of $< n_{obs} >$. Within the range $< n_{obs} > \approx 8-10$ the efficiency ϵ_{det} seems to have an almost linear dependence. There appears to be no dependence of ϵ_{det} on the type of event generator used. The two efficiencies obtained from a phase space Monte Carlo and from a charmed F Monte Carlo agreed very well when restricted to the same range of generated event multiplicity.

Using $< n_{obs} >= 10.50$ as a average observed multiplicity over all E_{cm}-steps the following efficiencies for the three different sets of cuts were obtained: $\epsilon_{det} = 53.5\% \pm 2.5\%$ for "minimal cut"; $\epsilon_{det} = 45.0\% \pm 2.1\%$ for "π^0-subtraction"; $\epsilon_{det} = 35.5\% \pm 2.0\%$ for "π^0-subtraction and pattern cut". The errors quoted are due to the limited Monte Carlo statistics. The systematic error of the value of ϵ_{det} is estimated to be 15%. More details about this estimate are given below. For the 8 different E_{cm} steps, $< n_{obs} >$ changes very slowly. The first step , which is still below D^*D^*-threshold , has the lowest multiplicity with $< n_{obs} >= 9.70$. All the other steps are in the range $< n_{obs} >= 10.38-10.73$. Correcting ϵ_{det} with a slope of 4.4% per unit of $< n_{obs} >$, this results in $\epsilon_{det} = 32.0\% - 36.5\%$ for the third set of cuts ("π^0-subtraction and pattern cut"). These efficiencies contain the hadron selection efficiency since the all the Monte Carlo generated events were run through the hadron selection cuts .

The efficiency ϵ_{det} was also determined by a second method . This method is based on merging the two photon showers of the Monte Carlo generated η into real data events. The efficiency ϵ_{det} was then obtained by comparing the number of η's reconstructed by the analysis code with the number of η's merged into the data. Since the event multiplicity gets increased one has to apply the corresponding multiplicity corrections to get the proper efficiency numbers. The two methods were compared by merging Monte Carlo η's into Monte Carlo data. The efficiency derived from merging η's into the event turned out to be smaller than the efficiency obtained with the first method. This is not unexpected since in a real event with a η carrying about 20% of E_{cm} , there are kinematical correlations between the photons of the η and the other tracks due to 4 momentum conservation . This correlation effectively improves the η detection efficiency since there

are fewer overlaps with other tracks compared to the situation where no such correlation exists. The difference in efficiency observed between the two methods in the Monte Carlo data was used to correct the efficiency obtained from merging η's into real data events. The final resulting efficiencies agreed within $7-15\%$ of the values of ϵ_{det} quoted above for the three different sets of cuts. The systematic error for ϵ_{det} used for the calculation of the cross section ,is therefore ,estimated to be 15% .

§4.4 RESULTS FROM INCLUSIVE η MEASUREMENT

The inclusive η production cross section σ_η or the process $e^+e^- \rightarrow \eta + X$ can now be calculated according to:

$$\sigma_\eta = \frac{N_\eta}{\mathcal{L} \cdot \epsilon_{det} \cdot BR(\eta \rightarrow \gamma\gamma)} \tag{4.1}$$

with N_η being the amplitude of the gaussian that was fit to the η peak. ϵ_{det} is the efficiency as described in the previous chapter , and $\mathcal{L}$ is the integrated luminosity for each separate E_{cm} step as given in Table 1 . Instead of presenting the resulting cross section σ_η, the ratio $R_\eta = \sigma_\eta/\sigma_{\mu\mu}$ was calculated , where $\sigma_{\mu\mu}$ is the QED point cross section for $e^+e^- \rightarrow \mu^+\mu^-$.

Table 2 gives R_η for the production of η's with $E_\eta > 700\,\mathrm{MeV}$, averaged over $E_{cm} = 3.860-4.500\,\mathrm{GeV}$, for the three different sets of cuts as described in previous sections.The average center of mass energy for this energy range is $< E_{cm} >= 4.230\,\mathrm{GeV}$. The errors shown are statistical only. An additional systematic error of 15% also has to be included. The final results for R_η in Table 2 show that the effects of the different cuts applied (π^0-subtraction ,"split off" cut, pattern cut) are sufficiently similar in Monte Carlo events as in real data events.

R_η with $E_\eta > 700\,\mathrm{MeV}$ for all E_{cm}	
cut	R_η
"minimal cut"	.43 ± .06
"π^0-subtracted"	.41 ± .06
"π^0-subt.+pattern cut"	.43 ± .04

Table 2. R_η with $E_\eta > 700\,\mathrm{MeV}$ for $E_{cm} = 3.86 - 4.50\,\mathrm{GeV}$

Table 3 and Figure 20 give the results for R_η with $E_\eta > 700\,\mathrm{MeV}$ for the individual E_{cm} steps as defined in Table 1 .The errors shown are statistical only . An additional systematic error of 15% has to be included in each measurement. These final results were obtained from the third set of cuts ("π^0-subtracted and pattern cut") since it gives the best signal to noise. Results for the other cuts are the same within errors. As a check ,a similar measurement was also performed with a energy cut of $E_\eta > 800\,\mathrm{MeV}$ resulting in the same qualitative behavior over the different E_{cm} steps.

R_η with $E_\eta > 700\,\mathrm{MeV}$			
Step	E_{cm}-range [GeV]	$<E_{cm}>$[GeV]	R_η
1	3.860-4.000	3.943	.36 ± .09
2	4.000-4.060	4.040	.49 ± .09
3	4.060-4.140	4.110	.38 ± .05
4	4.140-4.220	4.179	.49 ±.04
5	4.220-4.300	4.256	.54 ±.05
6	4.330	4.330	.42 ± .04
7	4.300-4.380	4.344	.49 ±.07
8	4.380-4.500	4.422	.43 ±.06

Table 3. R_η with $E_\eta > 700\,\mathrm{MeV}$ for different E_{cm} steps.

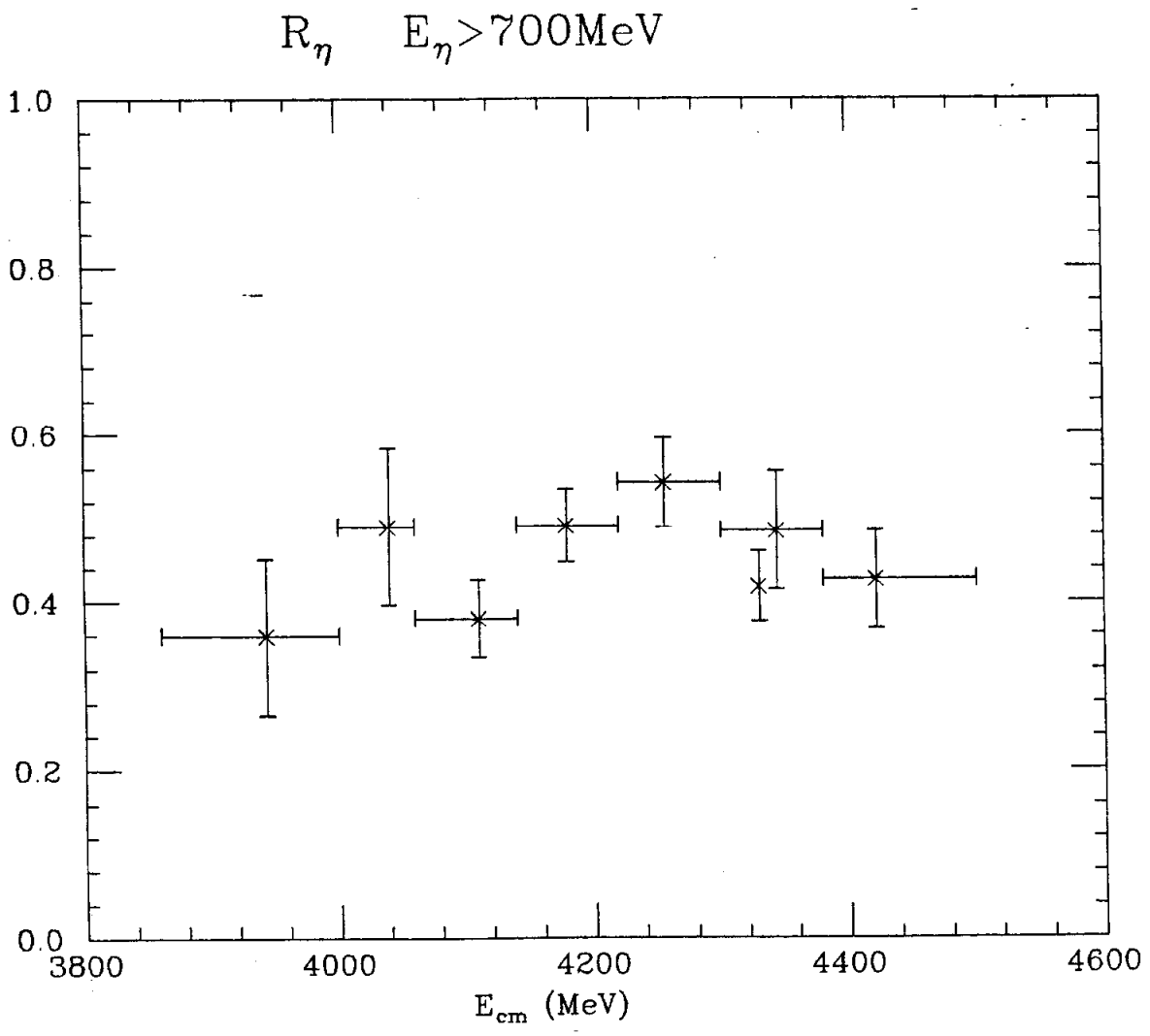

Figure 20. Inclusive η production R_η with $E_\eta > 700\,\mathrm{MeV}$.

Errors are statistical only. An additional systematic error of 15% has to be included.

The final result of R_η for inclusive η production with $E_\eta > 700\,\mathrm{MeV}$ shows no indication for a step in η production at $E_{cm} \approx 4.4\,\mathrm{GeV}$ as had been claimed by the DASP collaboration. This measurement ,therefore, cannot support their conclusion that there is a increased amount of F production resulting in an observed step in R_η. Figure 21 shows both measurements together. Since this measurement applied an η energy cut of $E_\eta > 700 MeV$, the results were scaled by a factor 1/.68 for better comparison. This factor was derived from a F Monte Carlo and corrects for the energy cut off .

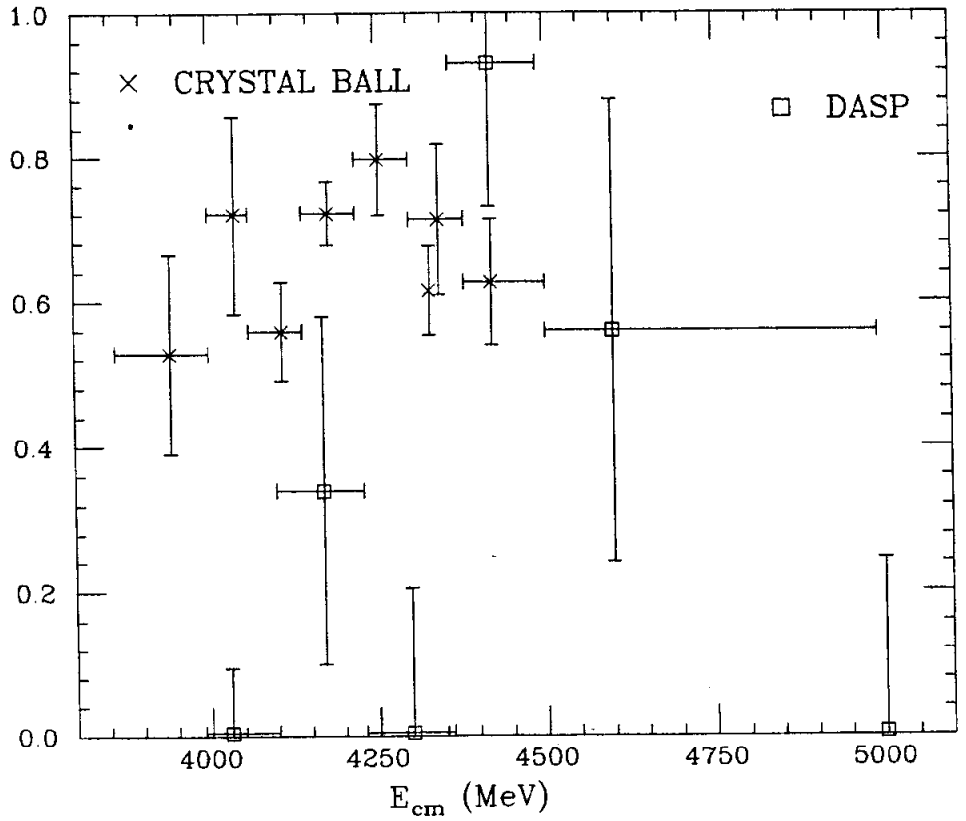

Figure 21. Comparison of R_η of DASP with this measurement

Chapter 5

INCLUSIVE γ SPECTRUM AT $E_{cm} = 4.33\,\mathrm{GeV}$

§5.1 INTRODUCTION

The F^* meson is expected to have only the radiative decay $F^* \rightarrow \gamma F$. If the center of mass energy is just above threshold for $F^*F^{(*)}$, it should therefore be possible to observe a monochromatic γ line in the inclusive γ spectrum. Since the cross section $\sigma_{F^*F^{(*)}}$ vanishes at threshold , one has to choose E_{cm} to be somewhat above the threshold $E_{F^*F^{(*)}}$ to have a finite cross section. This obviously results in a Doppler broadening of the monochromatic line that is proportional to β_{F^*} as long as $E_{cm} - E_{F^*F^{(*)}}$ is small compared to the threshold energy $E_{F^*F^{(*)}}$. Although the monochromatic line in the inclusive γ spectrum turns into a broad bump the line can still be detected , but with reduced statistical significance.

In this chapter a search for such a Doppler broadened transition line that would indicate F^* production will be done. The data set used for this search was taken in Fall 81 at a fixed center of mass energy $E_{cm} = 4.330\,\mathrm{GeV}$ and has good statistics ($\mathcal{L} = 1506nb^{-1}$) . This energy is 50 MeV above the F^*F^* threshold , corresponding to a F^* mass value of $m_{F^*} = 2.140\,\mathrm{GeV}$ as determined by the DASP experiment. Since this F^* mass has quite a large error of $\pm 60\,\mathrm{MeV}$ there is a certain range of m_{F^*} where the F^*F^* energy threshold is above the available center of mass energy , and only FF^* production is possible.

The center of mass energy of 4.33 GeV lies also in the "valley" of the hadronic cross section R which extends between 4.16 GeV and 4.46 GeV. Since the general behavior of R in the 4 GeV region can be explained by charm production one interprets these bumps in R as the $2D$ and the $4S$ state of the initial formed $c\bar{c}$ system. Most of charm production can be accounted for by the measured cross section for $D\bar{D}$, $D\bar{D}^*$ and $D^*\bar{D}^*$ production.[1] The production of D^* mesons complicates the structure of the inclusive γ spectrum and makes if more difficult to look for a Doppler broadened γ line that would indicate F^* production. Fortunately ,the center of mass energy of 4.33 GeV lies at a minimum of charm production and, therefore, the complication due to D^* production is also minimal. Nevertheless a measurement of the slow π^0 production will be done that can be used to calculate D^* production . This allows one to construct a fit function for the specifically shaped contribution to the γ spectrum due to the decays $D^* \rightarrow \pi^0 D$ and $D^* \rightarrow \gamma D$.

§5.2 INCLUSIVE γ SPECTRUM

The inclusive γ spectrum at $E_{cm} = 4.33$ GeV was obtained by plotting the track energy for all neutral tracks in each event. Figure 22 shows the the energy distribution obtained by applying only a "minimal" cut to each neutral track. This cut requires that $|\cos\theta_\gamma| < 0.90$, with θ_γ being the angle to beam direction , and $E_\gamma > 20$ MeV . The γ spectrum is shown logarithmically in $\Delta E/E = 8\%$ bins . This bin width was chosen to match to the Doppler broadend structure that is searched for .

The spectrum shows a peak at a neutral track energy of $\approx$ 210 MeV . This minimum ionizing peak is due to the contamination of the neutral tracks with charged tracks that were not detected by the tracking chambers. In addition to this peak , there is also a very wide bump noticeable centered around $\approx$ 70 MeV and which is due to the photons from slow π^0's that come from $D^* \rightarrow \pi^0 D$.

[1] Mark II-collaboration, Phys. Rev. D26,2190(1982).

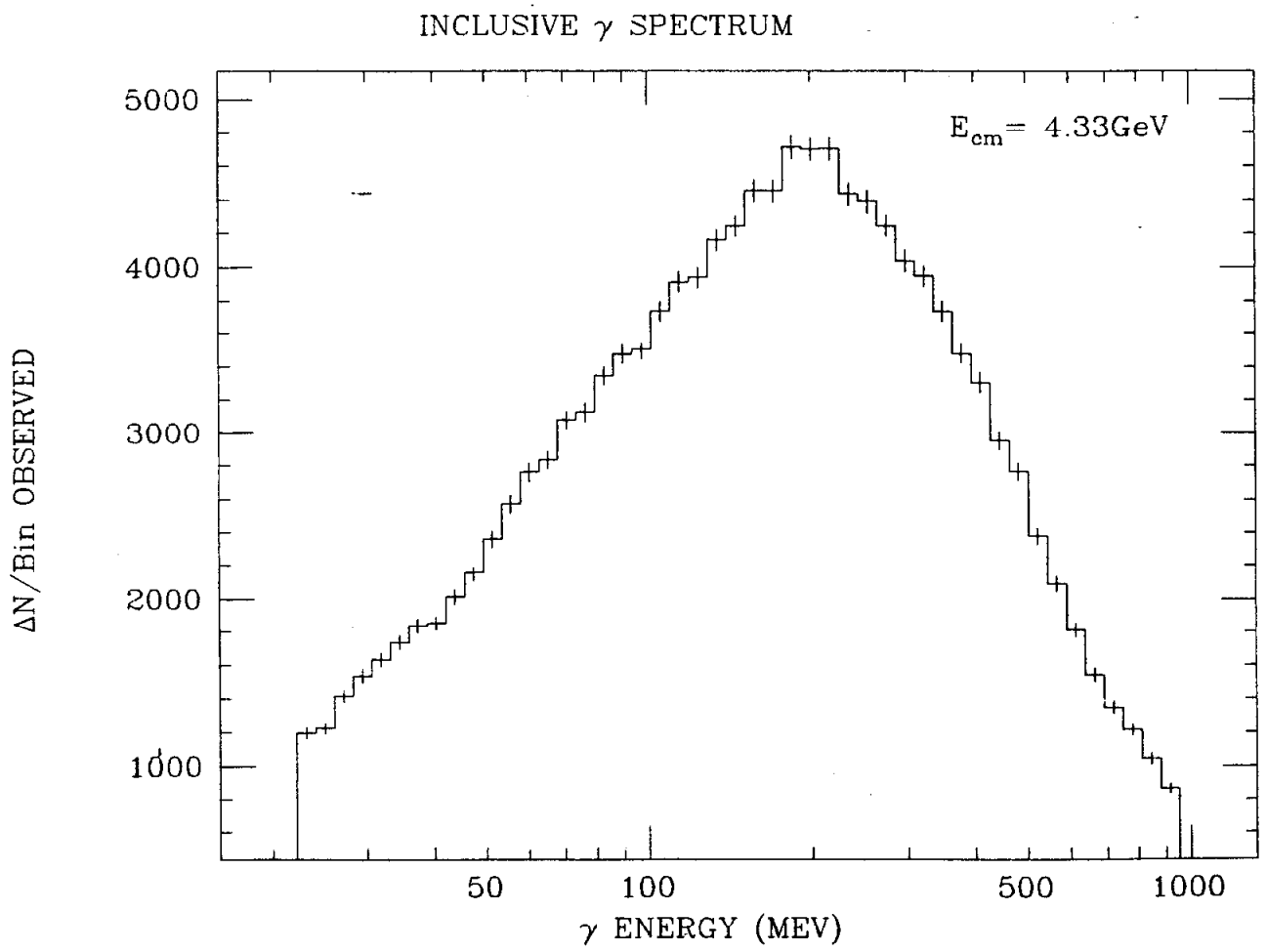

Figure 22. Inclusive γ spectrum at $E_{cm} = 4.33\,\text{GeV}$. For more details see text.

At this center of mass energy this "π^0 bump" is only barely visible since D^* production is low but it can very well seen at other center of mass energies , where D^* production is stronger. Otherwise ,there is no obvious structure visible in the photon energy spectrum that could be attributed to F^*F^* or FF^* production. Specifically ,in the region around $E_\gamma \approx 110\,\mathrm{MeV}$ the spectrum seems to be flat. This is the energy that would result from the masses $m_F = 2030(2000)\,\mathrm{MeV}$ and $m_{F^*} = 2140(2110)\,\mathrm{MeV}$, as determined by the DASP experiment.The second masses result from the possibilty that the DASP experiment actually observed F^*F^* events and not FF^* events.

Many other cuts had been applied to the inclusive γ spectrum in order to search for a possible enhancement of the γ line from $F^* \rightarrow \gamma F$, but no consistent peaks could be found. Some of these cuts were pure detector cuts as they were used in the inclusive η measurement , and the other cuts were physics motivated cuts.These cuts tried to enhance $F^{(*)}F^*$ events by cutting on specific properties that are expected for F decays. The physics cut , that were explored are the following:

a) multiplicity cut (charged and neutral).

b) rejecting an event if it contains a slow π^0 ($E_{\pi^0} < 170\,\mathrm{MeV}$). This should preferentially remove D^* events.

c) rejecting any event that does not have a $\gamma\gamma$ invariant mass combination within a certain mass window around the η mass . This cut was imposed since the F meson is expected to have a big branching fraction for the inclusive η decay.

In addition to examining the single γ spectrum , a search for signs of F^*F^* production was performed by plotting the energy of γ pairs that have almost the same energy. The maximal allowed energy difference was chosen so that most of the Doppler shifted transition γ pairs would be accepted. The γ spectrum obtained by this method showed a strong broad bump around 70 MeV which seemed to be connected with the slow π^0 from D^* decays but ,otherwise, no other striking structure was appearant. Although the γ pair spectrum has less statistics it appears that the level of sensitivity for detecting F^*F^* events is not better than from the single γ spectrum shown in

Figure 22 , since the ratio of the two efficiencies is roughly $\epsilon_\gamma/2 \approx .3$. Equal statistical significance of a small signal in both methods would require the γ pair spectrum to have $(\epsilon_\gamma/2)^2$ less statistics than the single γ spectrum in Figure 22 which is not the case. The method of plotting γ pairs with similar energy is actually only a simplified version of a method proposed by Cahn et al..[2] They noted that there are kinematical limits for the opening angle between the two transition γ's for a given set of observed γ energies and for a given set of F and F^* masses and center of mass energy. One can also turn the argument around and get restrictions for the possible F and F^* masses when a certain pair of γ's with energies $E_{\gamma_1}, E_{\gamma_2}$ and opening angle $\theta_{\gamma_1\gamma_2}$ is observed. Plotting the allowed range of F and F^* masses for each pair of γ's would then allow enhancement of F^*F^* events against background events with isotropic angular distribution. In additon ,they expect possible enhancement due to spin polarisation effects. This method was tried at various center of mass energies , and it was found that most of the background discrimination is due to the requirement that the two γ energies are similar.

Before the shape of the inclusive γ spectrum in Figure 22 can be fitted one has to understand the amount of charged particle contamination in the spectrum and also the amount of slow π^0's and transition γ's from D^* decays that could produce wide bumps around $\approx 70\,\mathrm{MeV}$ and $\approx 150\,\mathrm{MeV}$.

The charged particle contamination was determined by making use of the different behavior of the lateral shower pattern cut when applied to hadronic showers as compared to electromagnetic showers.If one plots the transmission efficiency as a function of the shower energy one sees ,in the case of hadronic showers ,a strong dip at the minimum ionizing energy. The same plot for electromagnetic showers shows only a smooth curve. In a real spectrum with charged track contamination one can still see a small dip around $\approx 210\,\mathrm{MeV}$. The magnitude of this dip is proportional to the amount of charged track contamination and can be measured. The exact procedure of this measurement is described in detail in Appendix F. The resulting charged

[2] R. N. Cahn, Y. Eylon, S. Nussinov, Phys. Rev.D 21,82 (1980).

particle fractions that are contained in the neutral track spectrum depend on the type of charged tracking chambers and also what kind of charged particle tracking code used. The data that were taken with the spark chambers show more charged "punch through" in general than the data taken with the tube chambers in Fall 81. For the Fall 81 data , which are of interest here, the fraction of charged hadronic tracks in the neutral spectrum is $5.2\% \pm 1.4\%$. This fraction agrees within errors with the fraction that is obtained by fitting the inclusive γ spectrum in Figure 22 with the shape of the charged particle spectrum and a background function that is a linear superposition of Legendre polynomials. The charged particle spectrum shape was obtained by using IR-tracks .

§5.3 D^* PRODUCTION AT $E_{cm} = 4.33\,\mathrm{GeV}$

The production of D mesons in the 4 GeV region seems to account for most of the expected charm cross section .[3] At lower center of mass energies this occurs mostly via quasi-two-body production like $D\bar{D}$,$D^*\bar{D}$, $D^*\bar{D}^*$ and probably also $D^{**}\bar{D}^{(*)}$, with D^{**} being the P-states. At higher energies also additional pions are being produced. For the inclusive γ analysis one needs to know the total amount of D^* production at $E_{cm} = 4.33\,\mathrm{GeV}$, but the measurement of D^* production itself is also of considerable interest. Definite predictions exist for the different cross sections from the charged coupled channel model of Eichten et. al.[4] Although the Mark II-collaboration has measured the cross sections for $D^{(*)}\bar{D}^{(*)}$ production in the 4 GeV region ,they were only able to calculate averages over wide center of mass energy bins .

The basic idea of measuring the D^* production cross section with the Crystal Ball experiment is to detect the slow π^0's emerging as a result from the decay $D^* \rightarrow \pi^0 D$. This does not allow one to distinguish between D^{+*} and D^{0*} production, and one must therefore assume equal cross sections due to isospin invariance. At $E_{cm} = 4.33\,\mathrm{GeV}$,it is also not possible to separate $D^*\bar{D}$ from $D^*\bar{D}^*$ production because the Doppler broadenings do not differ very much. The Doppler shifted

[3] MARK II-collaboration , Phys. Rev. D26, 1200(1980).

[4] E. Eichten, K. Gottfried, T. Kinoshita, K. Lane and T. Yan Phys. Rev. D17, 3090(1980).

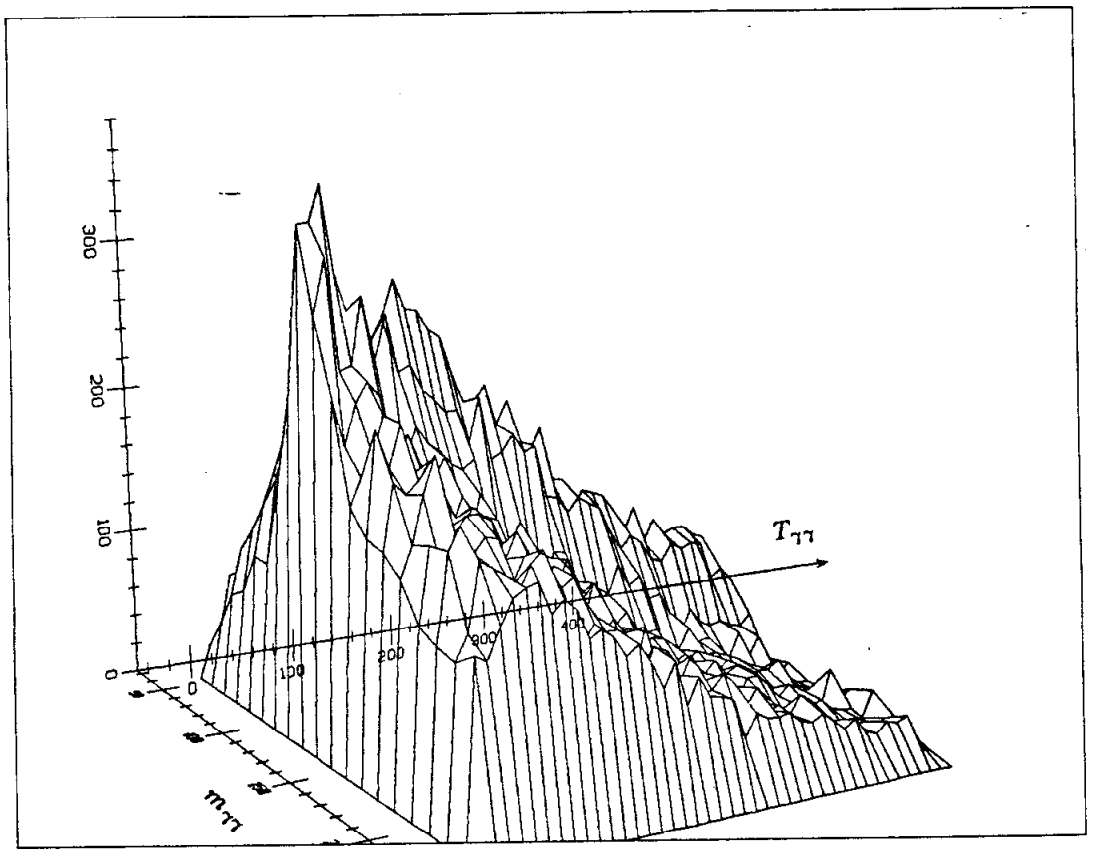

Figure 28. Kinetic energy $T_{\gamma\gamma}$ versus invariant mass $m_{\gamma\gamma}$ for all possible γ pairs from $E_{cm} = 4.33\,\mathrm{GeV}$ data

π^0 energies range from just above π^0 threshold to $\approx$ 176 MeV for the case of $D^*\overline{D}$ and to $\approx$ 168 MeV in the case of $D^*\overline{D}^*$ events. The maximal Doppler shift of the transition γ's from the decay $D^* \rightarrow \gamma D$ is bigger since the Doppler shift is proportional to $\gamma_D \cdot \beta_D \cdot \beta'$ .The quantity β' is the velocity of the emitted particle (π^0, γ) in the D^* restframe and is ≈ 0.29 for π^0's and equal to 1.0 for γ's.

In order to get the number of slow π^0's a plot of the π^0 energy spectrum is first needed that is properly subtracted from the combinatorical background underneath it. This was done by first plotting in a 2-dimensional histogram the invariant mass $m_{\gamma\gamma}$ versus the kinetic energy $T_{\gamma\gamma} = E_{\gamma\gamma} - m_{\gamma\gamma}$ for each γ pair combination that can be formed in a given event. Figure 23 shows the resulting 2-dimensional histogram for the Fall 81 data with $E_{cm} = 4.33\,\text{GeV}$. The cuts that were applied to the γ's were the "minimal" cuts as described in the previous section and the shower pattern cut *PATCUT*. This histogram was then sliced along the invariant mass axis with a step size of 5 MeV in kinetic energy. Each invariant mass plot was then fitted with a gaussian of fixed mean and width and 4 Chebyshev polynomials to extract the number of π^0's for that specfic kinetic energy. Finally the fit resulting from all the kinetic energy slices were plotted to form a "raw" π^0 energy spectrum . Figure 24 shows this energy spectrum which is not efficiency corrected yet. Instead of plotting the kinetic energy T_{π^0} the π^0 rest mass energy was added for display reasons . One immediately sees the peak at low π^0 energies that can be attributed to the decay $D^* \rightarrow \pi^0 D$. The corresponding plot that was generated from data taken at the ψ"(3772) is shown in Figure 25 . There is no such low energy peak visible in this spectrum. The ψ"(3772) data is a very good background point since it provides non charm events and $D\overline{D}$ events in similar proportion as one finds at $E_{cm} = 4.33\,\text{GeV}$.

The number of π^0's in the low energy peak from the 4.33 GeV data was determined by fitting a background curve of fixed shape to the π^0 energy spectrum , excluding the energy region from 135 MeV to 170 MeV. The shape of the background function was derived from a fit of 5 Chebyshev polynomials to the π^0 spectrum from the ψ"(3772) data.

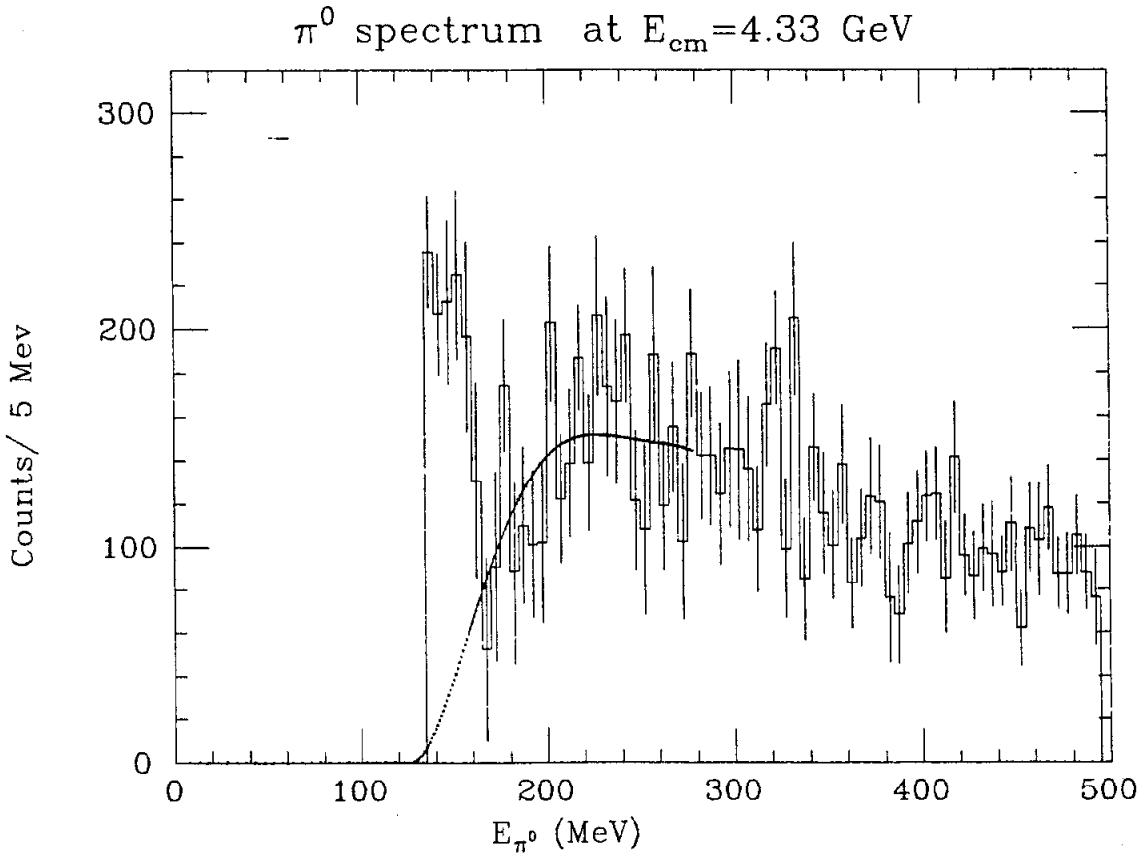

Figure 24. Observed π^0 energy spectrum at $E_{cm} = 4.33\,\text{GeV}$. Not efficiency corrected.

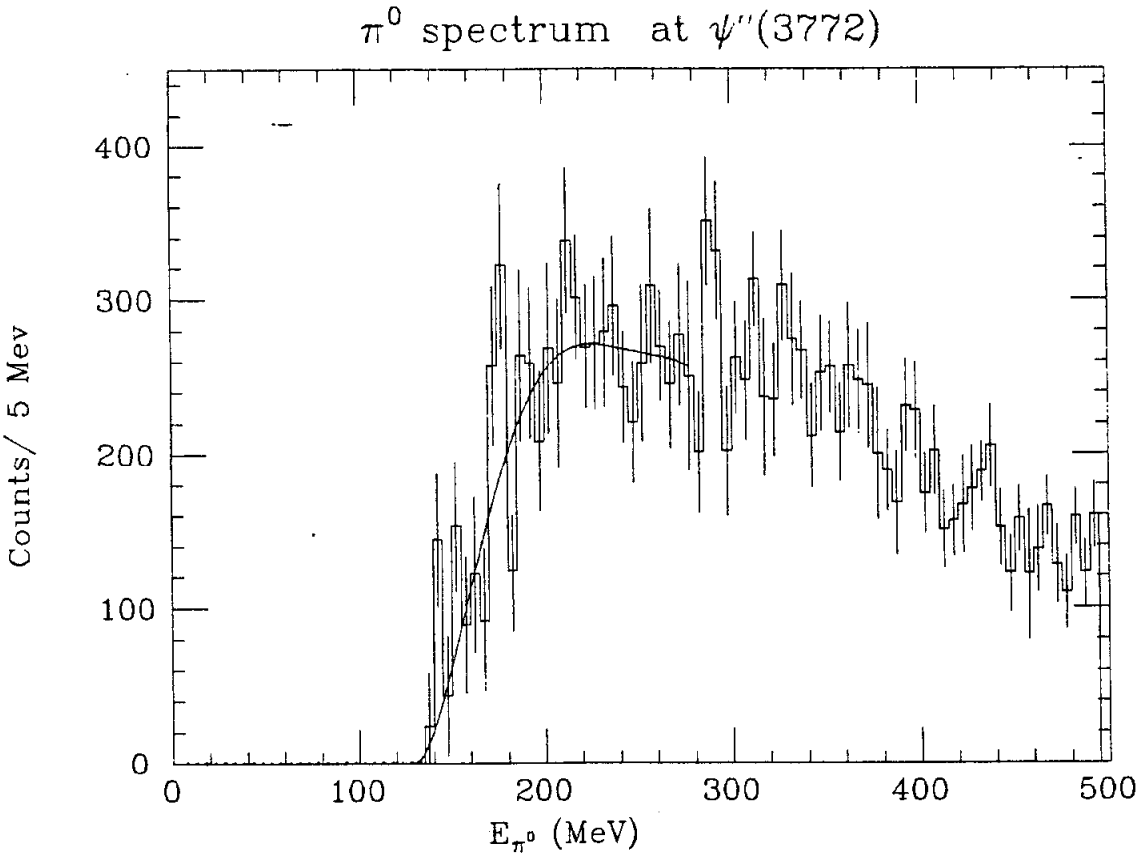

Figure 25. Observed π^0 energy spectrum at ψ"(3772). Not efficiency corrected.

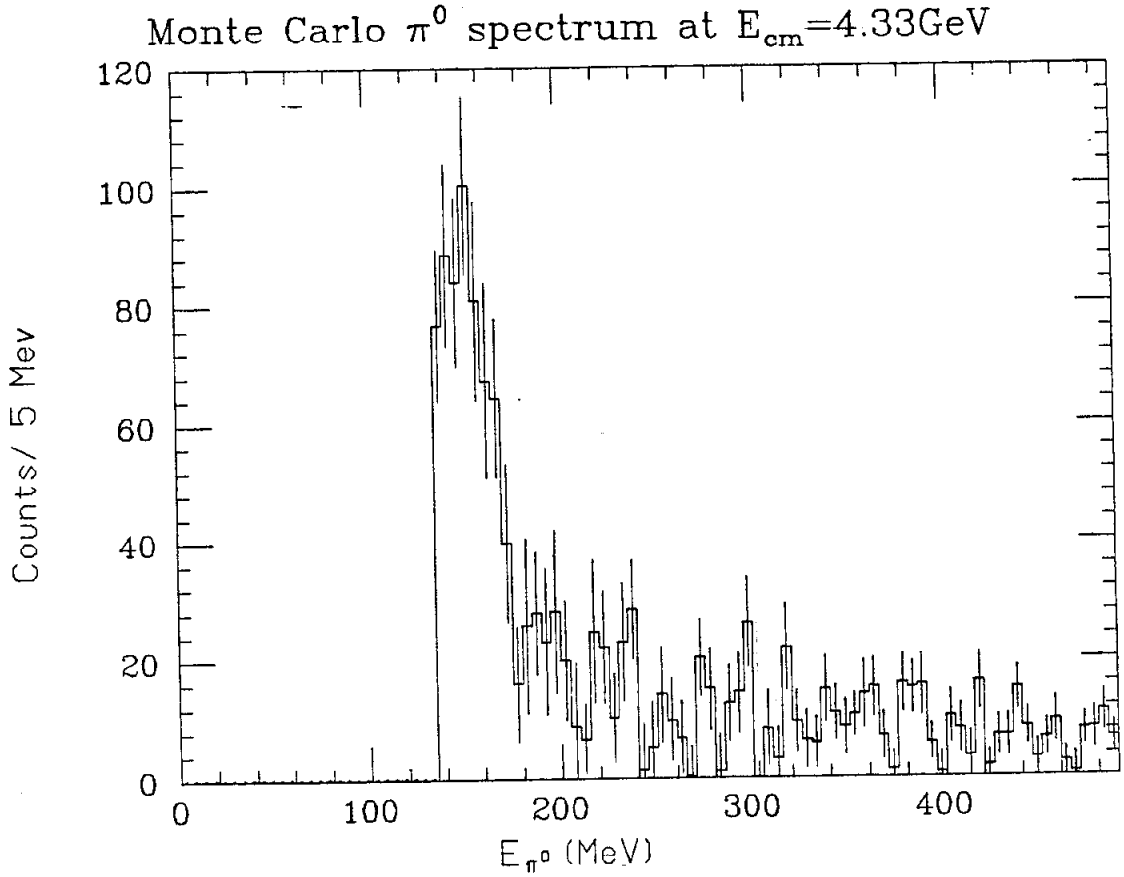

Figure 26. Observed π^0 energy spectrum from $D^*\overline{D}$ and $D^*\overline{D}^*$ Monte Carlo at $E_{cm} = 4.33\,\text{GeV}$

The number of low energy π^0's in the 4.33 GeV data was then calculated by adding up the number of entries above the background function within the energy range that is expected for the Doppler shifted π^0's. The reason this method was used is due to the fact that the observed π^0 box in Figure 24 is $\approx$ 10 MeV too narrow compared with the corresponding plot in Figure 26 obtained from Monte Carlo data . Doing a fit with a fit function that is too wide would not give very good results. The observed difference in width could be partially explained by the fact that the Monte Carlo data consist of $50\% D\overline{D}^*$ and $50\% D^*\overline{D}^*$ events, whereas at $E_{cm} = 4.33\,\text{GeV}$ fraction of $D^*\overline{D}^*$ events may be larger. Another possible explanation is the production of $D^{**}\overline{D}$ events at this center of mass energy. The MARK II experiment has possibly seen the D^{**} meson in the D recoil spectrum with a mass of $\approx$ 2450 MeV . The energy threshold for $D^{**}\overline{D}$ would then be just below the available center of mass energy. A third possibilty would be the production of additional π's that absorb some of the available collision energy , but at this center of mass energy the production of new resonances is probably more dominant.

The efficiency for detecting the slow π^0's has been determined with the help of Monte Carlo data . Half of the generated Monte Carlo data are $D\overline{D}^*$ events and half are $D^*\overline{D}^*$ events. Each channel has the same amount of charged events and neutral events. Although the coupled channel model of Eichten at. al.[5] predicts roughly the same cross section for $D\overline{D}^*$ as for $D^*\overline{D}^*$ production at $E_{cm} = 4.33\,\text{GeV}$ it is ,of course , not experimentally verified . Since the multiplicities of these two types of events are slightly different, one gets different efficiencies for the detection of the slow π^0's . Therefore , the final efficiency will have a systematic error due to this uncertainty in the correct event multiplicity. The decay of the D mesons into hadrons was done according to branching fractions given by the constant matrix element model of Quigg and Rosner[6] . In addition to the hadronic decay modes there are also semi-leptonic decay modes added to the decay routine in order to adjust the Monte Carlo D multiplicities to the experimental observed multilicities of real D's. The generated Monte Carlo events were then run through the detector simulation that

[5] E. Eichten, K. Gottfried, T. Kinoshita, K. Lane and T. Yan , Phys. Rev. D21, 203(1980).

[6] C. Quigg, J. Rosner, Phys. Rev. D17 (1978)p.239

also included a simulation of the tube chambers that were used as a central tracking chamber for the data at $E_{cm} = 4.33\,\mathrm{GeV}$. The simulation of the tube chambers used chamber efficiencies that had been calculated from real Bhabha events . The z-resolution of the tube chamber hits in the Monte Carlo was also adapted to the resolution observed in real hadronic data. More detail about the exact efficiencies and z-resolutions used are descibed in Appendix A . The detector Monte Carlo program also had a γ conversion routine added , whichs simulated the conversion of photons in the beam pipe and in the tube chamber material .The routine uses an energy dependent photon conversion probability. It assumes that the created e^+e^- pair has a very small opening angle and therefore appears as single track in the chamber. The resulting fraction of converted γ's lying within the solid angle of the central ball is 3.6%. Since the photons converting in the chambers create only hits in a few layers , it is possible for the tracking software to miss the new charged track . Using the tube chamber efficiencies that are mentioned above , it was found that only 2.5% of the γ's finally got lost due to photon conversion.

Figure 26 shows the π^0 energy spectrum that was obtained from the Monte Carlo data described above. The photon cuts that were used for this plot were the "minimal" cut ($|\cos\theta_\gamma| < .90$,$E_\gamma > 20\,\mathrm{MeV}$) and the shower pattern cut (PATCUT). The efficiency was then obtained by dividing the number of slow π^0's in the peak with the number of π^0's generated. The number of π^0's in the peak was calculated by adding the number of entries in the energy range of the $D\bar{D}^*$ Doppler box over a liner rising background. The resulting efficiencies for detecting a slow π^0 from $D^* \rightarrow \pi^0 D$ are : a). $\epsilon_{\pi^0} = 20.3\% \pm 1.6\% \pm 3.1\%$ for the case of the "minimal" cut and $PATCUT$. b). $\epsilon_{\pi^0} = 31.3\% \pm 1.9\% \pm 4.8\%$ for the "minimal" cut alone. The first error stems from the limited Monte Carlo statistics and the second error is systematic and contains the uncertainty due to the unknown ratio of $D\bar{D}^*$ to $D^*\bar{D}^*$ production at $E_{cm} = 4.33\,\mathrm{GeV}$ and also the uncertainty of the D multiplicity.

The number of slow π^0's in the π^0 energy spectrum at $E_{cm} = 4.33\,\mathrm{GeV}$ was determined as described earlier by using the background shape which was obtained from the ψ"(3772) data . For the π^0 spectrum in Figure 24 ("minimal" cut and shower pattern cut) this gave 931 ± 101. The

resulting cross section for the low energy π^0 peak is : $\sigma_{slow\pi^0} = 3.05nb \pm 0.41nb \pm 0.47nb$. The first error is statistical , the second error is systematic. The results obtained with the "minimal" cut alone agree well within errors. If one attributes the slow π^0 peak as only coming from the decays $D^* \rightarrow \pi^0 D$ and assumes that the cross section for D^{*+}production is the same as for D^{*0} production , it is possible to calculate the cross section for D^* production . By using the combined branching ratio of 0.415 ± 0.087 for $D^{*+} \rightarrow \pi^0 D^+$ and $D^{*0} \rightarrow \pi^0 D^0$, as given to date by the Particle Data Group, one obtains the following cross section for D^* production :

$$\sigma_{D^*} = 7.3nb \pm 1.1nb \pm 1.3nb$$

Again, the first error is the statistical and the second error is systematic which is basically due to the unknown ratio of $D\overline{D}^*$ to $D^*\overline{D}^*$ production .This cross section can also be expressed in units of the $\mu^+\mu^-$ point cross section for better comparison with the predicted values from the coupled channel model of Eichten et.al.. The above cross section becomes:

$$R_{D^*} = 1.57 \pm 0.21 \pm 0.25$$

This experimental value has to be compared with $R_{D^*} = 1.17$ as given by the Eichten model. One has to point out ,however , that there has been no radiative correction applied that would lower the measured value . The MARK II experiment had also previously measured the various $D^{(*)}\overline{D}^{(*)}$ cross sections in the 4 GeV region , but they did not do a measurement at $E_{cm} = 4.33\,\mathrm{GeV}$ that could be compared with the result from this experiment.

§5.4 FITS TO THE INCLUSIVE γ SPECTRUM

The inclusive γ spectrum in Figure 22 can now be fitted in order to obtain quantitative upper limits for $F^*\bar{F}^*$ and $F\bar{F}^*$ production at $E_{cm} = 4.33\,\mathrm{GeV}$. The shape of the spectrum was fitted with the sum of the following fit functions:

1). charged particle spectrum : this fit function was used to accommodate the charged track contamination in the spectrum , resulting in the "minimum" ionizing peak around 210 MeV. The function was obtained from the energy spectrum of charged IR-tracks which is shown in Figure 27a .

2). γ spectrum from $D^* \rightarrow (\pi^0, \gamma)D$: this fit function was used to fit the peculiar shape of the γ spectrum that stems from the production of D^* . The fit function was obtained by using a high statistics Monte Carlo program that also included the detector energy resolution.The ratio of $D\bar{D}^*$ to $D^*\bar{D}^*$ events was chosen according to the prediction of the Eichten-model at this E_{cm}. The value of this ratio is absolutely uncritical , since the shape of the final γ spectrum for the two different types of events is almost the same at this center of mass energy and the total contribution of this fit function to the inclusive γ spectrum is quite small. Figure 27b shows the fit function which was used . The magnitude of this fit function was fixed , using the the cross section for D^* production as determined in the previous section.

3). $F^*\bar{F}^*$ and $F\bar{F}^*$ - fit function: this fit function was generated similarly to the previous one with a high statistics Monte Carlo program . Figure 27 shows the resulting Doppler broadened transition γ line from $F^*\bar{F}^*$ events (Figure 27a + 27c) and from $F\bar{F}^*$ events (Figure 27b + 27d) for each of the two limiting F^* masses that are covered by this measurement . The F mass was fixed to a value of 2030 MeV.

4). Legendre polynomials were used as smooth background shape for the γ spectrum.

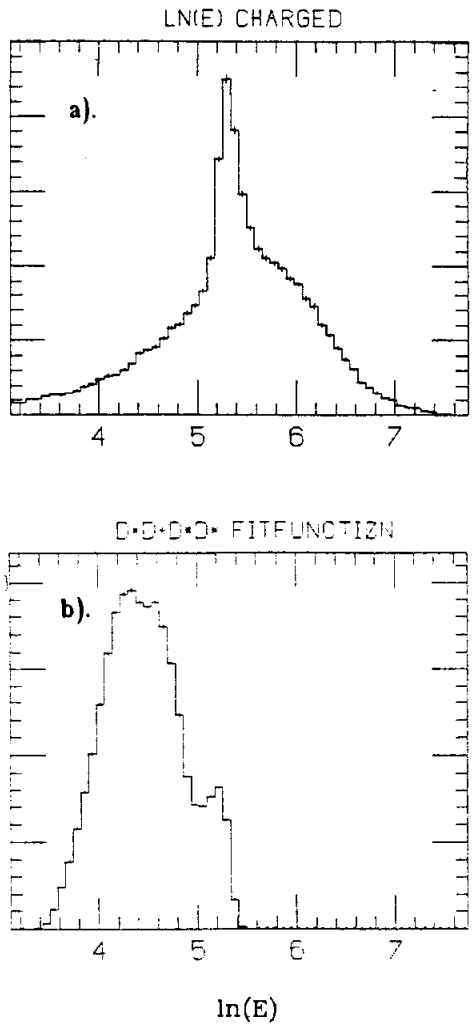

Figure 27. Fit functions used for inclusive γ spectrum.

a). charged particle spectrum. b). γ spectrum from $D^* \rightarrow (\pi^0, \gamma)D$.

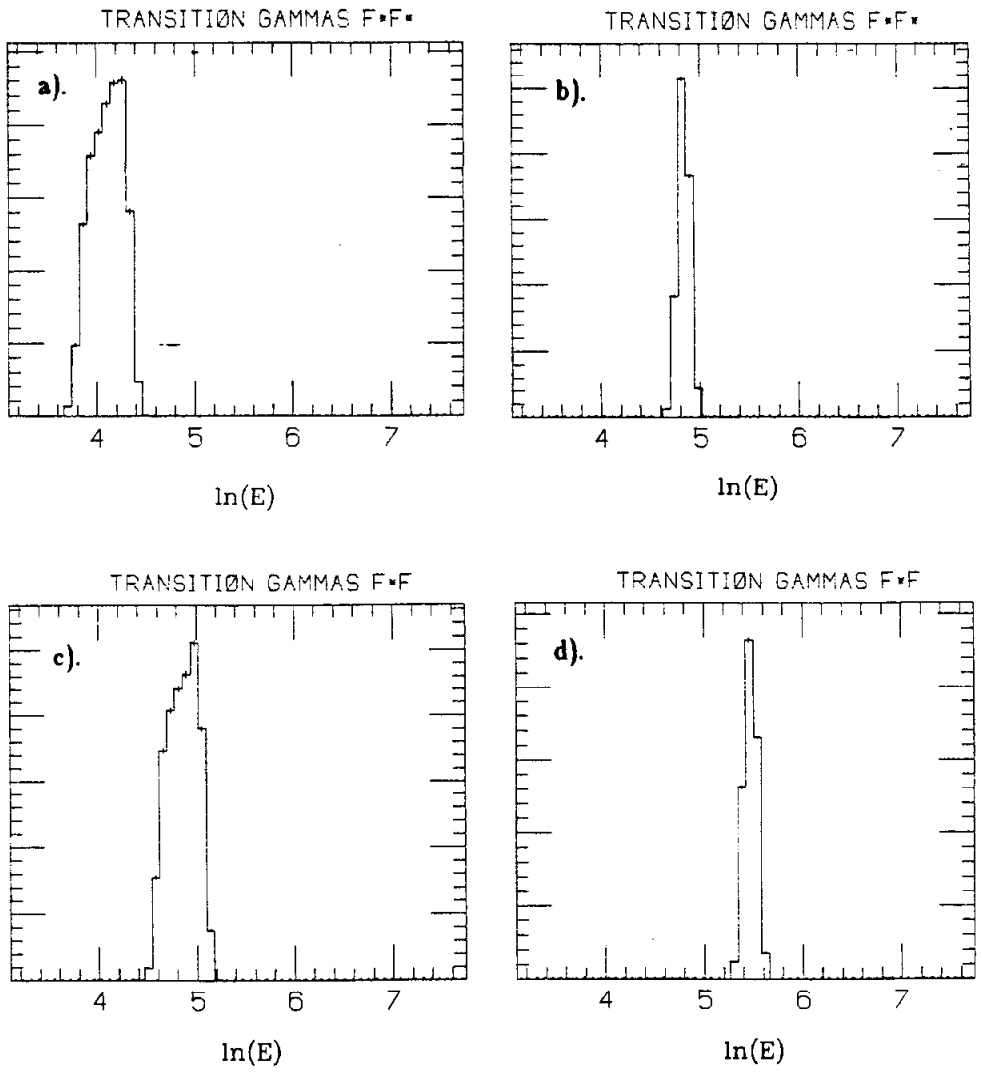

Figure 28. Fit functions of Doppler broadened γ line from $F^* \to \gamma F$. The four plots show the minimal and maximal F^* masses which are covered by this measurement. The F mass is fixed at 2030 MeV. a). F^*F^* with $m_{F^*} = 2090\,\mathrm{MeV}$. b). F^*F^* with $m_{F^*} = 2160\,\mathrm{MeV}$. c). $F\bar{F}^*$ with $m_{F^*} = 2160\,\mathrm{MeV}$. d). $F\bar{F}^*$ with $m_{F^*} = 2290\,\mathrm{MeV}$.

The whole fit function was then fit to the inclusive γ spectrum in Figure 22 by minimizing the χ^2 ,which was done with the help of a standard minimization routine.[7] In a first series of fits the fit function from the charged particle spectrum was left free in order to obtain the amount of charged particle contamination in the γ spectrum. From these fits a contamination of 5.7% was measured which agrees quite well with the value of $5.2\% \pm 1.4\%$ that was obtained with the method described in Appendix F. The fit function of the charged particle spectrum was then given a fixed value for all the following fits , using the value of 5.2% for the amount of charged track contamination. The fit function from the D^* decay was also fixed in magnitude , using the D^* production cross section that was determined in the previous section. The only functions that were left variable were the $F\overline{F}^*$ and the $F^*\overline{F}^*$ function along with the coefficients for 3-5 Legendre polynomials for a smooth background shape. The fits were done over a γ energy range from 40 MeV to 250 MeV. One problem with such a wide fit range was that the backgound function had difficulties to bend over at the peak of the spectrum and tended to overshoot at the low energy side , giving the $F\overline{F}^*$ and $F^*\overline{F}^*$ fit function a small negative amplitude. The fits were therefore redone with a smaller fit range in order to avoid this problem . This also allowed using fewer Legendre polynomials and keeping the background more rigid. The fits for the different F^* masses were all done with a fixed F mass of 2030 MeV . The F^* mass was varied from a minimum value of 2090 MeV to a maximum value of 2290 MeV in steps of 10 MeV . For the F^* mass range from 2090 MeV to 2160 MeV the two fit functions for $F\overline{F}^*$ and for $F^*\overline{F}^*$ production were both fitted simultaneously .Since the $F\overline{F}^*$ fit function is very wide in this mass range it is not possible to give any stringent limits for $F\overline{F}^*$ production . For F^* masses above the beam energy of 2165 MeV where only $F\overline{F}^*$ production is possible there is a certain mass range where the $F\overline{F}^*$ fit lies exactly on top of the charged minimum ionizing peak. It was therefore decided not to do give any results for F^* masses ranging from 2190 MeV to 2250 MeV.

[7] F. James, M. Roos, MINUIT CERN/DD internal report 72/20

§5.5 EFFICIENCIES

The efficiency for detecting the transition γ's from the decay $F^* \rightarrow \gamma D$ was obtained by using Monte Carlo generated $F\bar{F}^*$ and $F^*\bar{F}^*$ events. The produced F^* mesons were given the decay $F^* \rightarrow \gamma F$ meson. The resulting F mesons were then decayed further by the program into $\eta + n \cdot (\pi)$,$\eta' + n \cdot (\pi)$,$K\bar{K} + n \cdot (\pi)$ according to the branching ratios given by the constant-matrix-element model of Quigg and Rosner which had also been used for the D decays. The F decay routine only generated hadronic decay modes , and there were no semil-leptonic decay modes added like in the case of the D decay routine. The total semi-leptonic branching ratio for F mesons is not known , but it could be quite small . This is indicated by the currently accepted F lifetime which is quite small compared to the D lifetimes. The introduction of semi-leptonic decay modes in the Monte Carlo decreases the event multiplicity which results in an increased efficiency for reconstructing the correct particle tracks. If there is a possible bias by not having included the semi-leptonic decays it is probably small and worsens the detection efficiency. This would simply increase the value of the upper limits and make them safer.

The detection efficiency for γ's at various γ energies was then calculated by dividing the number of of reconstructed γ's with the number of generated ones. The number of reconstructed tracks was determined by first requiring the generated γ momentum vectors to be within 3 resolution width in ϕ and θ with the reconstructed γ track that were found by the analysis program. For these track pairs the energy differences were then plotted and the resulting peak at zero fit with a gaussian and a linear background. The obtained photon detection efficiency ϵ_γ for the "minimal" cut increases from $54\% \pm 3\%$ to $62\% \pm 4\%$ for a photon energy range from 60 MeV to 280 MeV . The quoted errors are only due to limited Monte Carlo statistics. An additional systematic error of 5% is estimated.

§5.6 RESULTS AND CONCLUSIONS

The fits to the inclusive γ spectrum at $E_{cm} = 4.33\,\text{GeV}$ show no sign of a peak that could be interpreted as coming from $F^*\bar{F}^*$ or $F\bar{F}^*$ production and therefore confirm the visual impression that one gets from Figure 22 . This has been expressed in upper limits for the cross section of $F^*\bar{F}^*$ and $F\bar{F}^*$ production at $E_{cm} = 4.33\,\text{GeV}$. These upper limits have been calculated for a range of F^* masses with a fixed F mass of 2030 MeV. This is the value for the F mass that had been quoted by the DASP experiment . For the upper limits of $F^*\bar{F}^*$ production the F^* mass was varied between 2090 MeV and 2160 MeV. Below 2090 MeV the Doppler broadened transition γ line becomes so wide that no meaningful numbers can be obtained. For $F\bar{F}^*$ production this range extends from 2160 MeV to 2290 MeV, with a gap from 2220 MeV to 2260 MeV due to complications with the minimum ionizing peak at $\approx$ 210 MeV.

The upper limits for the $F^*\bar{F}^*$ or the $F\bar{F}^*$ cross section $\sigma_{F^*\bar{F}^{(*)}}$ were calculated according to :

$$\sigma_{F^*\bar{F}^{(*)}} = \frac{N_\gamma}{\mathcal{L} \cdot n_\gamma \cdot \epsilon_\gamma} \tag{5.1}$$

with n_γ being the number of transition γ's in the event . N_γ was taken as 1.65 times the error of the $F^*F^{(*)}$ fit amplitude $(95\%CL)$, that was calculated by the fit program. The systematic error from the detection efficiency ϵ_γ was added linearly into the final upper limits.

Table 4 shows the resulting upper limits for the $F^*\bar{F}^*$ production cross section at $E_{cm} =$ 4.33 GeV for the different F^* masses . Figure 29 shows the same limits along with the predictions for the $F^*\bar{F}^*$ cross section as given by the charged channel model of Eichten et. al. The corresponding upper limits for $F\bar{F}^*$ production at $E_{cm} = 4.33\,\text{GeV}$ are given in Table 5 and in Figure 8 .

Upper limits for $F^*\overline{F}^*$ production at $E_{cm} = 4.33\,\mathrm{GeV}$ (95%CL)		
F^*mass [MeV]	$\sigma_{F^*\overline{F}^*}$ [nb]	$R_{F^*\overline{F}^*}$
2090	0.82	0.18
2100	0.67	0.14
2110	0.58	0.13
2120	0.48	0.10
2130	0.42	0.09
2140	0.37	0.08
2150	0.34	0.07
2160	0.28	0.06

Table 4. Upper limits for $F^*\overline{F}^*$ production with $m_F = 2030\,\mathrm{MeV}$.

Upper limits for $F\overline{F}^*$ production at $E_{cm} = 4.33\,\mathrm{GeV}$ (95%CL)		
F^*mass [MeV]	$\sigma_{F\overline{F}^*}$ [nb]	$R_{F\overline{F}^*}$
2160	2.05	0.44
2170	2.14	0.46
2180	2.12	0.46
2190	2.10	0.45
2200	1.97	0.43
2210	1.73	0.37
2270	0.80	0.17
2280	0.71	0.15
2290	0.57	0.06

Table 5. Upper limits for $F\overline{F}^*$ production with $m_F = 2030\,\mathrm{MeV}$.

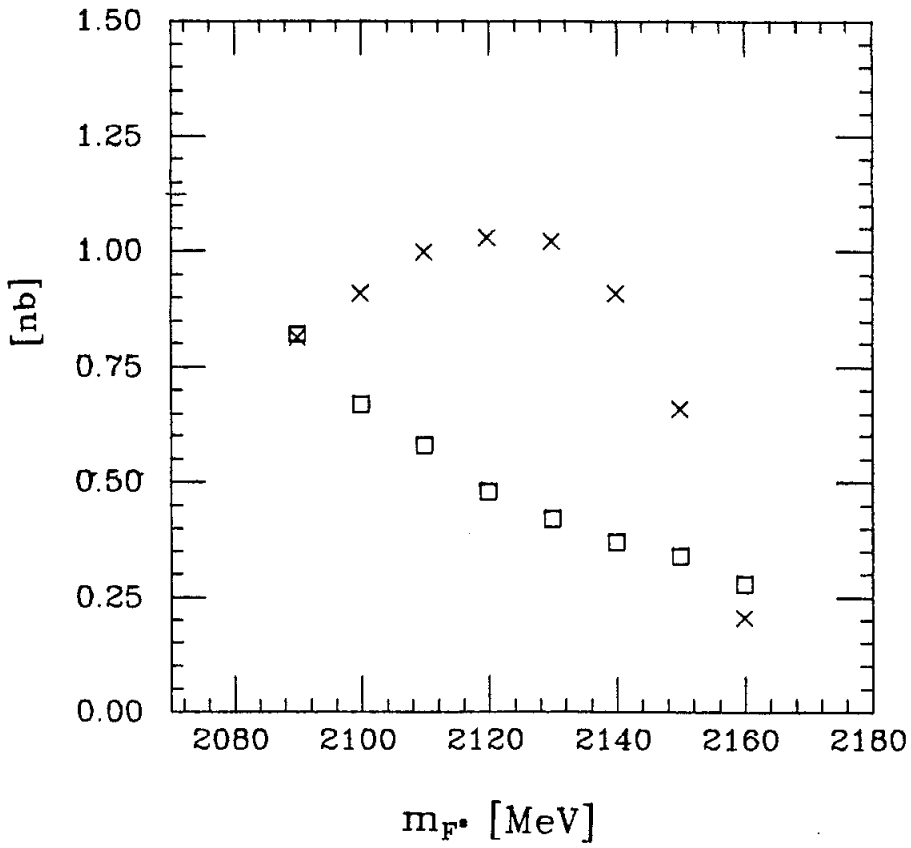

Figure 29. Upper limits for $F^*\overline{F}^*$ production at $E_{cm} = 4.33\,\text{GeV}$ as a function of F^* mass (squares).The F mass is fixed at 2030 MeV. The corresponding F^*F^* production cross sections given by the coupled channel model are also shown (crosses).

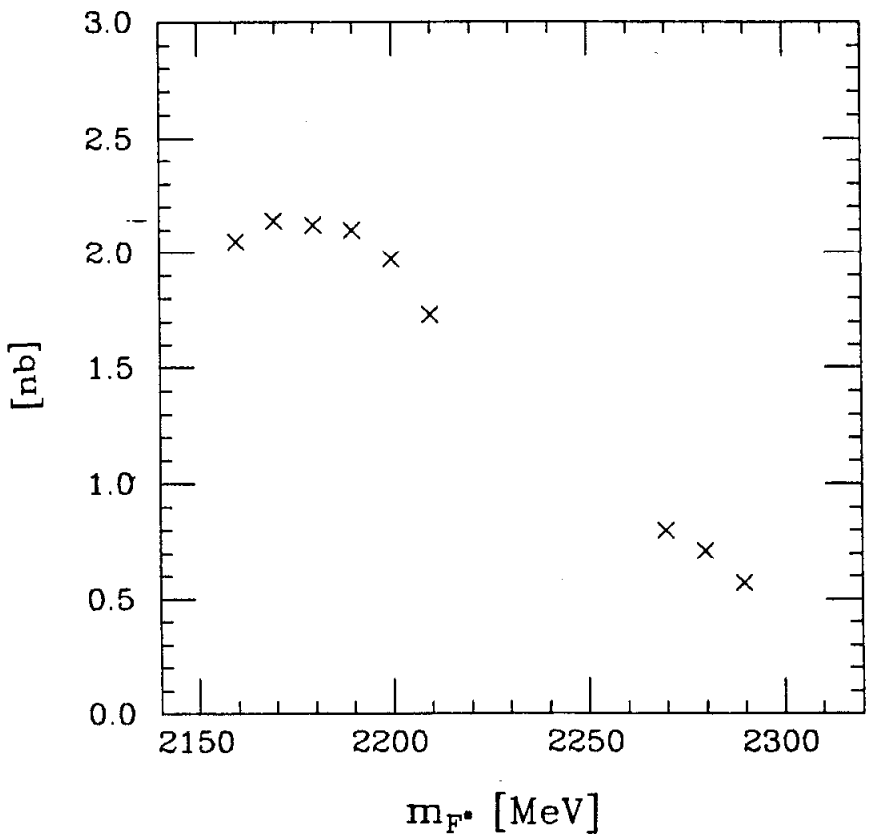

Figure 90. Upper limits for $F\overline{F}^*$ production at $E_{cm} = 4.33\,\mathrm{GeV}$ as a function of F^* mass (crosses).The F mass is fixed at 2030 MeV.

The upper limits for $F^*\overline{F}$ production are in disagreement with the predictions given by the coupled channel model for a range of F^* masses from 2100 MeV to 2150 MeV for a F mass of 2030 MeV. Taking the upper limit $BR(F^{\pm} \rightarrow \eta\pi^{\pm}) < 0.16$ as given by the results from the photoproduction experiments one can calculate a upper limit of $\sigma_{F^*\overline{F}^*} \cdot BR(F^{\pm} \rightarrow \eta\pi^{\pm}) < 0.059nb$. This is considerably lower than the $\sigma_{F^*\overline{F}} \cdot BR(F^{\pm} \rightarrow \eta\pi^{\pm}) = 0.41nb$ that had been claimed by the DASP experiment at $E_{cm} = 4.42$ GeV. Although this for $F\overline{F}^*$ production and at a higher energy , one would expect to observe a comparable cross section at $E_{cm} = 4.33$ GeV as is indicated by the coupled channel model.

Chapter 6

SEARCH FOR F PRODUCTION VIA $F^{\pm} \rightarrow \eta\pi^{\pm}$

§6.1 INTRODUCTION

In this chapter a search for $F\overline{F}, F\overline{F}^{*}, F^{*}\overline{F}^{*}$ production is done where one of the F has the decay $F^{\pm} \rightarrow \eta\pi^{\pm}$ and the other F goes into "anything". I shall refer to these as semi-exclusive decays. This search is motivated by results from the DASP experiment and the photoproduction experiments (WA4 and WA57) which all claimed to have observed the F meson via its $\eta\pi^{\pm}$ decay mode. Of all the Cabibbo favoured decay modes that are expected by the spectator model , this is the easiest detectable final state for the Crystal Ball . Since this experiment is a non magnetic detector it is not possible to measure the momentum of a charged particle , and the only way to determine this quantity is by using a constraint from 4 momentum conservation or from additional invariant mass constraints available in the event. The $F^{\pm} \rightarrow \eta\pi^{\pm}$ decay is the best reconstructable decay mode since it has only one charged particle and since the Crystal Ball detector is able to reconstruct η's with good efficiency and good energy resolution.

Using 4-momentum conservation and the various mass constraints , the following 3 types of fits were done:

a). $e^{+}e^{-} \rightarrow F\overline{F}$, with one F having the decay $F^{\pm} \rightarrow \eta\pi^{\pm}$. In this type of event one measures the the momenta of the 2 photons coming from the η decay and the direction

cosines of the charged track from the $\pi^{\pm}$. Using energy and momentum conservation and the equal mass constraint for the two F's ($\eta\pi^{\pm}$ invariant mass equal to recoil F mass) one can calculate the missing quantities . This corresponds to a 0-C situation with the additional η mass constraint. Looping through all possible track assignments in given event and plotting the $\eta\pi^{\pm}$-invariant mass one then can search in the final histogram for a peak at the F mass that would appear for $F\overline{F}$ production.

b). $e^+e^- \rightarrow F\overline{F}^* \rightarrow \gamma F + F$, with one F having the decay $F^{\pm} \rightarrow \eta\pi^{\pm}$. In this type of event one measures the momenta of the 2 photons from the η decay and from the transition photon and the direction cosines from the charged pion. As before one has 5 constraints that allow one to determine the missing quantities assuming that the charged track came from a $\pi^{\pm}$. If one fixes the F mass to a specific value one gets another constraint which leaves then a 1-C situation with an additional η mass constraint Doing a kinematic fit and cutting on the final chisquare one then can plot the $\gamma\eta\pi^{\pm}$ invariant mass and search for a peak that would incicate the F^* meson

c). $e^+e^- \rightarrow F^*\overline{F}^* \rightarrow \gamma F + \gamma F$, with $F^{\pm} \rightarrow \eta\pi^{\pm}$. In this type of event the momenta of the 2 transition γ's and the 2 γ's from the η decay and the direction cosines of the charged track are measured. Again, one has to assume the charged pion mass. In this type of event the two equal mass constraints (m_F and m_{F^*}) leads to a 1-C situation with an additional η mass constraint . This allows to fit the event with a kinematic fitting program and to cut on the combined chisquare . Plotting the fitted F mass and the F^* mass one then can search for a cluster that would indicate $F^*\overline{F}^*$ production.

§6.2 EFFICIENCY AND RESOLUTION

The efficiencies and invariant mass resolutions for the above mentioned semi-exclusive fits were obtained with Monte Carlo data. $F\overline{F}$,$F\overline{F}^*$ and $F^*\overline{F}^*$ events were generated and decayed

into hadronic final states according to the constant matrix element model that has been described earlier. These generated events were then run through the detector simulation program . Special attention had been paid to the central tracking chamber simulation program. The efficiencies used for the tracking chambers were the efficiencies that had been measured in real data . They are given in Appendix A and B . The z-resolution used in the proportional tube chamber simulation was also adjusted to the values measured in real hadronic data . The measurement is described in more details in Appendix A together with plots that show the observed distribution of z hits with its long non gaussian tails. In order to have a correct chamber simulation the Monte Carlo generated chamber hits were then smeared with two gaussians to obtain the same z-distribution as is observed in real data.

The Monte Carlo generated F events were then analysed , hadron selected and run through the neutral track separation program ($GAMFIND$) exactly the same way as real data . Efficiencies for the 3 different semi-exclusive fits were obtained by running the Monte Carlo events through the analysis and kinematic fitting program. The observed F and F^* mass peaks in the invariant mass plots were fitted with a gaussian and a low order polynomial background function to obtain the efficiencies and mass resolutions of the peaks. For the different types of fits described above it was found that the invariant mass resolution depends on the kinetic energy ΔT of the initially formed F or F^*. In order to obtain the mass resolution as a function of ΔT Monte Carlo events were generated for $F\overline{F}$, $F\overline{F}^*$ and $F^*\overline{F}^*$ production in ΔE_{cm} steps of 50 MeV. More details about the efficiencies and mass resolutions for each of the three different semi-exclcusive fits are given below.

§6.3 FITS TO $F\overline{F}$ PRODUCTION

In this section I will descibe in more detail the search for the F meson via the process $e^+e^- \rightarrow F\overline{F} \rightarrow \eta\pi^\pm + X$, where X stands for all the possible decay modes that are allowed for the second F . This process has just enough constraints to calculate all the unmeasured quantities (the only thing that really gets fit is the η 4-momentum) and to calculate the $\eta\pi^\pm$ invariant mass. The calculation of the F invariant mass is trivial . The equal mass constraint gives the charged pion energy $E_{\pi^\pm} = E_{beam} - E_\eta$ which then allows to calculate the pion momentum p_π, assuming it is a $\pi^\pm$. The square of the F mass becomes then $m_F^2 = E_{beam}^2 - (\vec{p_\eta} + \vec{p_\pi})^2$.

Several cuts were applied to the data before the invariant mass plots were calculated:

1). "muliplicity cut". Only events were accepted with less than 15 tracks. The number of neutral tracks had to be between 2 and 13 and the number of charged tracks was required to be between 1 and 8.

2). "minimal cut" as has been described before.

3). "charged-neutral overlap cut". This cut requires that a neutral track has no charged track close by with $\cos(\theta_{chrg,\gamma}) < 0.92$. Figure 31 shows the distribution that is obtained by plotting the cosine of the charged-neutral opening angle for all possible pairs in a event. The position of the cut is also indicated.

4). "pattern cut" . This cut has already been descibed before. Details are given in Appendix D.

5). π^0-subtraction and η selection. A simultaneous π^0 and η reconstructon was done using the global reconstruction routine that has been already described in Chapter 4 . The difference is that now the routine tries to reconstruct π^0's and η's simultaneously without using a γ twice. All pairs of γ's were required to fit either the π^0 or the η mass hypothesis with $\chi_i^2 < 3$. The configuration of such pairs that gave the best overall χ^2 was then searched with the requirement of having a confidence level

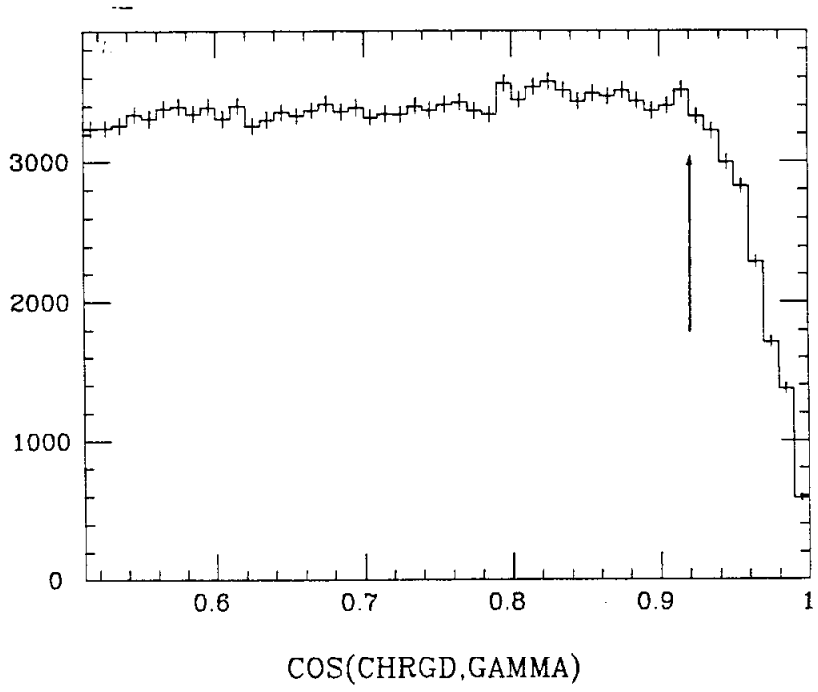

Figure 31. Plot of $\cos(\theta_{\gamma,charged})$ for all all pairs of charged and neutral tracks .

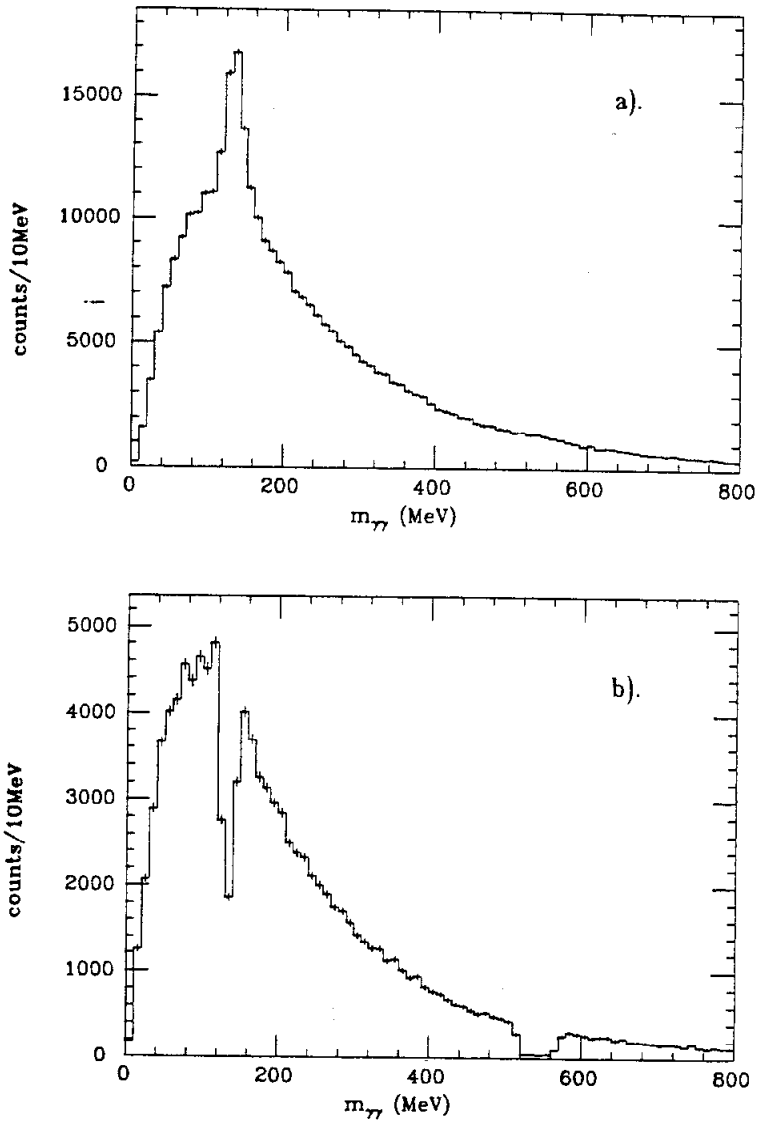

Figure 32. Invariant mass histogram for all $\gamma\gamma$ pairs before [a).] and after [b).] π^0 and η selection.

of more than .1. Figure 34a shows the histogram of all the $\gamma\gamma$ invariant masses before the π^0 and η subtraction. Figure 34b shows the same plot after all the reconstructed π^0's and η's were subtracted. A study with Monte Carlo generated F events shows that with the above mentioned χ^2 cut and confidence level cut 92% of the reconstructable η's are selected.

In order to obtain the invariant mass histogram all selected η's were paired with the charged tracks in a given event and the invariant mass calculated. The η 4-momentum vector used was the fitted 4-vector that was obtained from the global reconstruction routine. Applying this whole procedure to the Monte Carlo generated data allowed one to obtain the efficiencies and resolutions for the mass peaks. Figure 33 shows the resulting invariant mass plot for the Monte Carlo data at $E_{cm} = 4.08\,\text{GeV}, 4.13\,\text{GeV}$ and $4.18\,\text{GeV}$. The input mass for the F was 2030 MeV. The mass resolution for these three energy steps was found to be 6.0 MeV, 12.3 MeV, 17.6 MeV. The detection efficiency for the above described set of cuts was determined as 0.32 ± 0.07 . The error quoted here is dominated by the uncertainty due to the unknown F multiplicity.

The data in the center of mass energy range from 3.86 GeV to 4.50 GeV was divided into 8 different energy steps in the same way as it was done for the inclusive η measurement. For each of the energy steps an invariant mass histogram was accumulated as described above. Figures 34 - 41 shows the resulting plots for the 8 different energy steps. The fit curves superimposed were obtained from η sideband plots . For these η sideband plots the η mass was reset to 460 MeV and to 620 MeV. The combined invariant mass plot from the two sidebands was then fitted with 4 Chebyshev polynomials . The resulting coefficients for each energy step where then used together with a floating normalisation for the fits to the histograms in Figure 34 - 41.

No convincing peak can be seen in the invariant mass plots in Figure 34 - 41. Therefore , upper limits for $\sigma_{F\bar{F}} \cdot BR(F^{\pm} \rightarrow \eta\pi^{\pm})$ were calculated as a function of the m_F . The upper limits are $95\% CL$ and contain the 25% systematic error that is estimated for the efficiency due to the uncertainty in the F multiplicity.

The upper limits were calculated by fitting a gaussian of fixed position and width together with the η sideband background function to the spectra in Figure 34 - 41. The background function was taken 4.5σ of the gaussian on each side. The upper limit for the number of counts N_{UL} was then taken as 1.65 times the error for the gaussian amplitude plus the amplitude in case of a positive amplitude . The error contained in the efficiency was taken into account with help of a Monte Carlo program that was used to convolute the two distributions. The final upper limit for $\sigma_{F\overline{F}} \cdot BR(F^{\pm} \rightarrow \eta\pi^{\pm})$ was then calculated according to :

$$\sigma \cdot BR = \frac{N_{UL}}{\mathcal{L} \cdot 2 \cdot \epsilon_{F\overline{F}} \cdot BR(\eta \rightarrow \gamma\gamma)} \tag{6.1}$$

$\mathcal{L}$ is the appropriate luminosity that can contribute to the specific F mass under consideration . The factor 2 comes from the fact that both F's can decay into $\eta\pi^{\pm}$.

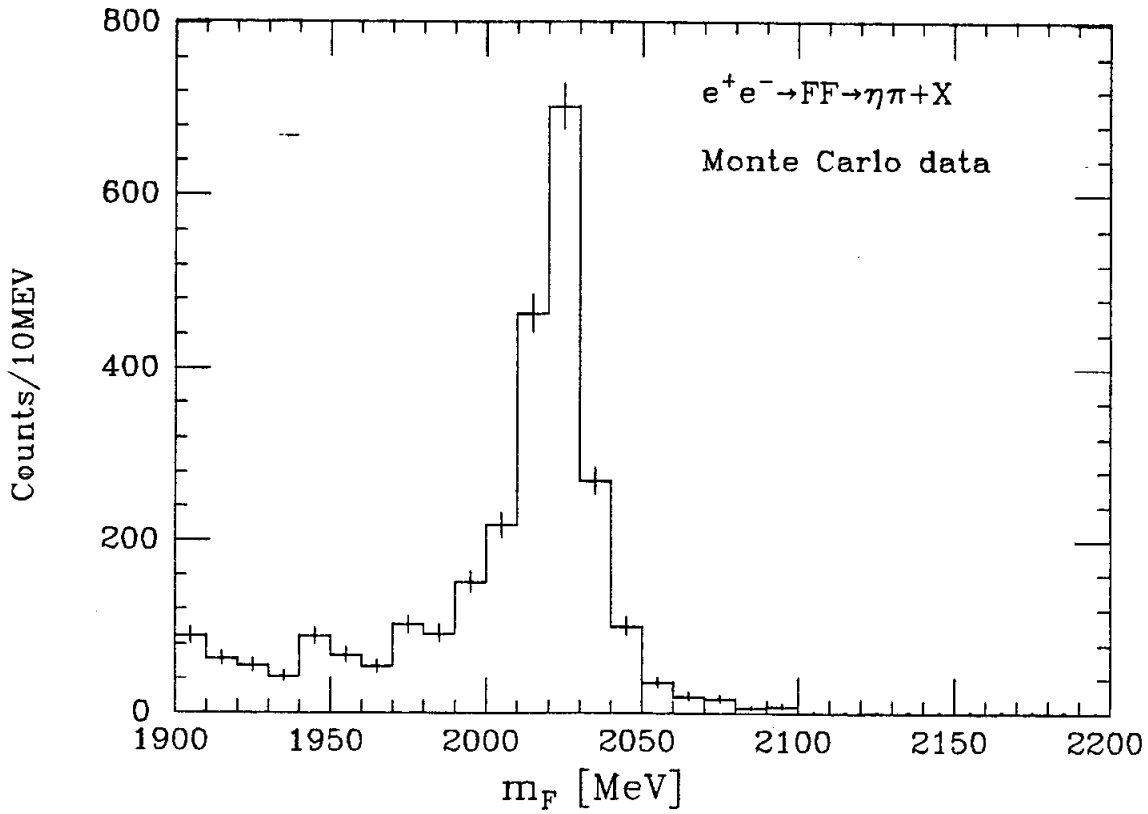

Figure 33. Invariant mass plot for Monte Carlo generated $F\overline{F}$ events, with one F having the decay $F^{\pm} \to \eta\pi^{\pm}$. $E_{cm} = 4.08\,\text{GeV}, 4.13\,\text{GeV}, 4.18\,\text{GeV}$

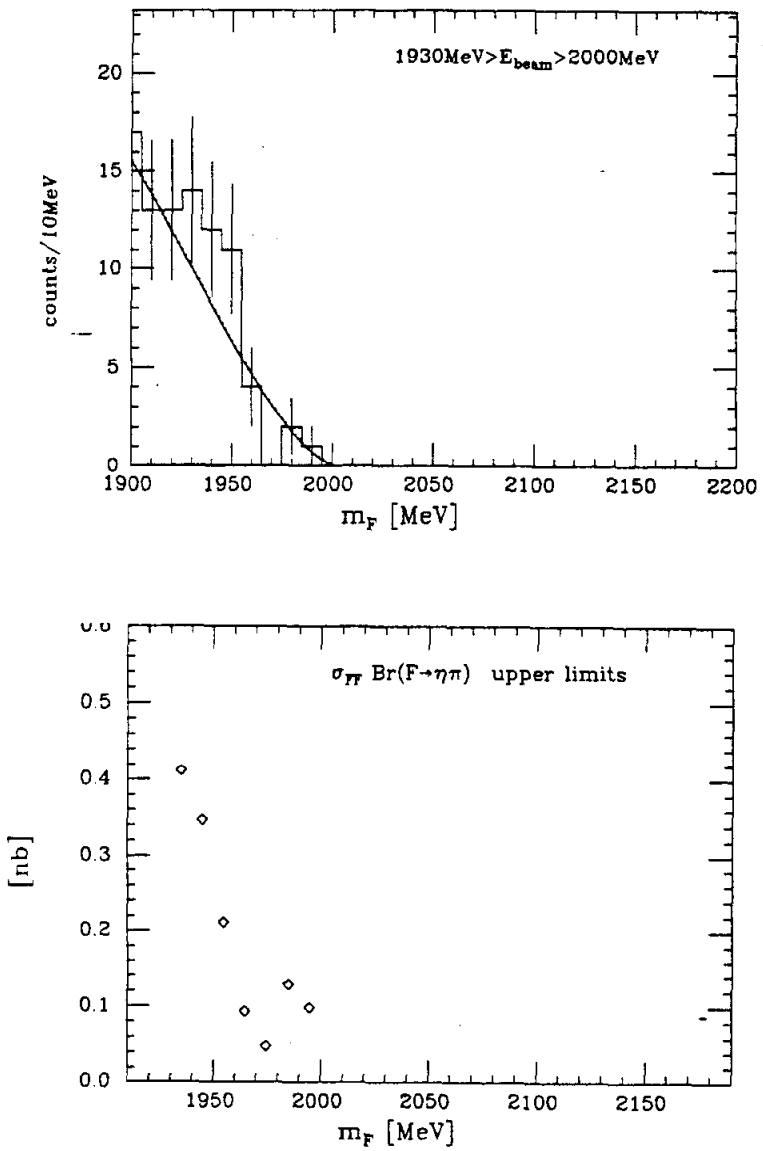

Figure 34. Invariant mass plot and Upper limits for $\sigma_{F\bar{F}} \cdot BR(F^{\pm} \to \eta\pi^{\pm})$ $(95\%CL)$

$E_{cm} = 3.86\,\text{GeV} - 4.00\,\text{GeV}$

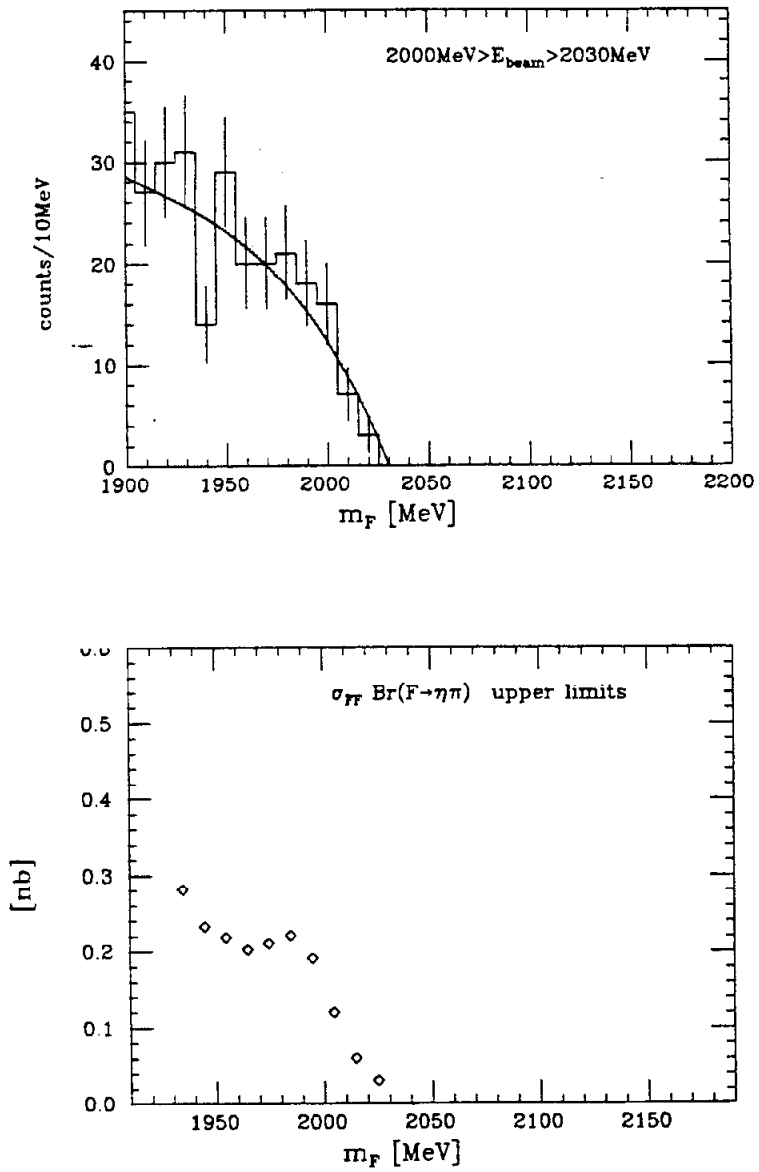

Figure 35. Invariant mass plot and Upper limits for $\sigma_{F\bar{F}} \cdot BR(F^{\pm} \to \eta\pi^{\pm})$ (95%CL)

$E_{cm} = 4.00\,\text{GeV} - 4.06\,\text{GeV}$

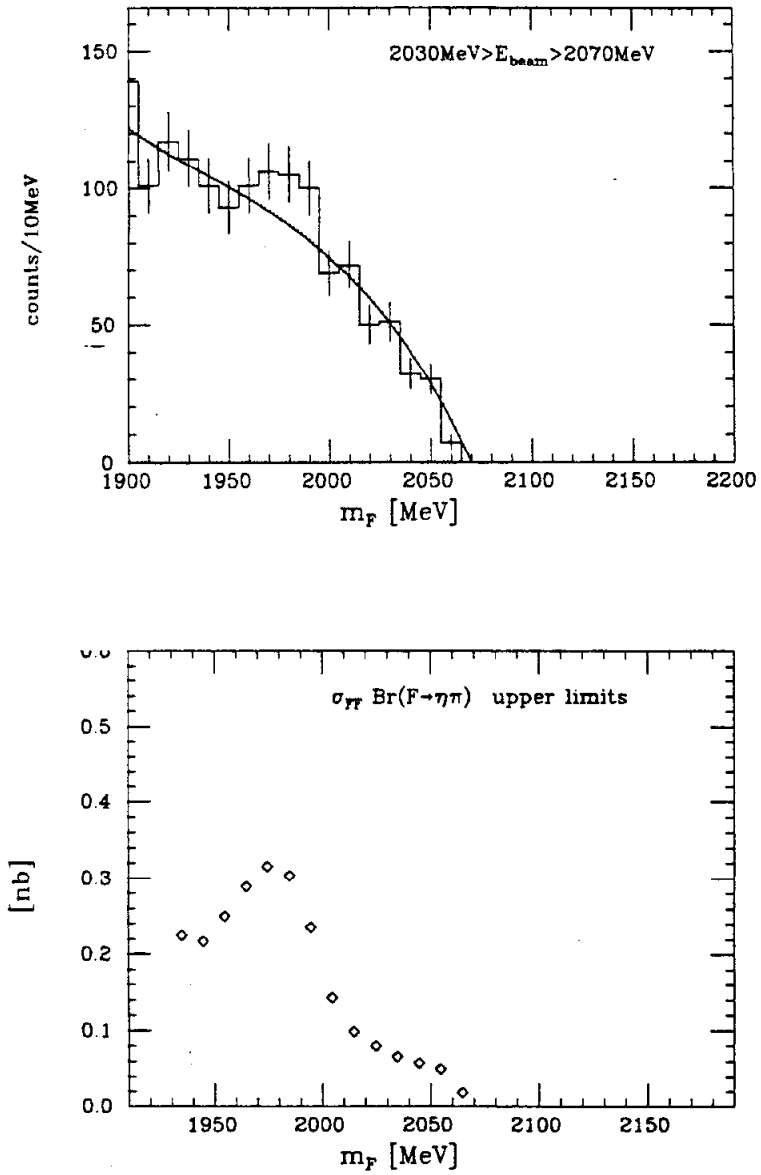

Figure 36. Invariant mass plot and Upper limits for $\sigma_{F\bar{F}} \cdot BR(F^{\pm} \to \eta\pi^{\pm})$ $(95\% CL)$

$E_{cm} = 4.06\,\text{GeV} - 4.14\,\text{GeV}$

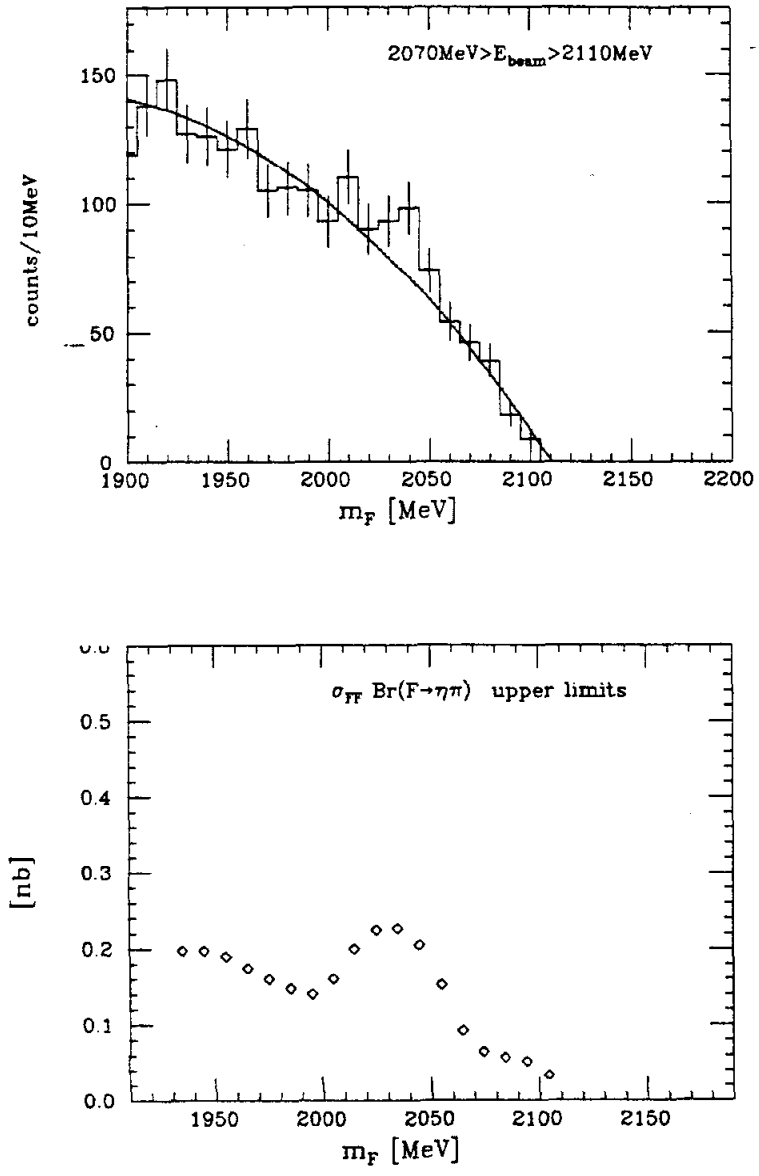

Figure 87. Invariant mass plot and Upper limits for $\sigma_{F\bar{F}} \cdot BR(F^{\pm} \to \eta\pi^{\pm})$ (95%CL)

$E_{cm} = 4.14\,\text{GeV} - 4.22\,\text{GeV}$

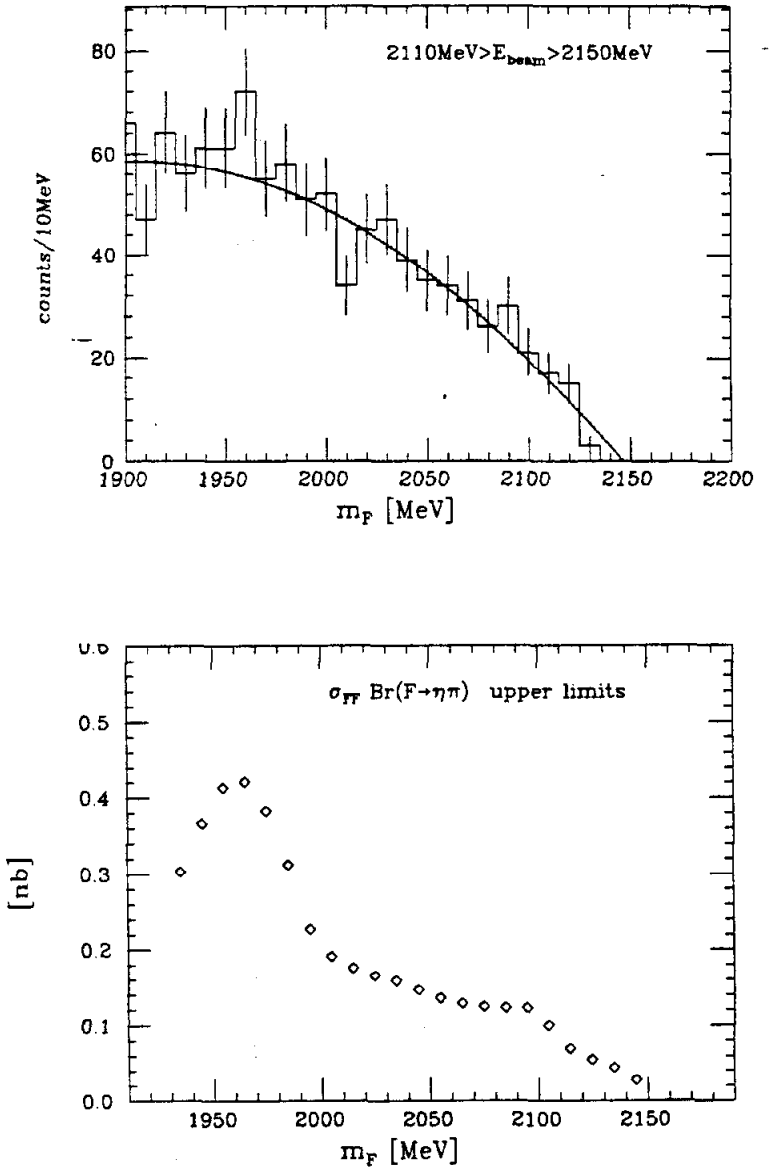

Figure 38. Invariant mass plot and Upper limits for $\sigma_{F\overline{F}} \cdot BR(F^{\pm} \to \eta\pi^{\pm})$ $(95\%CL)$

$E_{cm} = 4.22\,\text{GeV} - 4.30\,\text{GeV}$

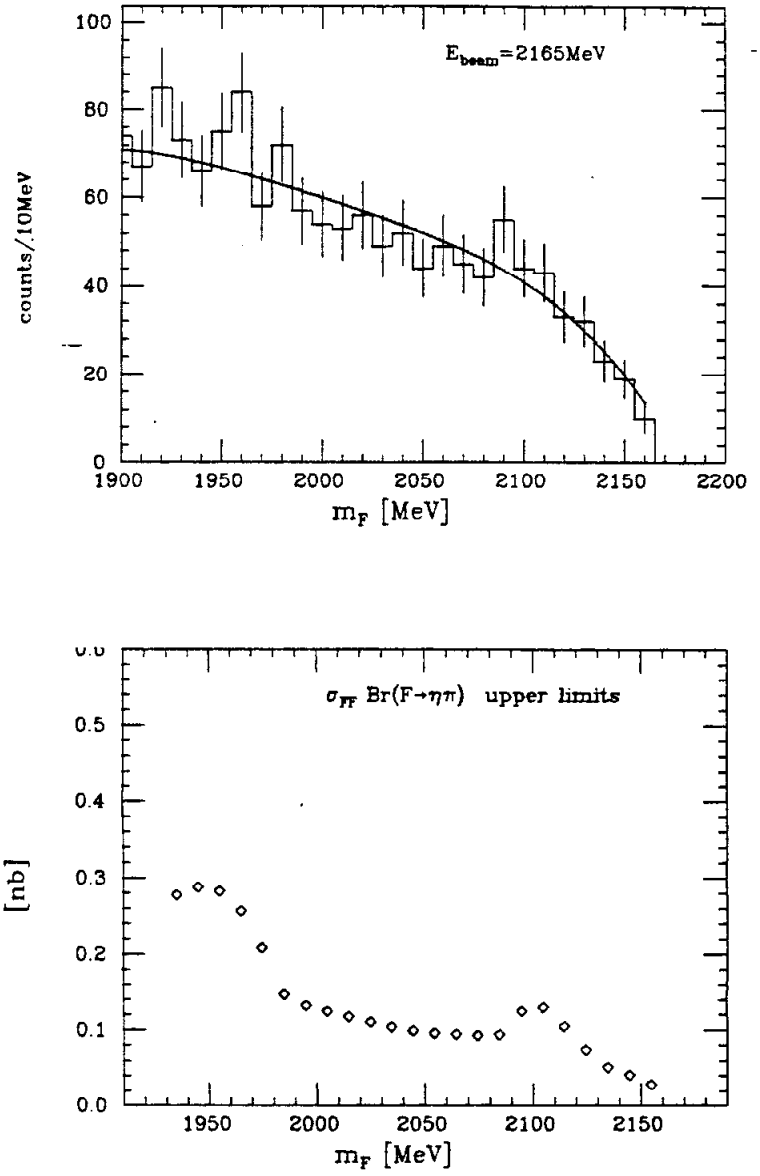

Figure 39. Invariant mass plot and Upper limits for $\sigma_{FF} \cdot BR(F^{\pm} \to \eta\pi^{\pm})$ $(95\%CL)$

$E_{cm} = 4.33\,\mathrm{GeV}$

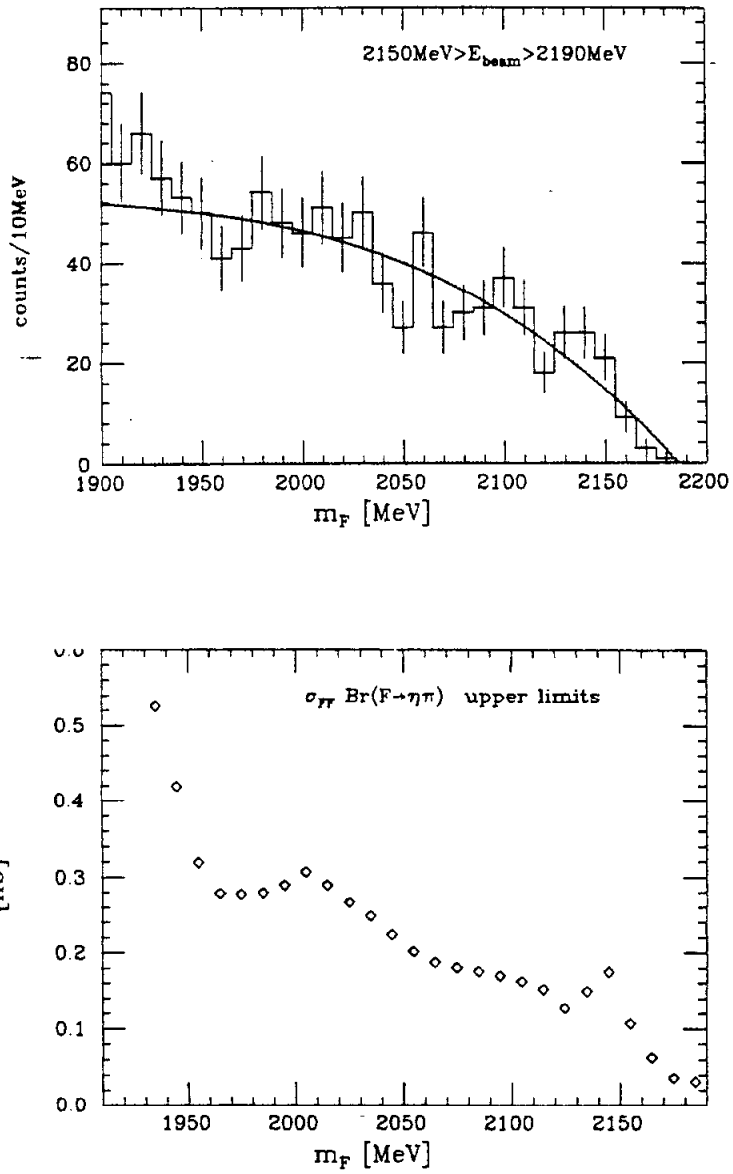

Figure 40. Invariant mass plot and Upper limits for $\sigma_{F\overline{F}} \cdot BR(F^{\pm} \to \eta\pi^{\pm})$ (95%CL)

$E_{cm} = 4.30\,\text{GeV} - 4.38\,\text{GeV}$

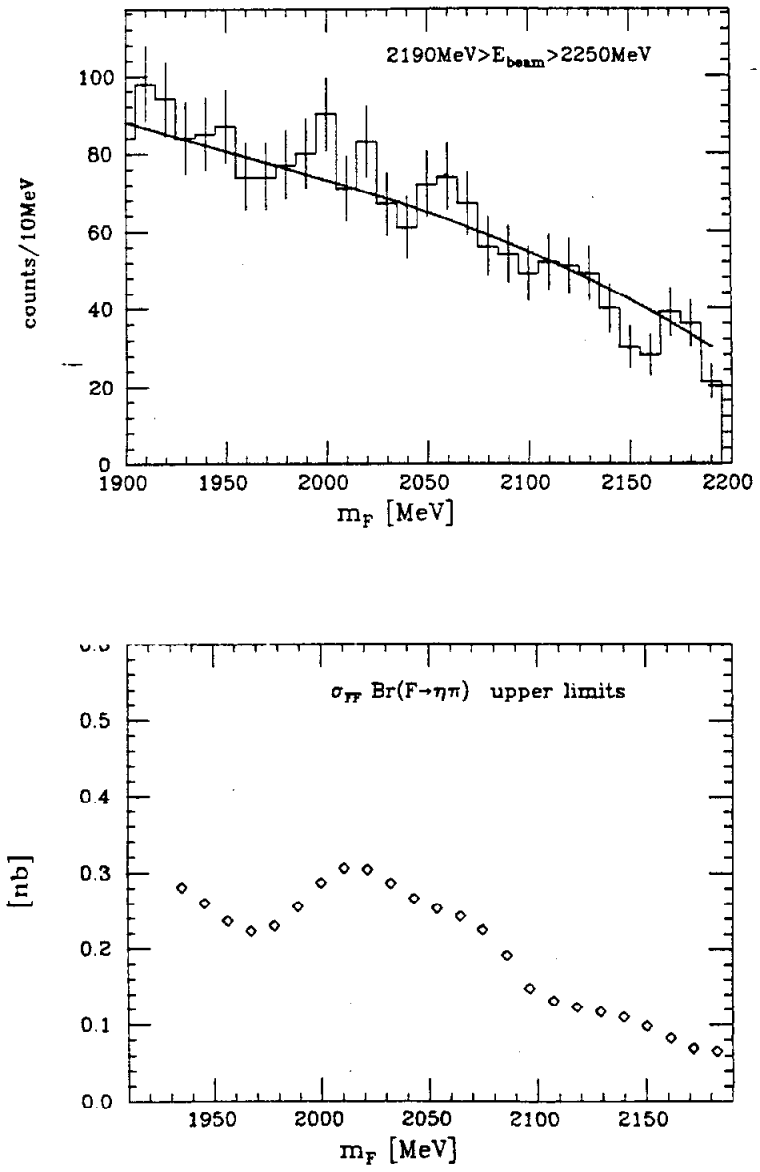

Figure 41. Invariant mass plot and Upper limits for $\sigma_{F\overline{F}} \cdot BR(F^{\pm} \to \eta\pi^{\pm})$ (95%CL)

$E_{cm} = 4.38\,\text{GeV} - 4.50\,\text{GeV}$

§6.4 FITS TO $F\bar{F}^*$ PRODUCTION

The search for the process $e^+e^- \rightarrow F\bar{F}^* \rightarrow \gamma F + F$ with one F decaying into $\eta\pi^\pm$ is described in this section . In this type of event one measures the directions and energies of the two γ's from the η decay and of transition γ coming from the decay $F^* \rightarrow \gamma F$. For the charged track one measures only the direction cosines and the energy has to be determined from a constraint assuming the charged pion mass. This leaves a 0-C situation plus an η mass constraint.

If the F mass of 2021 MeV $\pm$15 MeV that is quoted by the Particle Data Group as the world average is correct , it can be used as a additional constraint. This allows then a 1-C-fit plus a fit to the η mass and enables to search for the F^* meson . This fit was done with a kinematic fitting program callled *SQUAW* that has already previously been used for Crystal Ball data analysis. The program is a general fitting routine that also has the capabilty to fit to an equal mass constraint as is needed for the types of fits that will be done. A detailed description of the program is given elsewhere .[1]

Before the data could be fitted with *SQUAW* they had to pass various cuts and selection criteria . The same cuts were used as had been used for the $F\bar{F}$ fits , but with the exeption that the "pattern cut" was omitted and instead replaced by the requirement that a neutral track was not called a "split off" by the routine *SPLIT* which has been described earlier. The surviving events were then fit with *SQUAW*. The program loops through all possible track assignments and attempts a fit for each combination. In order to save computing time a subroutine was inserted that rejected all combinations that had no chance of beeing accepted in a fit. A confidence level cut of 0.1 was required for the fits to pass. If several track assignments passed this cut then only the fit with the best confidence level was used . For these fits the γF invariant mass was calculated using the fitted 4-momenta and plotted in a histogram. Since there is not enough information available to decide which F comes from the decay $F^* \rightarrow \gamma F$, one has to form both combinations

[1] F. Porter , Crystal Ball - note 20 (1982).

and plot their invariant masses. For center of mass energies just above the energy threshold $E_{F\bar{F}^*}$ for $F\bar{F}^*$ production the invariant mass peak formed by both combinations are both narrow. As one gets higher above $E_{F\bar{F}^*}$ the width of the wrong combination grows quickly whereas the width of the invariant mass peak formed by the correct combination stays narrow. Monte Carlo studies show that the invariant masses from wrong combinations form a box like structure that is about 80 MeV wide from edge to edge for events with E_{cm} being 50 MeV above threshold. For the correct combination one gets a resolution for the gaussian shaped mass peak of about 9 MeV . In order to get the proper detection efficiency and invariant mass resolutions for the F^* peak Monte Carlo events were generated and run through the whole analysis procedure. Figure 42 shows the invariant mass plot for the Monte Carlo data . The input masses that were used in the Monte Carlo for the F and the F^* were the DASP masses of 2030 MeV and 2140 MeV . The Monte Carlo data were generated for different center of mass energies in steps of 50 MeV . Fits were done to the observed peaks and it was found that the F^* mass resolutions and the efficinecies both were consistent with being constant for center of mass energies that are more than 50 MeV above threshold . For the invariant mass plots obtained from real data ,only F^* masses were considered that result in a $F\bar{F}^*$ energy threshold that is 50 MeV below E_{cm} . The width obtained for the F^* mass peak is 9.1 MeV and the detection efficiency is 0.125 ± 0.038 . The error in the detection efficiency is again dominated by the systematic error of 30% that was assumed due to the uncertain F multiplicity.

The data were divided into the same center of mass energy steps already used before. Since the F mass was fixed to a value of 2021 MeV only the steps with $E_{cm} > 4.14$ GeV were used . The steps 7 and 8 were also merged such that one is left with 4 center of mass energy steps . These data were fit with *SQUAW* and the resulting invariant mass plots are shown in Figure 42 - 45 . The shape of the fit curves that are shown have been obtained from η sideband plots in the same way as has been described in the previous section . The invariant mass plotts show no obvious peaks . Upper limits (95%*CL*) for $\sigma_{F\bar{F}^*} \cdot BR(F^{\pm} \rightarrow \eta\pi^{\pm})$ were derived in the same way as was done in the previous section for $F\bar{F}$ production. The upper limits were calculated for a F^* mass range of 2090 MeV –2200 MeV and are also shown in Figure 42 - 45 .

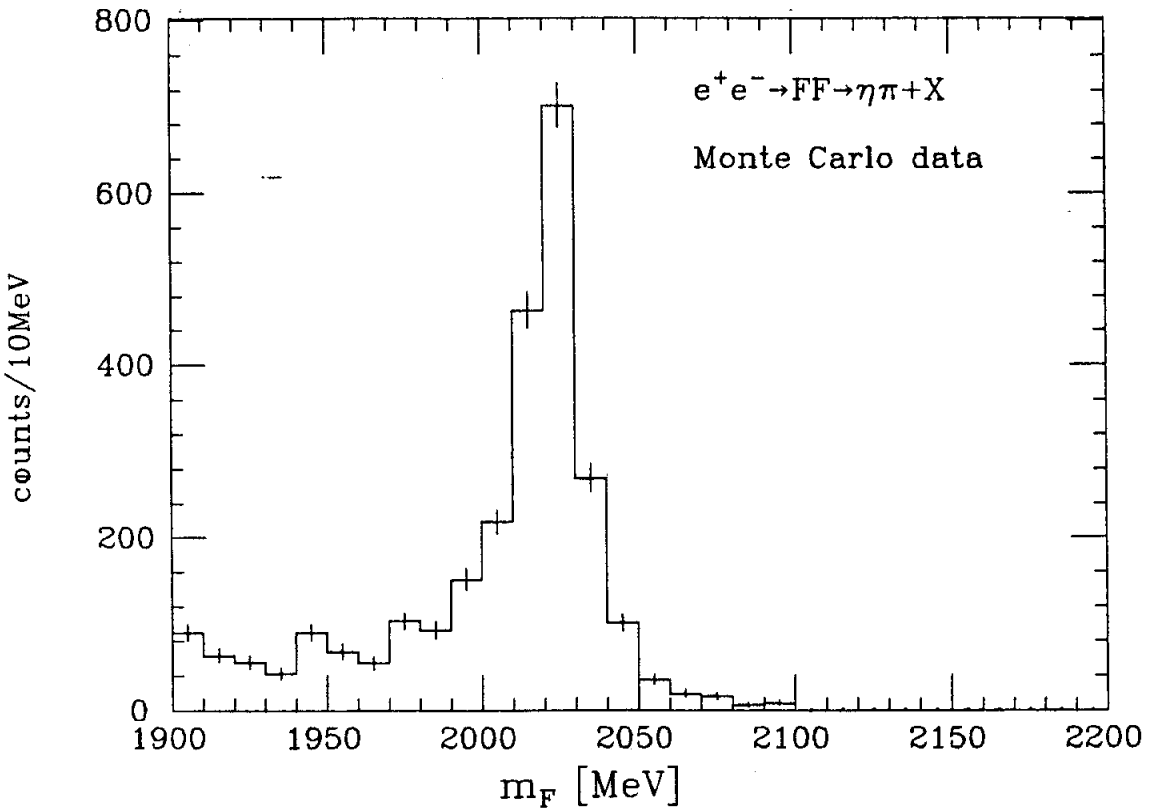

Figure 42. Invariant mass plot for Monte Carlo generated $F\overline{F}^*$ events, with on F having the decay $F^{\pm} \to \eta\pi^{\pm}$. $E_{cm} = 4.18\,\text{GeV}, 4.25\,\text{GeV}, 4.38\,\text{GeV}$

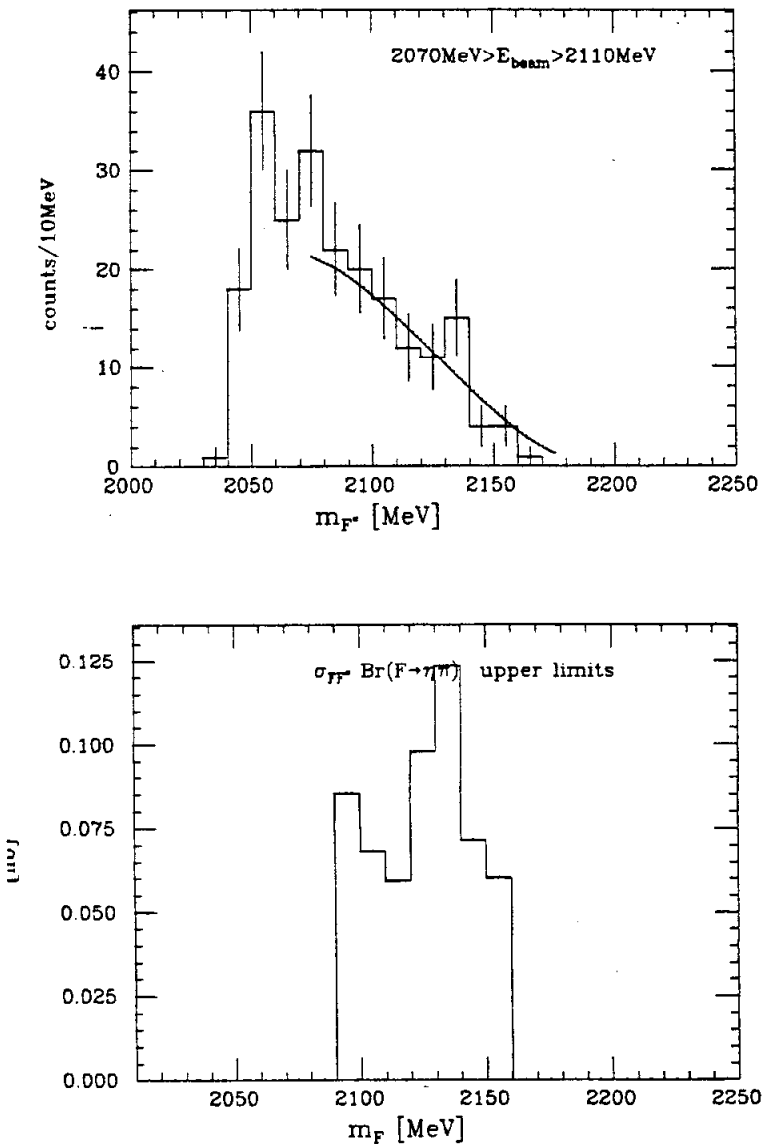

Figure 48. Invariant mass plot and Upper limits for $\sigma_{F\overline{F}^*} \cdot BR(F^{\pm} \to \eta\pi^{\pm})$ (95%CL)

$E_{cm} = 4.14\,\text{GeV} - 4.22\,\text{GeV}$

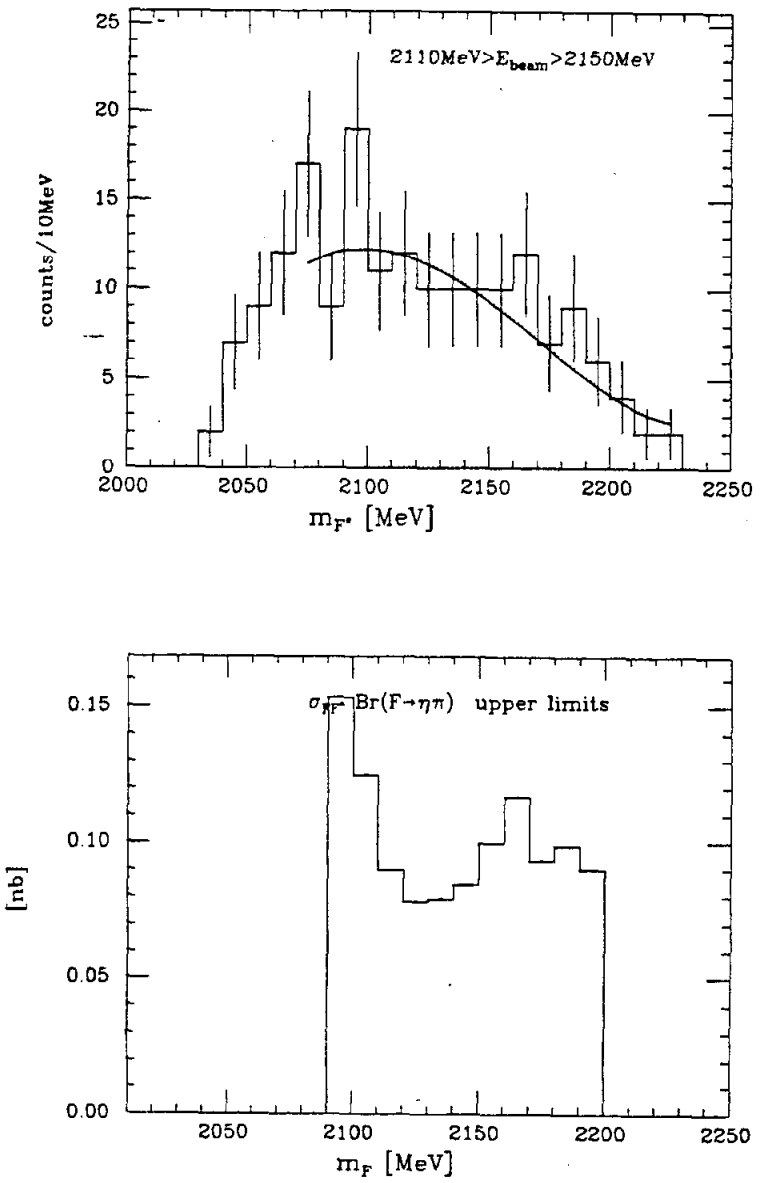

Figure 44. Invariant mass plot and Upper limits for $\sigma_{F\overline{F}^*} \cdot BR(F^{\pm} \to \eta\pi^{\pm})$ (95%*CL*)

$E_{cm} = 4.22\,\text{GeV} - 4.30\,\text{GeV}$

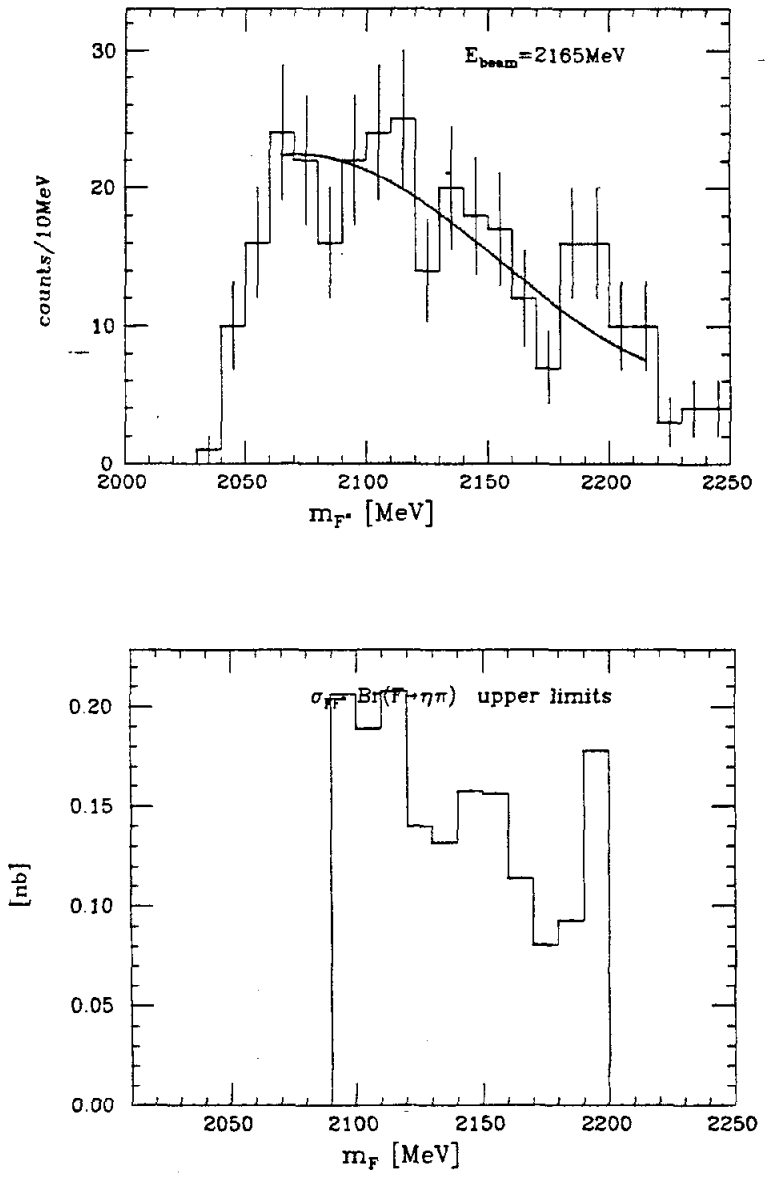

Figure 45. Invariant mass plot and Upper limits for $\sigma_{F\overline{F}^*} \cdot BR(F^{\pm} \to \eta\pi^{\pm})$ (95%CL)

$E_{cm} = 4.33\,\mathrm{GeV}$

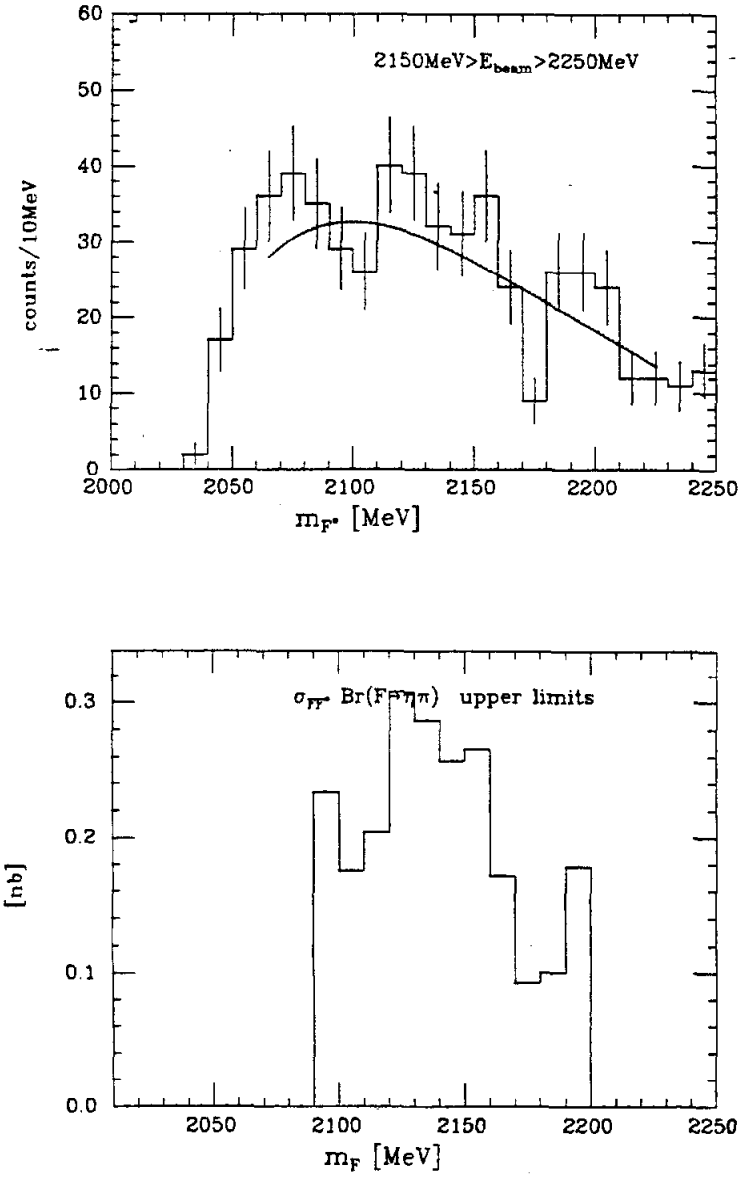

Figure 46. Invariant mass plot and Upper limits for $\sigma_{F\overline{F}^*} \cdot BR(F^{\pm} \to \eta\pi^{\pm})$ (95%CL)

$E_{cm} = 4.30\,\text{GeV} - 4.50\,\text{GeV}$

§6.5 FITS TO F^*F^* PRODUCTION

In this section the search for the reaction $e^+e^- \rightarrow F^*\bar{F}^* \rightarrow \gamma F + \gamma F$ with one F decaying into $\eta\pi^{\pm}$ is described. In a manner similar to the previous sections one measures the energies and direction cosines of the two transition γ's and the two γ's from the η decay and just the direction cosines for the charged track assuming it to be a $\pi^{\pm}$. With the two equal mass constraints for the F and F^* mass one is left with a 1-C-fit with a additional η mass constraint . This permits a search for the F and F^* meson without having to assume any specific F mass .

The cuts used were the same as for the previous fits with the only differnce that the γ's had to pass the "pattern cut" and not being labled a "split off" by the routine *SPLIT*. *SQUAW* was used to do the kinematic fitting and only the best fit with a confidence levle above 0.1 was used. For the passing fits one obtained the fitted $\eta\pi^{\pm}$ mass for the F mass and the $\gamma\eta\pi^{\pm}$ mass for the F^* mass. Instead of plotting m_F versus m_{F^*} the quantities m_{f^*} and $m_{F^*} - m_F$ were used. Plotting the F^* mass versus the $F^* - F$ mass splitting makes it easier to fit the final invariant mass peak .

Monte Carlo event were generated for different center of mass energies and also different $F^* - F$ mass splittings in order to obtain the invariant mass resolutions and efficiencies as a function of these quantities. Figure 47 shows the resulting invariant mass plot for the F^* mass and the $F^* - F$ mass splitting for Monte Carlo data at $E_{cm} = 4.33\,\text{GeV}$. The input masses in the Monte Carlo were 2030 MeV for the F mass and 2140 MeV for the F^* mass . The efficiency and the resolution of the $F^* - F$ mass splitting are constant as a function of $\Delta Q = E_{cm} - 2 \cdot m_{F^*\bar{F}^*}$. The width for the mass splitting was determined as 8.7 MeV. The $m_{F^*\bar{F}^*}$ mass resolution increases with growing ΔQ . At $\Delta Q = 20\,\text{MeV}$ the width is 4.8 MeV and at $\Delta Q = 100\,\text{MeV}$ it is 18.5 MeV . The efficinecy depends on the mass splitting and was determined as being $2.2\% \pm .7\%$ for a $F^* - F$ mass differnce of 110 MeV. For a mass difference of 60 MeV it was found to be 1.9% and for 160 MeV equal to 2.4%.

The data with $E_{cm} > 4.06\,\mathrm{GeV}$ was used and was divided into the same E_{cm} steps that had been used also before. Figure 47 -51 shows the final plots for the different E_{cm} steps. No obvious cluster of events is visible and these scatter plots were used to calculate upper limits for $\sigma_{F^*\bar{F}^*} \cdot BR(F^\pm \to \eta\pi^\pm)$. Since there are so few entries in these mass plots a likelihood method was used to derive the proper upper limits . The generalized likelihood function for N events with the probabilties $f(n_s, n_b)$ is :

$$L = \frac{e^{-(n_s+n_b)}}{N!} \cdot \prod_i^N f_i(n_s, n_b)$$

. whith n_s being the signal expectation value and n_b the background expectation value. For this case the probability $f_i(b_s, n_b)$ is the sum of a 2-dimensional gaussian probabilty distribution of known width and normalized to the signal expectation value n_s, and of a flat background distribution that is properly normalized to n_b. For the upper limits that were derived here the background area was taken to be a rectangle of 5 times the gaussian width in the F^* mass direction and of 6 times in the $F^* - F$ mass splitting direction. The upper limit for a given set of the F^* mass and the $F^* - F$ mass difference was then calculated by integrating the likelihood function over n_b and finding that specific n_s that leaves a certain fraction of the total normalisation outside. For the upper limits presented here this fraction was chosen to be 10% which then represents 90% confidence level . The systematic error of 35% that has to be assumed for the efficiency was taken into acount by convoluting the distribution of the likelihood function with a gaussian . The number of events for a $90\%CL$ upper limit is then used exactly as before with the approriate efficiency and luminosity to calculate upper limits for $\sigma_{F^*\bar{F}^*} \cdot BR(F^\pm \to \eta\pi^\pm)$. Table 6 - 10 give the upper limits for $\sigma_{F^*\bar{F}^*} \cdot BR(F^\pm \to \eta\pi^\pm)$ that correspond to the plots shown in Figure 47 -51 .

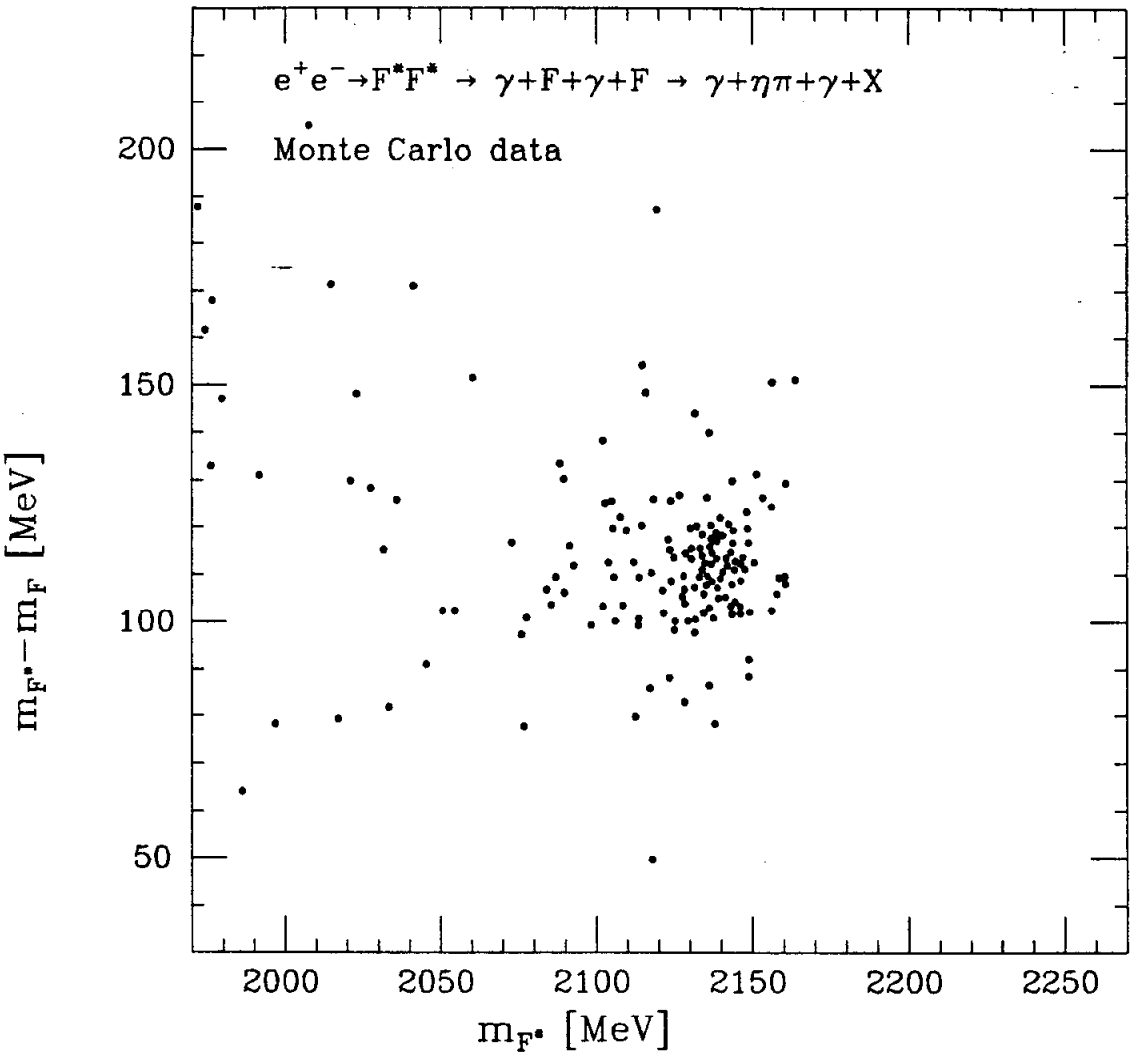

Figure 47. Invariant mass plot for Monte Carlo generated $F^*\overline{F}^*$ events, with one F having the decay $F^{\pm} \to \eta\pi^{\pm}$. $E_{cm} = 4.33\,\text{GeV}$

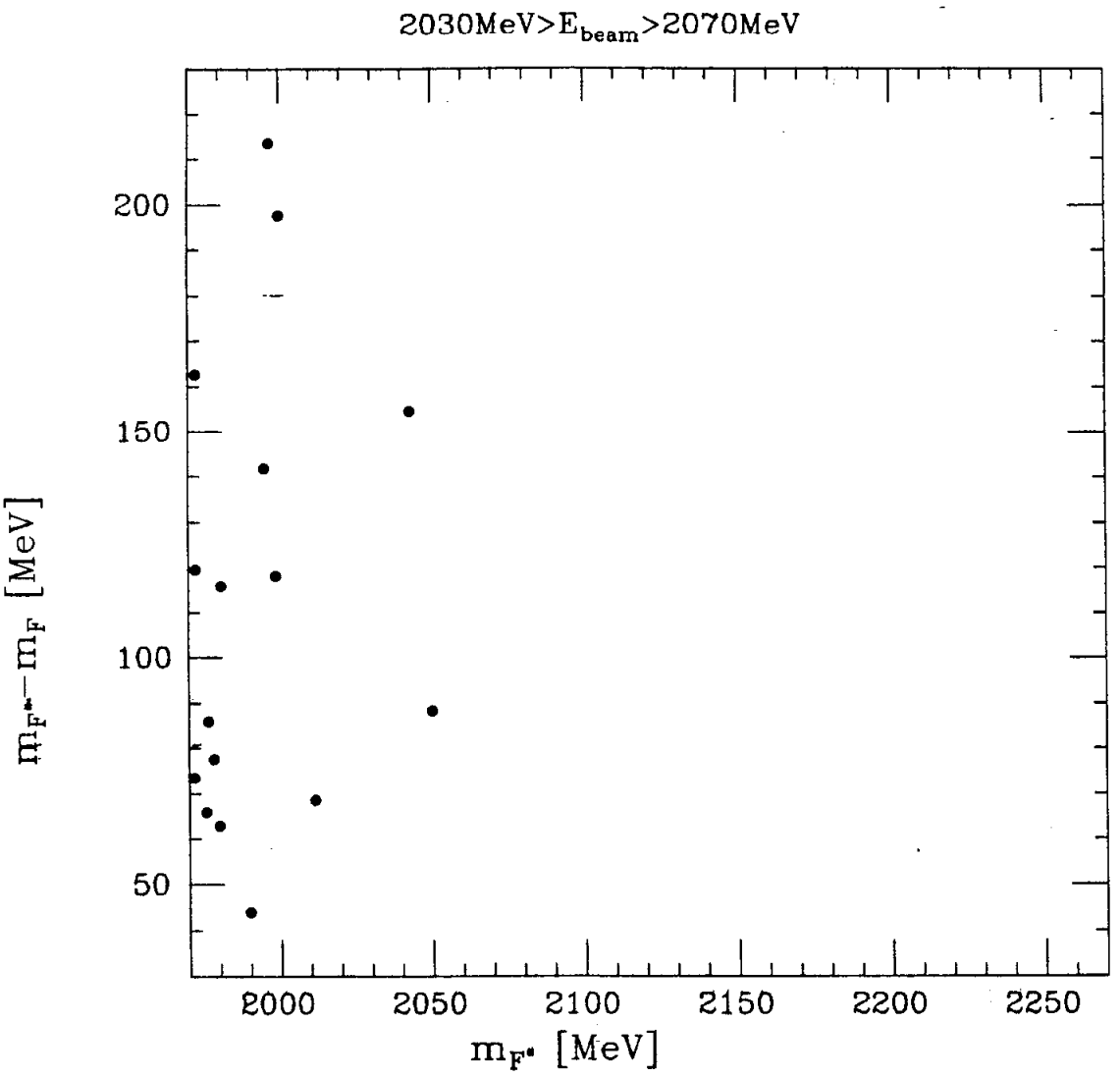

Figure 48. Invariant mass plot for m_{F^*} versus $m_{F^*} - m_F$

1 count $\Leftrightarrow$ $\sigma_{F^*\bar{F}^*} \cdot BR(F^{\pm} \to \eta\pi^{\pm}) \approx 0.029nb$

$E_{cm} = 4.06\,\text{GeV} - 4.14\,\text{GeV}$

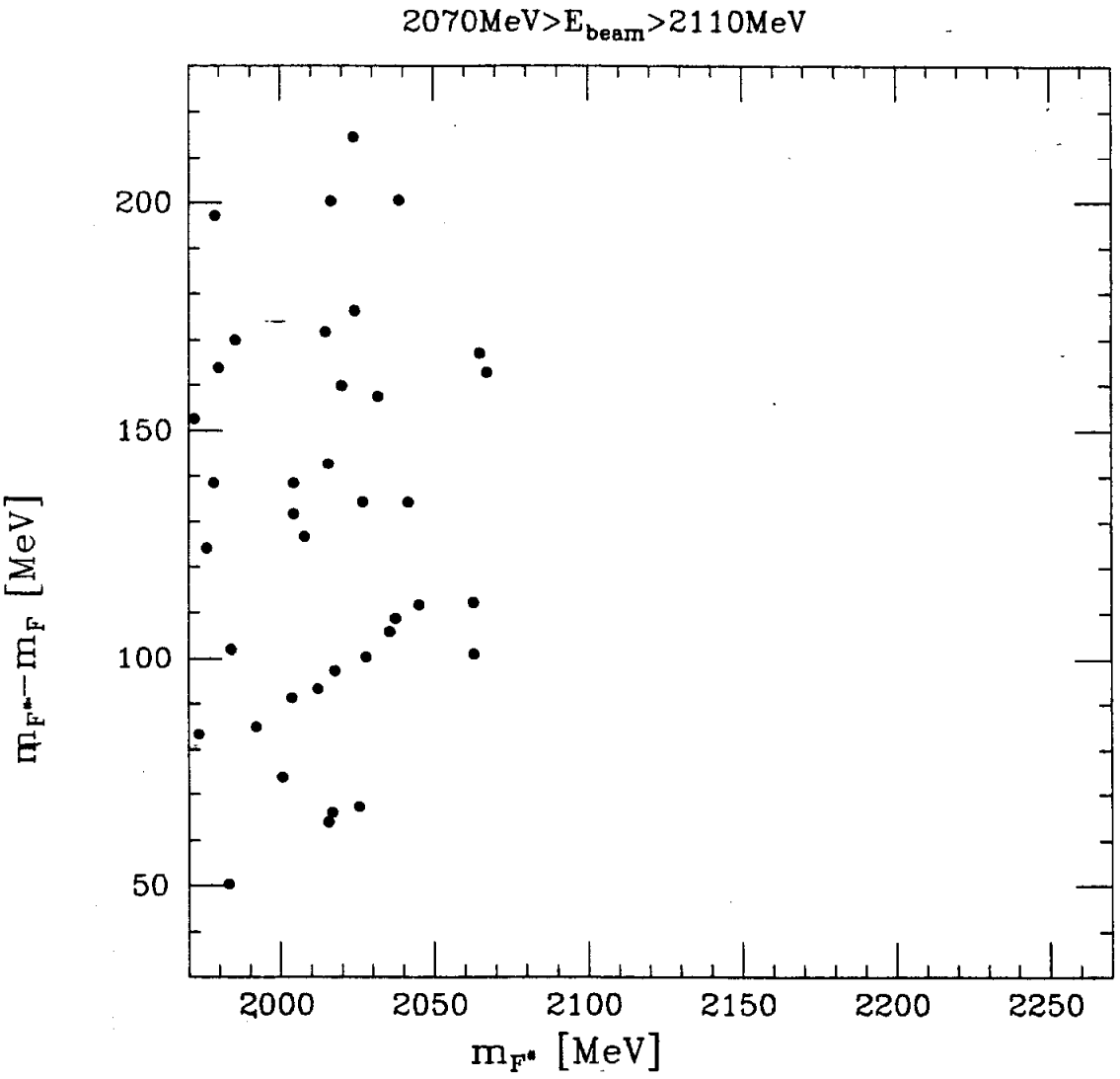

Figure 49. Invariant mass plot for m_{F^*} versus $m_{F^*} - m_F$

1 count $\Leftrightarrow$ $\sigma_{F^*\bar{F}^*} \cdot BR(F^{\pm} \to \eta\pi^{\pm}) \approx 0.027nb$

$E_{cm} = 4.14\,\text{GeV} - 4.22\,\text{GeV}$

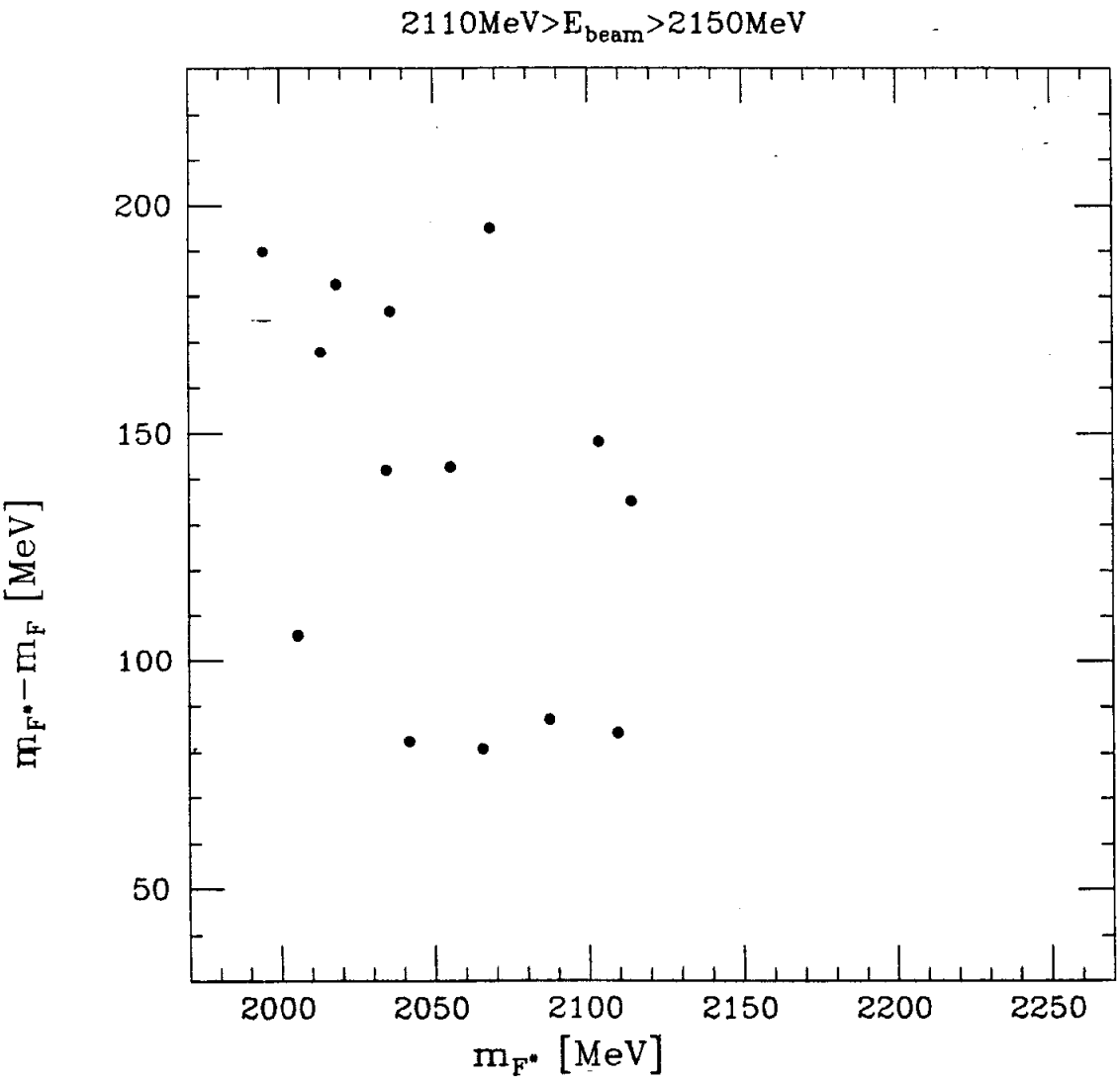

Figure 50. Invariant mass plot for m_{F^*} versus $m_{F^*} - m_F$

1 count $\Leftrightarrow$ $\sigma_{F^*\overline{F}^*} \cdot BR(F^{\pm} \to \eta\pi^{\pm}) \approx 0.048nb$

$E_{cm} = 4.22\,\text{GeV} - 4.30\,\text{GeV}$

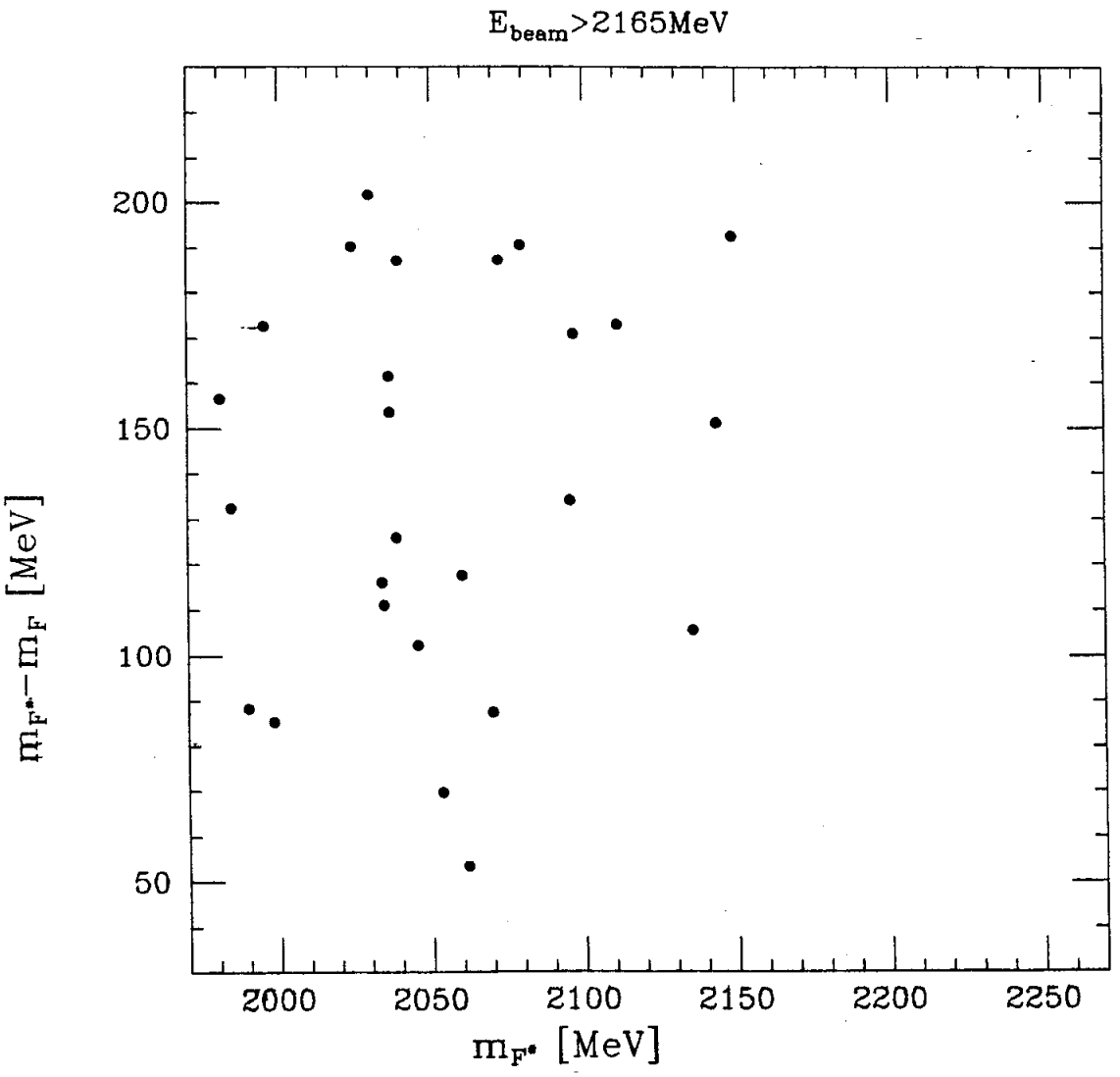

Figure 51. Invariant mass plot for m_{F^*} versus $m_{F^*} - m_F$

1 count $\Leftrightarrow$ $\sigma_{F^*\overline{F}^*} \cdot BR(F^{\pm} \to \eta\pi^{\pm}) \approx 0.039nb$

$E_{cm} = 4.33\,\mathrm{GeV}$

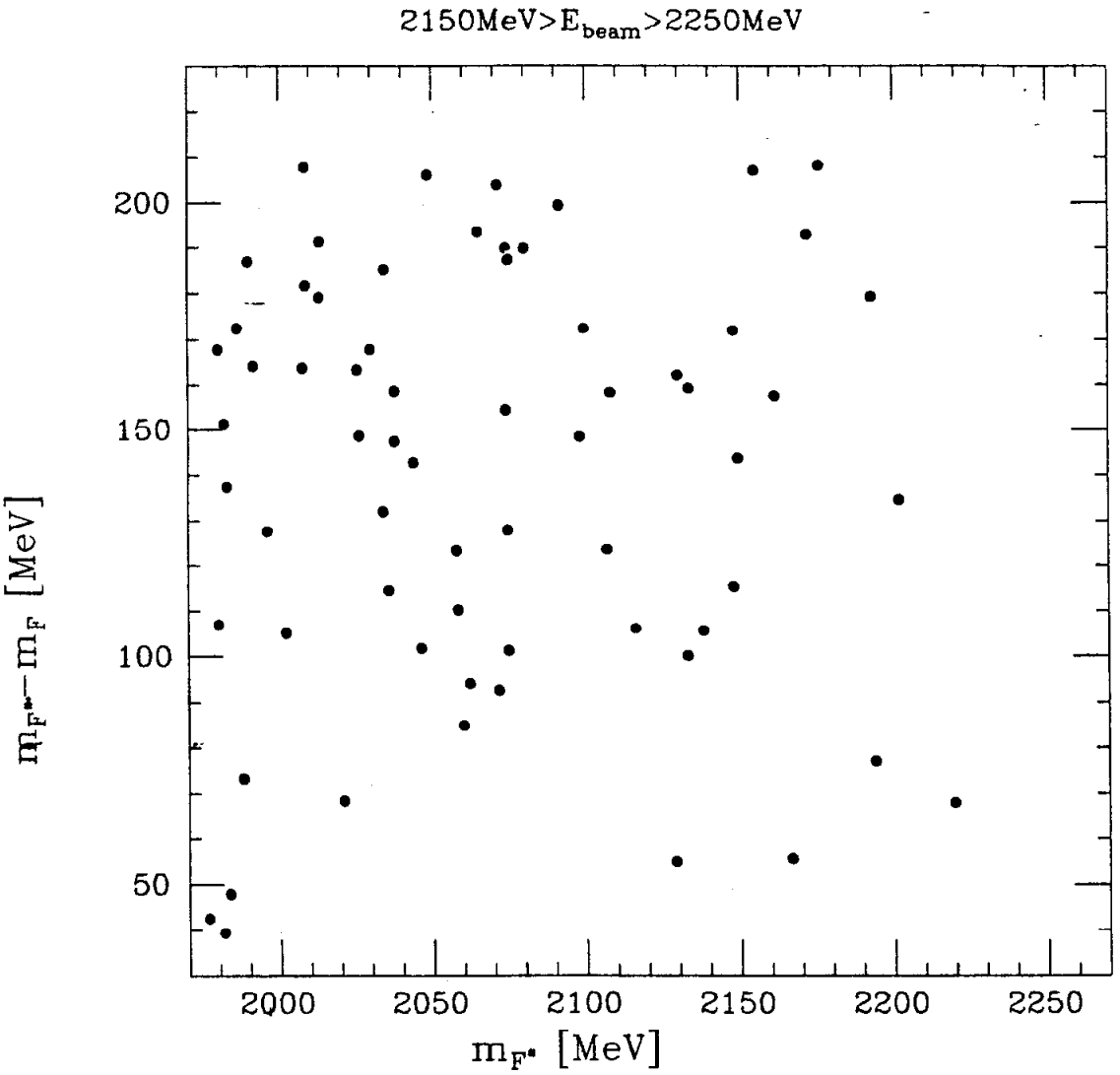

Figure 52. Invariant mass plot for m_{F^*} versus $m_{F^*} - m_F$

1 count $\Leftrightarrow$ $\sigma_{F^*\bar{F}^*} \cdot BR(F^{\pm} \to \eta\pi^{\pm}) \approx 0.025nb$

$E_{cm} = 4.30\,\text{GeV} - 4.50\,\text{GeV}$

	$m_{F^*} - m_F$ [MeV]								
m_{F^*}[MeV]	50	70	90	110	130	150	170	190	210
2000	0.15	0.31	0.11	0.18	0.14	0.13	0.09	0.10	0.09
2020	0.12	0.11	0.11	0.10	0.10	0.11	0.08	0.09	0.08
2040	0.10	0.11	0.13	0.08	0.08	0.11	0.10	0.07	0.07
2060	0.17	0.17	0.16	0.15	0.15	0.14	0.14	0.14	0.14

Table 6 Upper limits (90%CL) for $\sigma_{F^*F^*} \cdot BR(F^{\pm} \to \eta\pi^{\pm})$ in [nb]

for $E_{cm} = 4.06\,\text{GeV} - 4.14\,\text{GeV}$.

	$m_{F^*} - m_F$ [MeV]								
m_{F^*}[MeV]	50	70	90	110	130	150	170	190	210
2000	0.16	0.42	0.27	0.18	0.30	0.20	0.26	0.14	0.07
2020	0.15	0.28	0.25	0.24	0.29	0.17	0.23	0.11	0.09
2040	0.11	0.18	0.19	0.29	0.22	0.18	0.27	0.10	0.08
2060	0.07	0.09	0.10	0.24	0.10	0.11	0.15	0.08	0.08
2080	0.11	0.10	0.10	0.13	0.08	0.11	0.13	0.08	0.08
2100	0.29	0.28	0.26	0.25	0.24	0.23	0.23	0.23	0.22

Table 7 Upper limits (90%CL) for $\sigma_{F^*F^*} \cdot BR(F^{\pm} \to \eta\pi^{\pm})$ in [nb]

for $E_{cm} = 4.14\,\text{GeV} - 4.22\,\text{GeV}$.

	$m_{F^*} - m_F$ [MeV]								
m_{F^*}[MeV]	50	70	90	110	130	150	170	190	210
2000	0.14	0.19	0.27	0.21	0.12	0.17	0.27	0.31	0.14
2020	0.14	0.23	0.26	0.20	0.17	0.19	0.32	0.31	0.14
2040	0.14	0.27	0.33	0.19	0.18	0.21	0.28	0.31	0.14
2060	0.14	0.29	0.40	0.13	0.19	0.20	0.19	0.23	0.15
2080	0.14	0.29	0.38	0.13	0.22	0.22	0.15	0.19	0.16
2100	0.14	0.24	0.29	0.13	0.22	0.22	0.11	0.13	0.11
2120	0.18	0.21	0.27	0.18	0.27	0.25	0.15	0.14	0.14
2140	0.71	0.69	0.66	0.63	0.60	0.57	0.55	0.56	0.57

Table 8 Upper limits (90%*CL*) for $\sigma_{F^*F^*} \cdot BR(F^\pm \to \eta\pi^\pm)$ in [*nb*]

for $E_{cm} = 4.22\,\text{GeV} - 4.30\,\text{GeV}$.

	$m_{F^*} - m_F$ [MeV]								
m_{F^*}[MeV]	50	70	90	110	130	150	170	190	210
2000	0.12	0.23	0.26	0.19	0.18	0.25	0.19	0.23	0.12
2020	0.17	0.19	0.26	0.25	0.23	0.20	0.22	0.27	0.15
2040	0.21	0.22	0.24	0.36	0.26	0.19	0.22	0.34	0.15
2060	0.22	0.26	0.23	0.36	0.25	0.18	0.20	0.30	0.13
2080	0.19	0.24	0.19	0.22	0.21	0.15	0.22	0.23	0.12
2100	0.17	0.17	0.15	0.16	0.16	0.16	0.20	0.24	0.11
2120	0.11	0.10	0.13	0.17	0.13	0.15	0.19	0.17	0.11
2140	0.11	0.10	0.13	0.17	0.10	0.15	0.13	0.15	0.10
2160	0.11	0.10	0.10	0.09	0.09	0.09	0.08	0.08	0.08

Table 9 Upper limits (90%*CL*) for $\sigma_{F^*F^*} \cdot BR(F^\pm \to \eta\pi^\pm)$ in [*nb*]

for $E_{cm} = 4.33\,\text{GeV}$.

	$m_{F^*} - m_F$ [MeV]								
m_{F^*}[MeV]	50	70	90	110	130	150	170	190	210
2000	0.22	0.14	0.11	0.17	0.14	0.18	0.30	0.16	0.08
2020	0.13	0.13	0.11	0.14	0.13	0.22	0.21	0.16	0.07
2040	0.08	0.13	0.18	0.22	0.18	0.24	0.16	0.17	0.08
2060	0.07	0.11	0.26	0.26	0.17	0.22	0.09	0.21	0.09
2080	0.07	0.08	0.24	0.21	0.13	0.12	0.10	0.20	0.09
2100	0.11	0.08	0.15	0.15	0.11	0.17	0.13	0.19	0.08
2120	0.13	0.09	0.14	0.24	0.11	0.20	0.14	0.09	0.06
2140	0.12	0.11	0.13	0.24	0.11	0.21	0.17	0.08	0.08
2160	0.15	0.12	0.11	0.16	0.11	0.17	0.17	0.12	0.12
2180	0.15	0.18	0.13	0.10	0.13	0.13	0.16	0.18	0.15
2200	0.14	0.26	0.18	0.12	0.18	0.14	0.16	0.16	0.13

Table 10 Upper limits (90%CL) for $\sigma_{F^*F^*} \cdot BR(F^{\pm} \to \eta\pi^{\pm})$ in [nb]

for $E_{cm} = 4.30\,\text{GeV} - 4.50\,\text{GeV}$.

Chapter 7

SUMMARY AND CONCLUSIONS

The Crystal Ball experiment has taken data at SPEAR over a center of mass energy range from 3.86 GeV to 4.50 GeV . In this analysis a search has been made for evidence of the production of charmed F or F^* mesons using a total integrated luminosity of $10370nb^{-1}$ over the above mentioned center of mass energy range.

The evidence for the existence of F and F^* mesons up to the date of this analysis have come mainly from three different experiments and have been reviewed in Chapter 1 . I will just briefly recall the most important points. The DASP experiment had reported the observation of a significant increase in the inclusive η production ($e^+e^- \rightarrow \eta + X$) at $E_{cm} \approx 4.4$ GeV compared to 4.03 GeV which they intepreted as evidence for the production of F mesons. This was supported also by their observation of $e^+e^- \rightarrow F^*\overline{F} \rightarrow \gamma F\overline{F}$, with $F^{\pm} \rightarrow \eta\pi^{\pm}$ at $E_{cm} = 4.42$ GeV. From this measurement they obtained a mass for the F meson of 2030 ± 60 MeV and a mass difference between the F^* meson and the F meson of 110 ± 4.6 MeV . Subsequent photoproduction experiments (WA4 and WA57) observed F signals in $\eta\pi$, $\eta 2\pi$, $\eta 3\pi$,$\eta 5\pi$,$\eta' 3\pi$ and $\Phi\rho$ which fixed the F mass to the value 2021 ± 15.2 MeV that is , at present , quoted by the Particle Data Group.

Three different measurements have been made with the Crystal Ball detector to search for evidence of $F^{(*)}$ production in e^+e^- collisions. First: An inclusive η production measurement similar to the DASP measurement. Second: A search for the decay $F^* \rightarrow \gamma F$ by searching for a

doppler broadened photon line in the inclusive γ spectrum. Third:A search for $F\overline{F}$, $F\overline{F}^*$, F^*F^* events with one F having the decay $F^{\pm} \rightarrow \eta\pi^{\pm}$ and the other F going to "anything" .

The measurement of cross section of the inclusive η production ($e^+e^- \rightarrow \eta + X$) was done for η's with $E_\eta > 700\,\mathrm{MeV}$. The whole E_{cm} range (3.86 GeV - 4.50 GeV) was divided into 8 different energy steps . The resulting cross sections are presented as $R_\eta = \sigma(e^+e^- \rightarrow \eta + X)/\sigma(e^+e^- \rightarrow \mu^+\mu^-)$. They do not show any strong variation as a function of the center of mass energy . The smallest cross section of 0.36 ± 0.09 is observed for the lowest E_{cm} step with $E_{cm} = 3.86 - 4.00\,\mathrm{GeV}$. The biggest cross section was 0.54 ± 0.05 for $E_{cm} = 4.22 - 4.30\,\mathrm{GeV}$. Although there is some variation of the observed η production cross section over the E_{cm} region it is consistent with being constant. It does certainly not follow the inclusive η cross section that was obtained by the DASP experiment. A comparison of the two cross sections shows that the Crystal Ball measurement has a slight dip at $\approx 4.15\,\mathrm{GeV}$ where DASP had a maximum , and the Crystal Ball measurement has a maximum at $\approx 4.25\,\mathrm{GeV}$ where the DASP group had reported a minimum in the cross section . There is also no sign of any steplike increase in R_η at $E_{cm} \approx 4.42\,\mathrm{GeV}$ as was indicated by the DASP result. This analysis therefore fails to confirm the conclusion drawn by the DASP group that there is a F meson "factory" at $E_{cm} \approx 4.4\,\mathrm{GeV}$ which would be responsible for an increase in η production at this center of mass energy.

The inclusive γ spectrum at $E_{cm} = 4.33\,\mathrm{GeV}$ has been used to search for a doppler broadened photon line that one expects to observe for the process $e^+e^- \rightarrow F^*F^{(*)}$ with the subsequent decay $F^* \rightarrow \gamma F$. No indication for such a photon line has been found in the data and a series of upper limits were derived for the cross section times branching ratio $\sigma(e^+e^- \rightarrow F^*\overline{F}^*) \cdot BR(F^* \rightarrow \gamma F)$. There is only a limited range of F^* masses that can be covered by this method. For lower F^* masses the increasing doppler broadening of the photon line decreases the sensitivity for detection and for higher F^* masses one is limited with the center of mass energy. For the case of $F^*\overline{F}^*$ production the covered F^* mass range goes from 2090 MeV to 2160 MeV . For $F\overline{F}^*$ production the F^* mass ranges from 2160 MeV up to 2190 MeV and from 2200 MeV

up to 2290 MeV assuming $m_F = 2030\,\text{MeV}$. Since for all the different F^* masses considered the $F^* - F$ mass difference is less than two pion masses one can therefore quite safely assume $BR(F^* \to \gamma F) = 100\%$. Thus the upper limits mentioned above reduce to upper limits for the production cross section $\sigma(e^+e^- \to F^*\overline{F}^{(*)})$ alone . For $F^*\overline{F}^*$ production the upper limits (95%CL) for $\sigma_{F^*\overline{F}^*}$ vary between 0.28 nb for $m_{F^*} = 2160\,\text{MeV}$ and 0.82 nb for $m_{F^*} = 2090\,\text{MeV}$. For $F\overline{F}^*$ production the limits range between 0.57 nb for $m_{F^*} = 2290\,\text{MeV}$ and 2.05 nb for $m_{F^*} = 2160\,\text{MeV}$. For the F^* mass of 2140 MeV that was quoted by the DASP group the upper limit for $\sigma_{F^*\overline{F}^*}$ is 0.37 nb . This value is substantially below the cross section that is predicted by the charged coupled channel model which gives a $F^*\overline{F}^*$ production cross section of 0.92 nb for the DASP masses at $E_{cm} = 4.33\,\text{GeV}$. Combining this upper limit for $\sigma_{F^*\overline{F}^*}$ with the upper limit $BR(F^\pm \to \eta\pi^\pm) < 0.16$ as given by the results from the photoproduction experiments one obtains an upper limit of $\sigma_{F^*\overline{F}^*} \cdot BR(F^\pm \to \eta\pi^\pm) < 0.059\,nb$. Unfortunately , this cannot directly be compared with $\sigma_{F\overline{F}^*} \cdot BR(F^\pm \to \eta\pi^\pm) = 0.41 \pm 0.18\,nb$ that was claimed by the DASP group in the E_{cm} region 4.36 GeV – 4.49 GeV , but one would expect to observe a comparable cross section at $E_{cm} = 4.33\,\text{GeV}$ as indicated by the coupled channel model . In connection with the analysis of the inclusive γ spectrum at $E_{cm} = 4.33\,\text{GeV}$ a measurement of the π^0 energy spectrum was done. The spectrum shows a prominent peak at $E_{\pi^0} \approx 155\,\text{MeV}$ that stems from the production of D^* mesons with the subsequent decay $D^* \to \pi^0 D$. This one allows to measure the inclusive D^* production if one assumes isospin invariance for the production cross sections of charged and neutral D^* mesons . The resulting cross section σ_{D^*} was found to be $7.4\,nb \pm 1.1\,nb \pm 1.3\,nb$ with the first error being statistical and the second error being systematic . The charged coupled channel model predicts a cross section of $\sigma_{D^*} = 5.4\,nb$ which has no radiative corrections ($\approx 20\%$) added to it and which is consistent with the measured value.

A search for charmed F and F^* mesons has been done for $F\overline{F}$, $F\overline{F}^*$ and $F^*\overline{F}^*$ production with one F having the subsequent decay $F^\pm \to \eta\pi^\pm$ whereas the second F can decay into "anything" . The F and F^* signal have been searched for by plotting the $\eta\pi^\pm$ invariant mass after having fitted the event to four momentum conservation and additional equal mass constraints . The data

show no convincing signal for F or F^* production in any of the three different production channels. Upper limits were calculated for various F masses and F^* masses for the different center of mass energy ranges.

For $F\overline{F}$ production and a F mass of 2021 MeV the upper limits (95%CL) for the cross section time branching ratio $\sigma_{F\overline{F}} \cdot BR(F^{\pm} \rightarrow \eta\pi^{\pm})$ vary between 0.1 nb and 0.3 nb .

For $F\overline{F}^*$ production the events were fitted to a F mass of 2021 MeV and a search was done for a signal in the $\gamma\eta\pi^{\pm}$ invariant mass plot as an indication of the F^* meson. No signal has been observed , and upper limits (95%CL) were derived for the cross section time branching ratio $\sigma_{F\overline{F}^*} \cdot BR(F^{\pm} \rightarrow \eta\pi^{\pm})$ for different F^* masses and different center of mass energy ranges. For the $F^* - F$ mass difference of 110 MeV $\pm$4.6 MeV that was quoted by the DASP experiment the upper limits range between 0.09 nb and 0.29 nb . This is in disagreement with the results from the DASP group which had given a combined cross section times braching ratio of 0.41 $nb \pm 0.18$ nb in the center of mass energy region 4.36 GeV $-$4.49 GeV .

The production of $F^*\overline{F}^*$ events with the observation of both transition γ's from $F^* \rightarrow \gamma F$ and of the decay $F^{\pm} \rightarrow \eta\pi^{\pm}$ gives an additional equal mass constraint . This allowed the search for a correlated signal of the $\eta\pi^{\pm}(= m_F)$ invariant mass and of the $\gamma\eta\pi^{\pm}(= m_{F^*})$ invariant mass. The data show no such signal for any of the different center of mass energy steps , and upper limits (90%CL) for the cross section times branching ratio $\sigma_{F\overline{F}^*} \cdot BR(F^{\pm} \rightarrow \eta\pi^{\pm})$ for different F^* masses and different $F^* - F$ mass splittings were derived. For an F mass of 2021 MeV and an $F^* - F$ mass splitting of 110 MeV the upper limits vary between 0.17 nb and 0.24 nb for the different center of mass energy ranges . For the F and F^* masses given above , the charged coupled channel model for open charm production shows that the maximal $F\overline{F}^*$ cross section is about of the same size as the maximal cross section obtained for $F^*\overline{F}^*$ production . One would therefore expect that a signal would have been observed for $F^*\overline{F}^*$ production if the DASP results for the F and F^* masses and for the combined signal times branching ratio were correct .

Concluding one can say that the search for the production of the charmed F and F^* mesons in e^+e^- collisions at $E_{cm} = 3.86\,\text{GeV} - 4.50\,\text{GeV}$ with the Crystal Ball experiment has not been able to confirm the previous results for the masses as well as the cross section that had been reported by the DASP group and the photoproduction experiments . Some of the results of this analysis are strictly inconsistent and some results are only weakly in contradiction with the previous results and some are inconsistent with theoretical predictions for an F mass of $2021.1 \pm 15.2\,\text{MeV}$ and a $F^* - F$ mass splitting of $110 \pm 4.6\,\text{MeV}$. Altogether these results cast serious doubts on the claim that the charmed F and F^* mesons have been discovered at the reported mass .

After having completed this analysis and while preparing this manuscript new evidence for the production of F mseons in e^+e^- collisions at $E_{cm} = 10.5\,\text{GeV}$ has been reported by the CLEO experiment .[1] They have been looking for the decay mode $F^\pm \to \phi\pi^\pm$ and observed a peak at an invariant mass of $1970 \pm 5\,\text{MeV}$.

[1] R. Ehrlich , SLAC Summer Institute July 27-29 , 1983

APPENDIX A : TUBE CHAMBERS

The Fall 81 data used in this analysis were taken with a new set of central tracking chambers consisting of 6 layers of tube chambers with charge division read out. The 6 layers are arranged as 3 double layers with each double layer being split into two cylindrical half shells for easier mounting around the beam pipe. The innermost double layer consists of two times 80 tubes at a radius of 6.16 cm and covers a solid angle of 98% of 4π around the interaction point. The middle double layer has the same number of tubes but at a radius of 7.16 cm and covers a solid angle of 96% of 4π. The outermost double layer has 2 times 160 tubes with a chamber radius of 14.3 cm and covers 75% of the full solid angle. The aluminum tubes have a wall thickness of 0.08 mm which has been achieved by starting out with thicker tubes and reducing their wall thickness to the desired value by chemical etching. The tubes of each double layer are glued between two 0.25 mm thick sheets of G10 (epoxy fortified glass fibre cloth) , resulting in a a very light but mechanically stiff sandwich construction. The inner sheet of G10 has an additional layer of 0.05 mm of copper in order to provide a stable electric ground across the tube length. Each double layer has a thickness of 0.94% raditation length at normal incidence. Together with the 1.65 mm thick aluminum beam pipe this results in 4.93% radiation length of converting material for photons at perpendicular direction to the beam.

Each tube has a 45μm thick stainless steel anode wire with a a total resistance of $\approx 300\Omega$ over the full tube lenght. Two charge sensitive amplifiers are mounted on each side of the chamber

in order to measure the z position of the chamber hit by charge division read out . Each amplifier drives a 50Ω coaxial cable that brings the pulse to the counting room where the signal is digitized and written to tape along with all the other data from the event. In order to calculate the z position of a hit from the measured chamber pulses, one needs to know the gain ratios of the two amplifiers as well as their input impedances. The input impedances have a dependence on the input pulse height that are assumed to be inversly proportional to the input pulse current. Together with the two pedestals one needs therefore 5 constants for each tube in order to calculate the proper z position of a track hit.

For the 640 tubes these constants are determined by a calibration procedure that uses Bhabha events . One first starts with the pedestals by selecting uncompressed events and looking at signals of tubes that have no charged tracks passing through . In a next step the directions of the Bhabha tracks are reconstructed using the observed energy deposition in the central ball and the intersection of the Bhabha tracks with the different chamber layers is calculated. By integrating over many Bhabha events and minimizing the quantity $\chi^2 = \sum(z_{hit} - z_{calc})^2$ one is then able to fit the other 3 constants for each tube as well as the geometric position of the chambers relative to the central ball. For the calibration of the Fall 81 data the input impedances were held at a fixed value and only the gain ratios were fit . This was done since the dependence of χ^2 on the input impedance did not seem very strong and the fits sometimes had difficulties to converge with all the 3 constants as free parameters.

The resulting z-resolution obtained from the charge division read-out has been measured on real data events . This measurement was done for the 3 double layers by plotting the z-differences between pairs of chamber hits of two subsequent layers with an additional correction due to the angle between the track and the beam and the slightly different radii of the two layers . Figure 53 a).-c). shows the resulting distribution for the 3 double layers (a). innermost ; b). middle ; c). outermost double layer). The distributions were fit with two gaussians and a flat backgound in order to accomodate for long non gaussian tails. The Monte Carlo simulation of the proportional tube chambers was adjusted to the values measured in real hadronic data by smearing the simulated

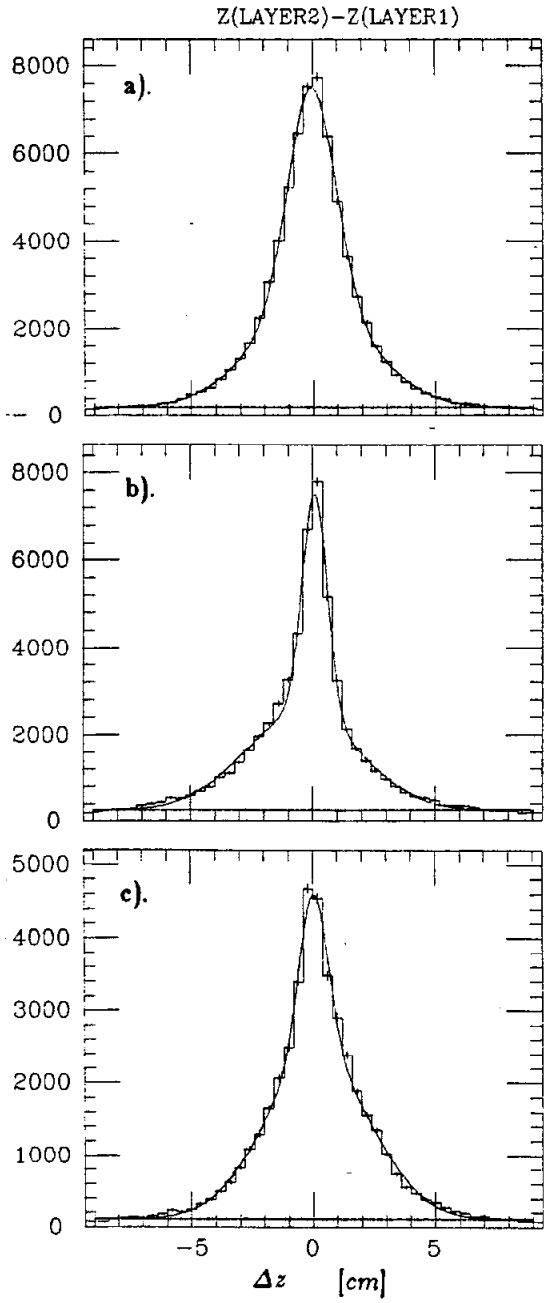

Figure 58. Observed tube chamber Δz-resolution $[cm]$ of the 3 double layers from hadronic data. a). innermost ; b). middle ; c). outermost double layer . Fits were done with two gaussians.

generated chamber hits with two gaussians of same mean but different width in order to obtain the same z-resolution as is observed in real data.

The efficiencies used in the Monte Carlo program were measured on Bhabha events. The Bhabha events were selected by according to following criteria:

1). $N_{conreg} = 2$, (N_{conreg} = number of connected regions)

2). 2 tracks with $x > 0.9$, where $x = E_{track}/E_{beam}$, plus one possible extra track with $E < 100\,\mathrm{MeV}$. The 2 high energy tracks were required to be collinear within 18.2^0.

3). $0.9 > f_E > 1.1$, with f_E being the total energy fraction . ($f_E = E_{ball}/E_{cm}$)

For the efficiency calculation only tracks were considered that were going through the outermost chamber and were not within a $4cm$ fiducial region from each end . This left only tracks in a solid angle of 63% of 4π. The direction cosines of the tracks were determined from the energy deposition in the central ball and chamber hits were accepted for the efficiency calculation only within a ϕ window of 200 $mrad$. No z window was used in the efficiency calculation for the tube chambers since the tracking code used in the analysis of the Fall 81 data applied only ϕ tagging to associate chamber tracks with the energy depositions in the central ball. The efficiencies that were obtained for the different layers averaged over the whole Fall 81 data sample are shown in Table 11 . The values that are quoted are not just the average single tube efficiencies for each layer but also contain the efficiency loss due to dead tubes . The errors that are indicated are statistical only. All Monte Carlo simulations that were done for the analysis of the Fall 81 data at $E_{cm} = 4.33\,\mathrm{GeV}$ used the efficiencies that are given in Table 11 .

Tube chamber efficiencies averaged for Fall 81	
Layer	Efficiency
1	0.80±0.01
2	0.76±0.01
3	0.78±0.01
4	0.77±0.01
5	0.78±0.01
6	0.73±0.01

Table 11. Average tube chamber efficiency from Fall 81 data used in Monte Carlo chamber simulation.

APPENDIX B : SPARK CHAMBER EFFICIENCIES AND NOISE HITS

In connection with the reanalysis of the Spring 79 data and Spring 80 data and the subsequent hadron selection the efficinecies for the magnetostrictive spark chambers and the multiwire proportional chambers (MWPC) were measured in order to have the proper gap efficiencies for the Monte Carlo simulation. In addition to this an attempt was also made to remove noise hits in the spark chambers.

The measurement of the chamber efficiencies was done on Bhabha events at the stage of the hadon selection. The Bhabha events were selected according to the QED cut that is described in the hadron selection cuts of Chapter 3 with the additional requirement of having 2 IR-tracks in the event. These IR-tracks were used for the measurement of the efficiencies of the 12 chamber planes. The two spark chambers and the MWPC have each two ϕ planes and two ψ planes that are helically wound in order measure the z position of the track. For the inner (outer) spark chambers the angle of inclination was $30^0(45^0)$ and for the MWPC it was 62^0 for the inner gap and 90^0 for the outer one. The efficiency for a certain plane was measured by establishing the track without needing a hit on this plane and then measure the efficiency by comparing the number of hits found with the number of tracks considered. Hits were accepted when they were within a window of 100 $mrad$ for the ϕ plane and within 200 $mrad$ for the ψ plane. The same windows were also used for MWPC planes with exception of the 90^0 plane which was directly calibrated in cm and had a

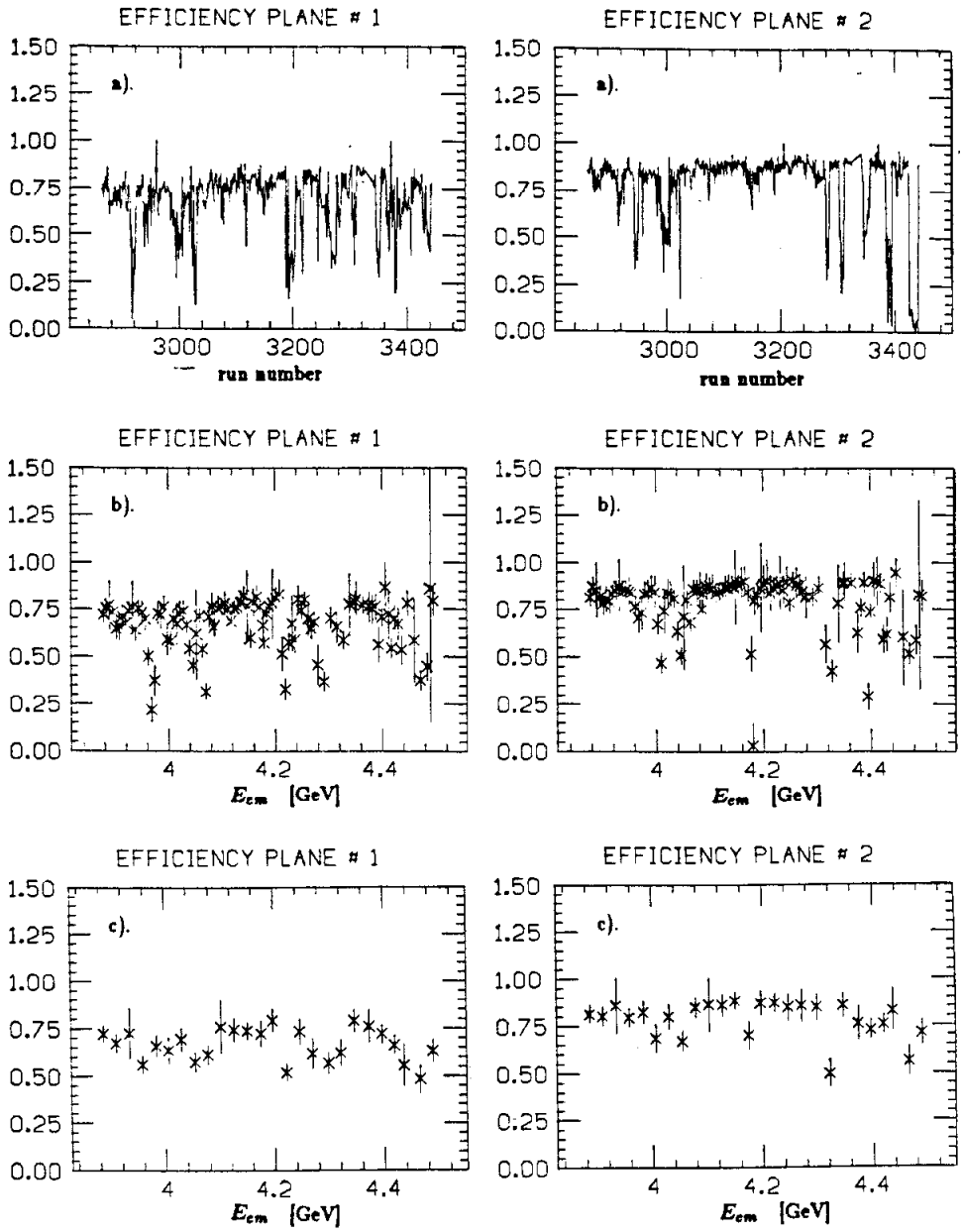

Figure 54. Chamber efficiencies for inner gap of inner spark chamber for Spring 79 data. a). as function of run number; b). as function of E_{cm} ; c). as function of E_{cm}[20MeV steps];

1.0 *cm* window. The efficiencies were measured for each run and the results show a variations on a run by run basis. Figure 54 a) gives the resulting efficiencies of the inner ψ and ϕ plane of the inner spark chamber as a function of the run number for the Spring 79 data . Figure 54 b) shows the the same efficiencies as a function of the center of mass energy for all the energy steps taken. Both plots show some quite dramatic changes in measured plane efficiencies. Figure 54 c) has the above results in E_{cm} bins of 20 MeV with many of the short-term variations averaged out. Since in this analysis the whole data sample was divided into 7 energy steps , the efficiencies were averaged over these E_{cm} regions . The results are shown in Table 12 for all the chamber planes. Planes 1-4 (5-8) belong to the inner(outer) spark chambers and planes 9-12 belong to the multiwire proportional chambers.

Chamber efficiencies in [%] for Spring 79 and Spring 80 data								
		Center of mass energy steps						
Layer	Plane	1	2	3	4	5	7	8
1	$\psi_{I.SPC}$	64	78	80	84	77	88	76
2	$\phi_{I.SPC}$	83	84	84	66	84	87	71
3	$\phi_{I.SPC}$	79	84	91	92	91	93	90
4	$\psi_{I.SPC}$	54	77	86	86	84	90	81
5	$\psi_{O.SPC}$	80	82	88	90	90	91	88
6	$\phi_{O.SPC}$	86	90	94	95	94	96	93
7	$\phi_{O.SPC}$	84	84	87	88	88	89	88
8	$\psi_{O.SPC}$	71	70	77	80	82	83	79
9	ψ_{MWPC}	84	85	85	85	84	84	83
10	ϕ_{MWPC}	95	92	97	97	96	96	95
11	ϕ_{MWPC}	97	93	95	96	96	96	96
12	ψ_{MWPC}	89	89	89	90	89	89	88

Table 12 Spark chamber and MWPC efficiencies for different E_{cm}-steps (see Chap.4)
Layer 1-4 (5-8) belong to the inner (outer) spark chamber and Layer 9-12 to the multiwire proportional chamber.

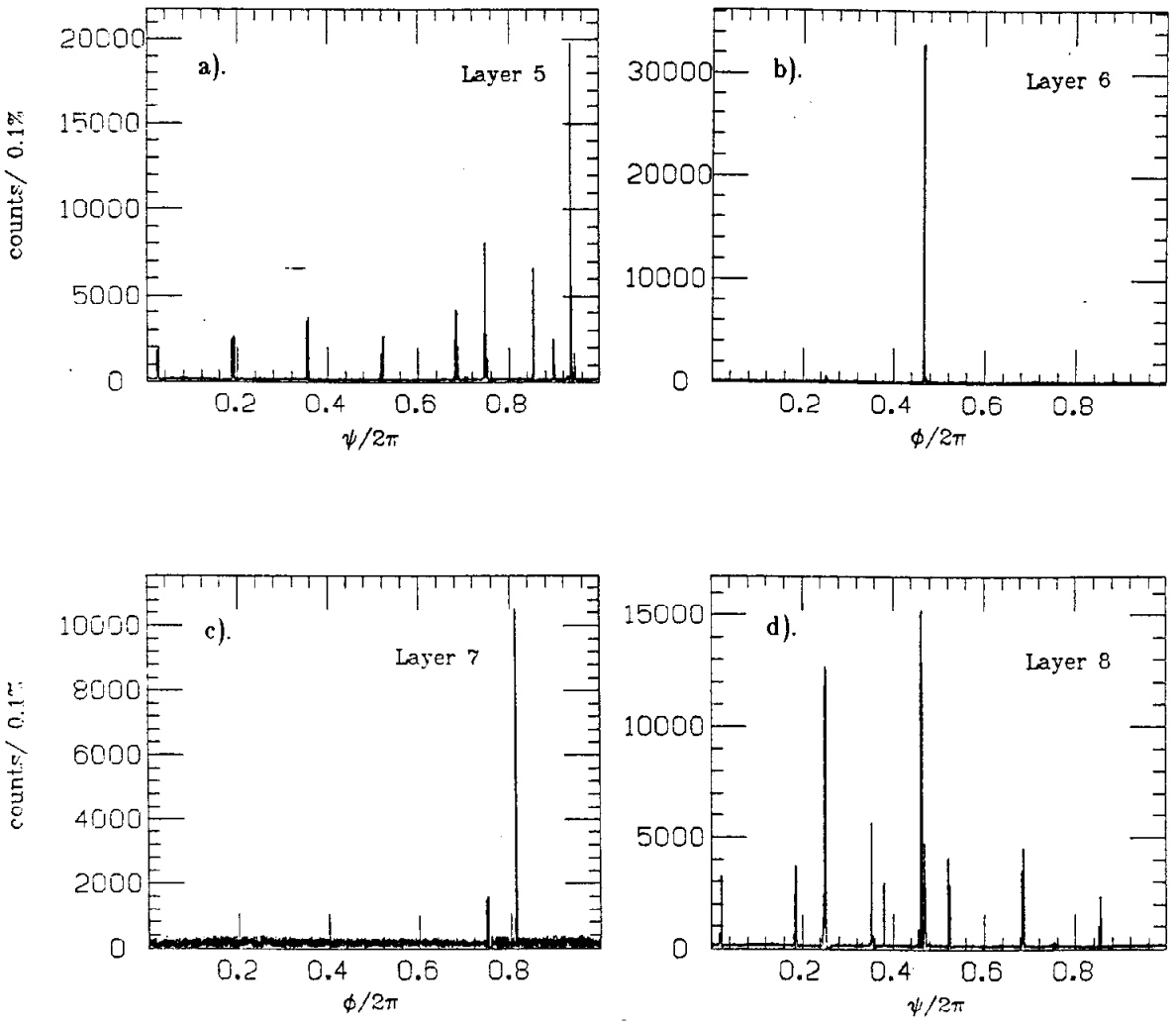

Figure 55. **All hits in outer spark chamber planes showing the localized noise hits. Plots a).-d). correspond to layers 5-8 with the angles ϕ and ψ plotted in units of 2π.**

In additon to measuring the efficiencies for the magnetostrictive spark chambers and the multiwire proportional chambers an attempt was made to remove localized noise hits that occured in the inner and the outer spark chambers. These noise hits can be observed by plotting all the ϕ and ψ hits for each layer. Figure 55 shows as an example all the hits in the two ϕ and the two ψ layers of the outer spark chamber. The horizontal axis is the ϕ or ψ angle in units of 2π. Clearly visible are the strong spikes that indicate the existence of localized noise hits that cannot be due to charged particle tracks . Some of these localized noise hits appear to be very stable over longer periods of time and others seem to wander around. Localized noise hits in the ϕ plane do not necessarily correlate with hits in the corresponding ψ plane although such correlated "hot" spots were observed in the spark chamber set used for the Spring 79 data set. These noise hits were removed from the data by first tracing the "spikes" over the whole data period and then by cutting out these noise hits and retracking the events with the reduced set of chamber hits. The procedure was performed on hadron selected data . The data were ordered chronologically and divided in blocks of 500 events that were interleaved by 250 events. Only regions of the chambers where the number of sparks exceeded the expected number of sparks by a factor of 6 or more were cut out . In a second pass the cuts were used to reanalyse the events disregarding the sparks that lie within the solid angle cut for each plane. Table 13 shows for each of the 8 spark chamber layers the fraction of sparks that were removed in this way together with the fraction of the solid angle that had to be sacrificed. The average solid angle of $\approx 0.65\%$ of 4π that is lost due to this cut is rather small compared to the average layer inefficiencies of $\approx 15\%$. Removing an average of $\approx 14\%$ of the chamber sparks reduces the problem of different $\phi - \psi$ combinations that makes track reconstruction difficult for events with higher charged multiplicity.

Removal of localized noise hits in spark chambers			
Layer	Plane	removed sparks [%]	$\Delta\Omega_{cut}$[% of 4π]
1	$\psi_{I.SPC}$	3.5	0.30
2	$\phi_{I.SPC}$	6.7	0.39
3	$\phi_{I.SPC}$	20.3	0.84
4	$\psi_{I.SPC}$	10.3	0.72
5	$\psi_{O.SPC}$	21.1	1.40
6	$\phi_{O.SPC}$	14.1	0.17
7	$\phi_{O.SPC}$	10.8	0.25
8	$\psi_{O.SPC}$	20.5	1.12

Table 13 Average fraction of sparks and solid angle removed by noise hit cut.

Layer 1-4 (5-8) belong to the inner (outer) spark chamber.

APPENDIX C : NEUTRAL TRACK SEPARATION

In this Appendix a description of the routine GAMFIND[1] is given. The routine was written in order to achieve better separation of neutral tracks among each other than is obtained by the standard offline analysis code. In the standard OFFLINE analysis program the separation of neutral tracks is done at the BUMPS stage as has been described in Chapter 3 . The crucial step in the search for "bumps" of energy depositions that could be accociated with tracks is the suppression of shower fluctuations that could be mistaken as another track. For hadronic showers these shower fluctuations are more erratic than for electromagnetic showers. Since the routine BUMPS has no charged tracking information available an average criterion for the bumps discriminator has to be used as has been described in Chapter 3 . This leads to the situation that the separation of neutral tracks among each other is not as good as might be achieved. The routine GAMFIND was written to separate such merged gammas under the assumption that the neutral energy deposition stems from either one single gamma or two merged gammas. Figure 56 a). shows the histogram obtained by plotting the cosine of the opening angle between all pairs of gammas in events that were analyzed just with the standard offline analysis code. The data used were hadron selected events in the $E_{cm} = 4.0 - 4.5\,\mathrm{GeV}$ region. The cutoff that is observed has a complicated dependence on both

[1] R. Horisberger "Neutral track separation with GAMFIND" Crystal Ball Offline Workshop (August 29- September 2, 1983).

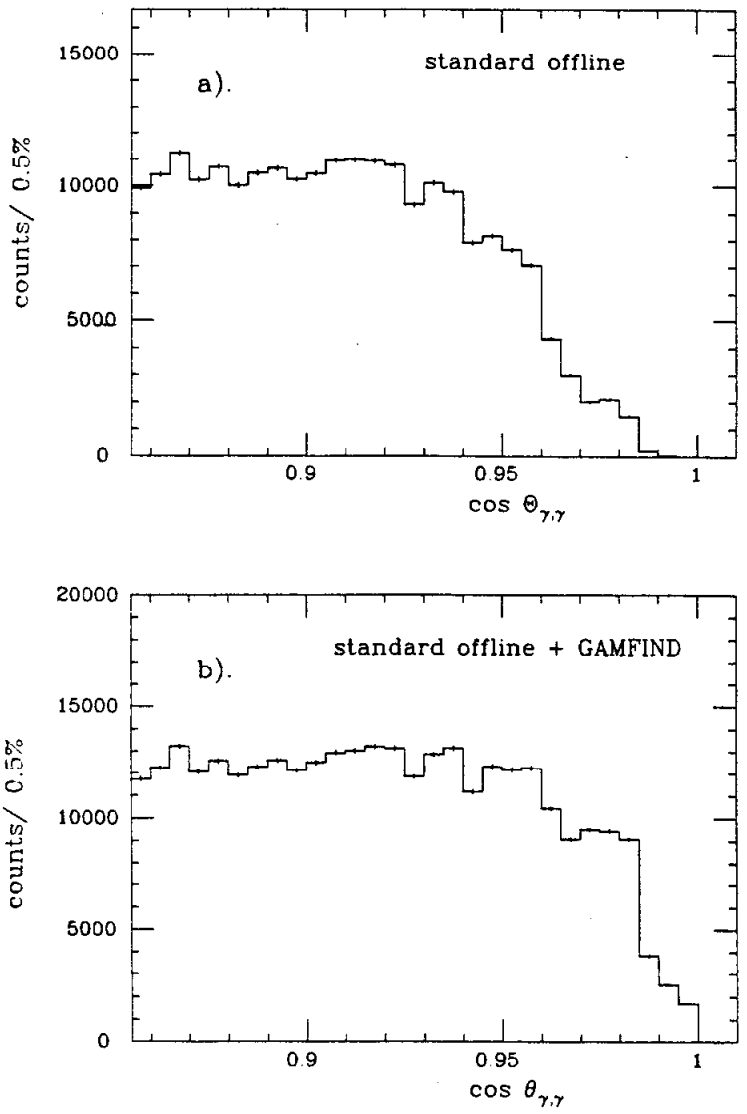

Figure 56. Cosine of average opening angle for all neutral track pairs in a event.

a). events analyzed with standard offline analysis program.

b). events analyzed with standard offline analysis program and GAMFIND.

gamma energies and other bumps in the same connected region and leads to the observed curve when integrated over all track pairs. The curve shows bumps around the cutoff which is a manifestation of the finite crystal segmentation of the NaI(Tl) ball . The cosine of the opening angle with a 50% probabilty for separation is ≈ 0.96 for the standard offline analysis code .

The routine GAMFIND only considers neutral energy depositions which were labled by the offline analysis code as a single photon and which have more than one local maximum in the connected region. This is simply done by checking for each crystal in the connected region that the energy of each of the three nearest neighbour crystals is lower than the the energy of the crystal under investigation. The energy distribution is then fitted to a two photon hypothesis and a one photon hypothesis using the routine PIFIT.[2] This routine returns the log likelihood difference ($\Delta log(L)$) for the two hypotheses , the energies of the two gammas (E_{γ_1},E_{γ_2}) , and the cosine of the opening angle ($cos\theta_{\gamma_1,\gamma_2}$) between them. Using Monte Carlo events , a series of cuts was developed in this 4 dimensional parameter space that attempted to distiguish between the two photon hypothesis and the 1 photon hypothesis . In order to simplify this 4 dimensional cut the photon energies were divided into 6 bins bounded by the energies 0 MeV, 50 MeV, 80 MeV, 160 MeV, 300 MeV, 600 MeV, 5000 MeV . A contour cut for the quantities $\Delta log(L)$ and $cos\theta_{\gamma_1,\gamma_2}$ was then developed for each of the 21 combinations of the two photon energies. The cut was designed so that only few single gammas were lost by labeling a shower fluctuation to be a second gamma.

For the F^*F^* Monte Carlo events that were used for developing the cut only $\approx 1\%$ of the single gammas were misidentified as two photons . The fact that very few "good" gammas are lost due to GAMFIND can also be shown by plotting the invariant mass of all the pairs that can be formed from the corresponding "old offline" gammas and all the other gammas in the event. Figure 57 a). shows the resulting histogram that was obtained from all the data available in the 4 GeV region and the absence of a noticeable π^0 peak at the π^0 mass confirms this.

---

[2] R. Partridge "PIFIT and GAMFIT" Crystal Ball Offline Workshop (August 29- September 2, 1983).

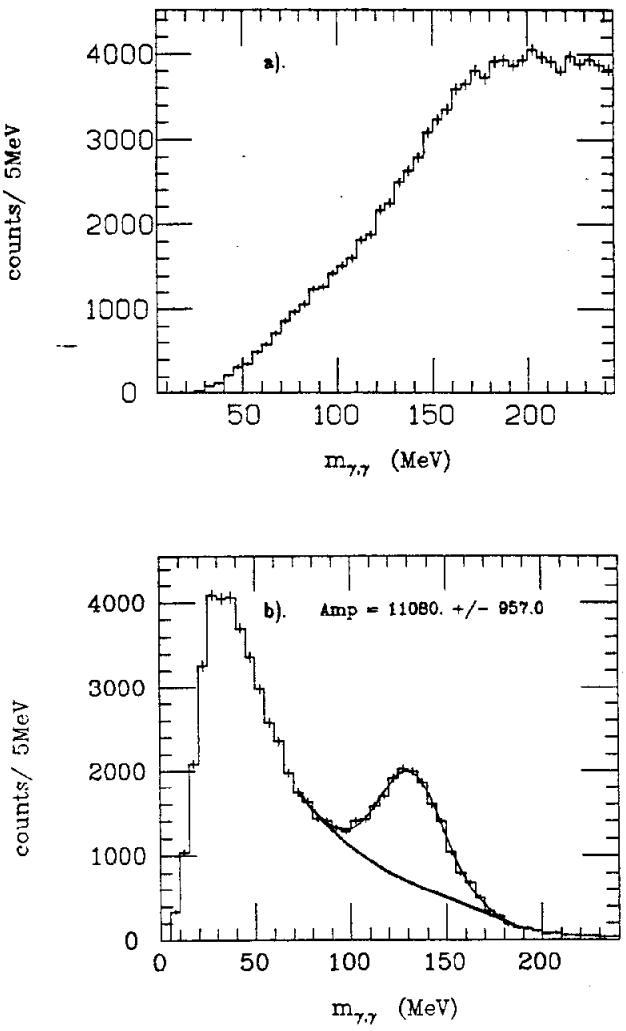

Figure 57. $\gamma\gamma$ invariant mass plots with γ's from GAMFIND.

a). Invariant mass plot from "old offline" gammas (considered by GAMFIND to be 2 gammas) with all other gammas in the event.

No π^0 peak is visible which shows that very few "good" γ's are lost by GAMFIND.

b). Invariant mass plot from pairs of gammas that were found by GAMFIND.

A clear π^0 peak is visible that stems from high energy π^0's.

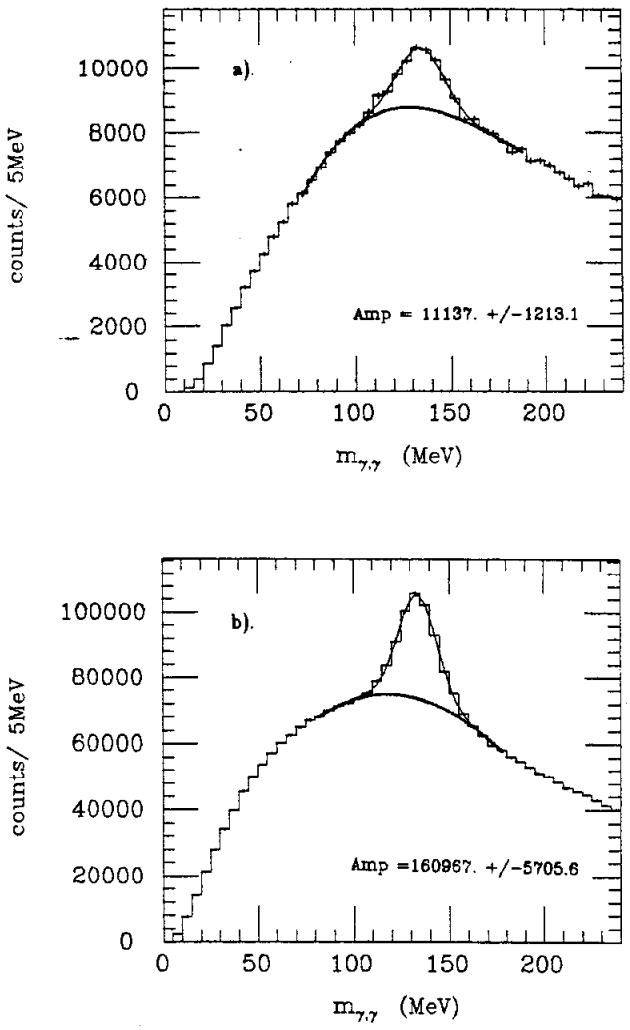

Figure 58. $\gamma\gamma$ invariant mass plots with γ's from GAMFIND.

a). Invariant mass plot from GAMFIND gammas with all other gammas in event.

b). Invariant mass plot of all gamma pairs including GAMFIND gammas.

Once a neutral energy deposition is classified as coming from 2 gammas an energy division routine is applied to obtain the final photon energies and direction cosines. This routine is based on the routine ESORTN[3] but with the difference that the connected region is enlarged with the 12 neighbour crystals around each of the 2 gammas . The energy resolution of gammas obtained from GAMFIND is somewhat worse than for isolated gammas and appears to follow $\approx 3.2\%/E^{1/4}$. Studies on F^*F^* Monte Carlo data indicate that the routine GAMFIND is able to increase the average fraction of gammas per event by $\approx 7-8\%$ depending somewhat on the event multiplicity and with very few gammas being found below 80 MeV in energy. The overlap angle where 50% of the gamma pairs are merged is decreased from $\approx 17.5^0$ to $\approx 11^0$. The fraction of gammas retrieved by GAMFIND in real data can also be obtained by measuring the number of π^0's that can be reconstructed by pairing among each other and with all the other gammas in the event. Figure 57 b). shows the invariant mass plot that is obtained by pairing GAMFIND gammas among each other. A clear π^0 peak is obervable that indicates that some of the merged gamma pairs come from high energy π^0's whose decay gammas had been merged by the OFFINE code . Figure 58 a). shows the invariant mass histogram that is obtained by pairing GAMFIND gammas with all the other gammas in the event. This plot shows a π^0 peak as well indicating that GAMFIND is also able to recover gammas that had been lost due to random overlap with other gammas. Figure 58 b). shows for comparison the invariant mass obtained by pairing all gammas in the event including GAMFIND gammas . Comparing the number of π^0's that were gained with the total number of π^0's found one concludes that GAMFIND is able to increase the number of reconstructable π^0's by $\approx 15\%$ as compared to the standard offline code. Occasionly the routine GAMFIND will also label a neutral track as charged. This occures when the second bump that was suppressed by the standard offline code can be tagged by the hits in the central tracking chambers.

[3] F. Bulos "ESORT" Crystal Ball Offline Workshop (August 29- September 2, 1983).

APPENDIX D : ELECTROMAGNETIC SHOWER PATTERN CUT

This Appendix describes the routine PATCUT that was written in order to distinguish between energy depositions originating from single electromagnetic showers and energy depositions from hadronic showers. The cut is based on the fact that the transverse shower distribution for electromagnetic showers is smaller than for interacting hadrons. Noninteracting hadrons on the other hand only lose energy by dE/dx and produce an energy pattern that has most of its energy in one or two crystals and has therefore a much narrower width than electromagntic showers. In order to cut on the different transverse shower width the two ratios $r_{1,4} = E(\sum 1)/E(\sum 4)$ and $r_{4,13} = E(\sum 4)/E(\sum 13)$ were used. The quantity $E(\sum 1)$ is the energy of the central crystal , $E(\sum 4)$ is the energy of the central crystal and its 3 closest neighbors ,and $E(\sum 13)$ is the energy of the central crystal and its 12 neighbors. The three different energy sums are illustrated in Figure 59. The separation between the different types of energy depositions was done by first identifying which regions in the parameter plane $(r_{1,4}, r_{4,13})$ were mostly populated by electromagnetic showers , hadronic showers and energy patterns from minimum ionizing charged particles and then by cutting along a certain boundary to distinguish single electromagnetic showers from anything else. Since electromagnetic showers have a somewhat more erratic behavior at lower energies than at higher energies the cut was made energy dependent in order to obtain a transmission efficiency (fraction of showers that pass the cut) that is constant for different photon energies. The cuts were developed using a sample of well selected gammas from ψ' cascade events ($\psi' \rightarrow \gamma\chi_{1,2}$ with

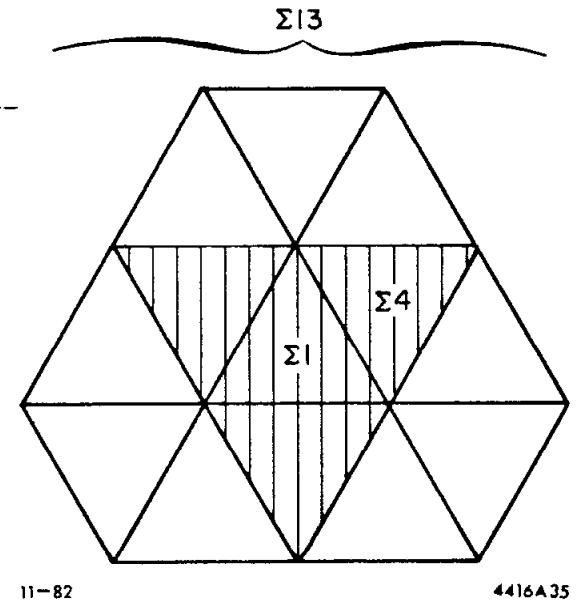

Figure 59. Geometry of the $\sum 13$ Crystal pattern.

$E(\sum 1)$ is the energy of the central crystal (bump module) .

$E(\sum 4)$ is the energy of the central crystal and its 3 nearest neighbors.

$E(\sum 13)$ is the energy of the bump module and the 12 neighbors.

$\chi_{1,2} \rightarrow \gamma\psi$ and $\psi \rightarrow l^+l^-$) that had been selected without using any information about the shower distribution of the cascade photons . This allowed the study of photons with energies of $\approx$ 128 MeV, $\approx$ 172 MeV and $\approx$ 410 MeV . For each of these photon energies the cut was done by plotting the ratios $r_{1,4}$ versus $r_{4,18}$ and requiring that photons lie inside a polygon given by 5 points. In between the three energies of the cascade photons the boundary was linearly interpolated and held constant above 410 MeV and below 128 MeV . Figures 60a),61a),62a) show the ratios $r_{1,4}$ and $r_{4,18}$ obtained from well defined cascade photons for the three different energies mentioned above. Also indicated are the boundaries of the cuts belonging to the three different energies. Figures 60b),61b),62b) show the same plots but for well defined charged tracks (IR-tracks) . The exact values of the polygon points $(r_{1,4}, r_{4,18})$ for the three different photon energies are listed in Table 14 .

Polygon points $(r_{1,4}, r_{4,18})$ used in PATCUT					
	Polygon point				
E_γ[MeV]	1	2	3	4	5
128	0.980,0.989	0.480,0.989	0.480,0.780	0.540,0.660	0.930,0.740
172	0.960,0.980	0.480,0.980	0.480,0.780	0.580,0.620	0.960,0.820
410	0.945,0.989	0.460,0.963	0.460,0.820	0.520,0.660	0.935,0.880

Table 14 Polygon points $(r_{1,4}, r_{4,18})$ used for pattern cut (PATCUT) for the three different energies $E_\gamma = 128, 172, 410$ MeV .

The transmission efficiency of PATCUT for photons has been measured for selected energies using the well defined photons from the cascade events and the slow π^0's from $D^* \rightarrow D + \pi^0$ events. For the four photon energies 67 MeV, 128 MeV, 172 MeV, 410 MeV the measured transmission efficiencies are $0.84 \pm 0.11, 0.87 \pm 0.06, 0.88 \pm 0.04, 0.93 \pm 0.03$. For charged tracks it is easier to obtain the transmission efficiency since it is possible to establish the charged track by the central tracking chamber alone. In Appendix E the transmission efficiencies for charged tracks (IR-tracks) are shown in Figure 63a) as functions of the track energy . The average transmission efficiency is about

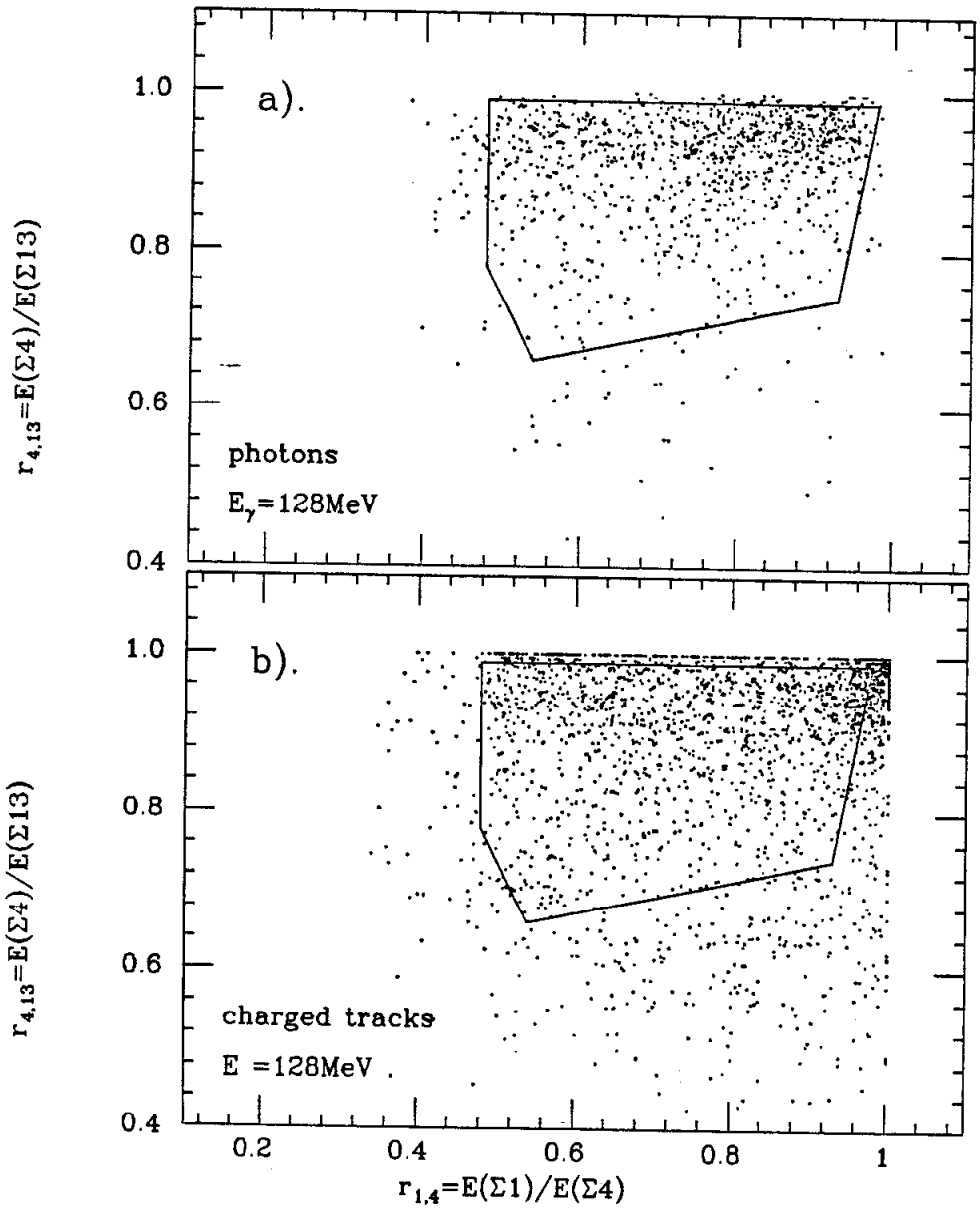

Figure 60. Plot of $r_{1,4}$ versus $r_{4,13}$ for well defined photons and charged tracks with $E_{track} = 128\,\mathrm{MeV}$. a). Well defined γ's from ψ' cascade events ($\psi' \rightarrow \gamma\chi_1$). b). Well defined charged tracks (IR-tracks). Also indicated are the cut boundaries used for selecting photons.

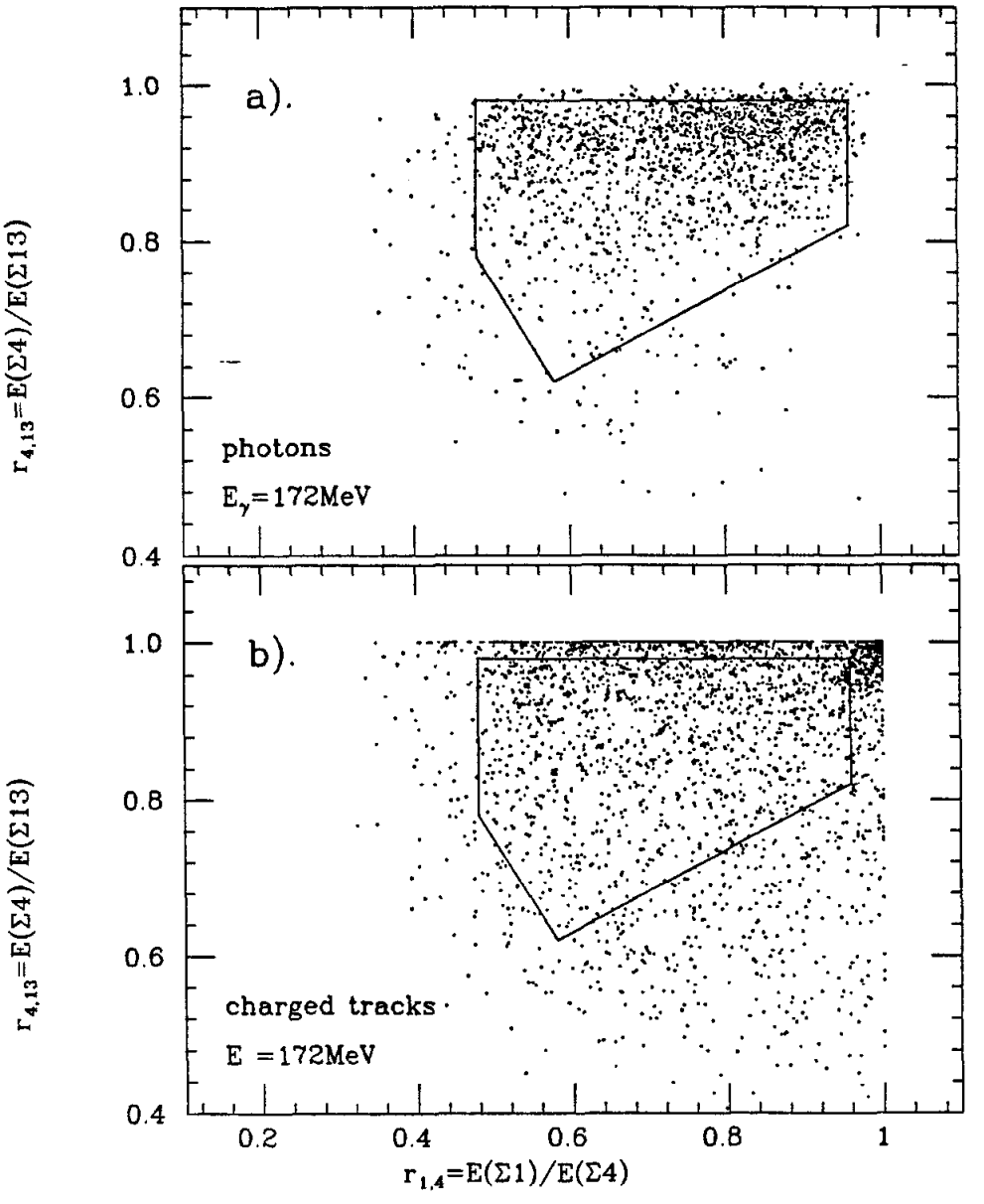

Figure 61. Plot of $r_{1,4}$ versus $r_{4,13}$ for well defined photons and charged tracks with $E_{track} = 172\,\mathrm{MeV}$. a). Well defined γ's from ψ' cascade events ($\psi' \rightarrow \gamma\chi_2$). b). Well defined charged tracks (IR-tracks). Also indicated are the cut boundaries used for selecting photons.

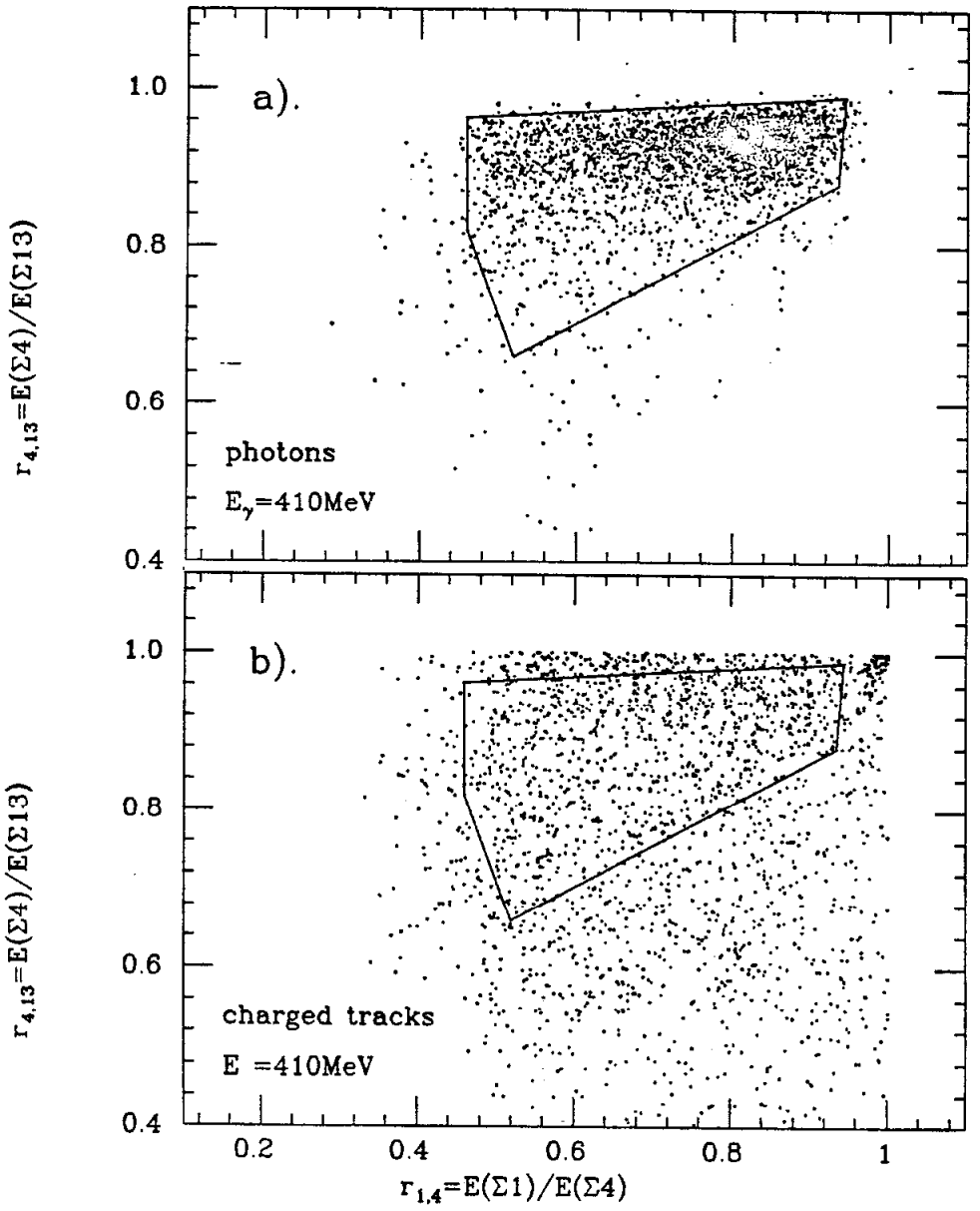

Figure 62. Plot of $r_{1,4}$ versus $r_{4,13}$ for well defined photons and charged tracks with $E_{track} \approx 410\,\mathrm{MeV}$. a). Well defined γ's from ψ' cascade events ($\chi_{1[2]} \rightarrow \gamma\psi$). b). Well defined charged tracks (IR-tracks). Also indicated are the cut boundaries used for selecting photons.

40 – 50% with the typical dip at the minimum ionizing energy . This dip is exploited in the determination of the charged track contamination in the neutral track spectrum as is described in Appendix E.

APPENDIX E : CHARGED TRACK CONTAMINATION IN THE γ SPECTRUM

The neutral track spectrum is contaminated by charged tracks which were not tagged correctly by the charged tracking program. Some of the reasons for these misidentifications have been mentioned in the section describing the routine *BUMPS*.

The measurement of the fraction of charged hadronic tracks in the neutral spectrum is based on the different transmission efficiency of the shower pattern cut for hadronic showers as compared to electromagnetic showers. The transmission efficiencies of the shower pattern cut means the fraction of showers that pass the cut divided by the total number of showers for which the cut was applied. The shower pattern cut used is the routine *PATCUT* which is described in more detail in Appendix D. If one plots the transmission efficiency for charged hadronic showers as a function of the shower energy, one sees a clear dip at an energy of $\approx$ 210 MeV. This occurs at this energy since ,besides the interacting hadronic showers , there are also minimum ionizing tracks that have a totaly different pattern of energy deposition. Minimum ionizing tracks have most of their energy deposited in 1-2 crystals , whereas interacting hadronic showers are wide spread and very irregular. Figure 63a shows the transmission efficiency for charged IR-tracks , obtained with the routine *PATCUT*. IR-tracks represent a clean source of charged tracks . There is virtually no contamination by overtagged γ's .This can be shown by the absence of π^0's in the invariant mass plott which is obtained by pairing IR-tracks with neutral tracks.

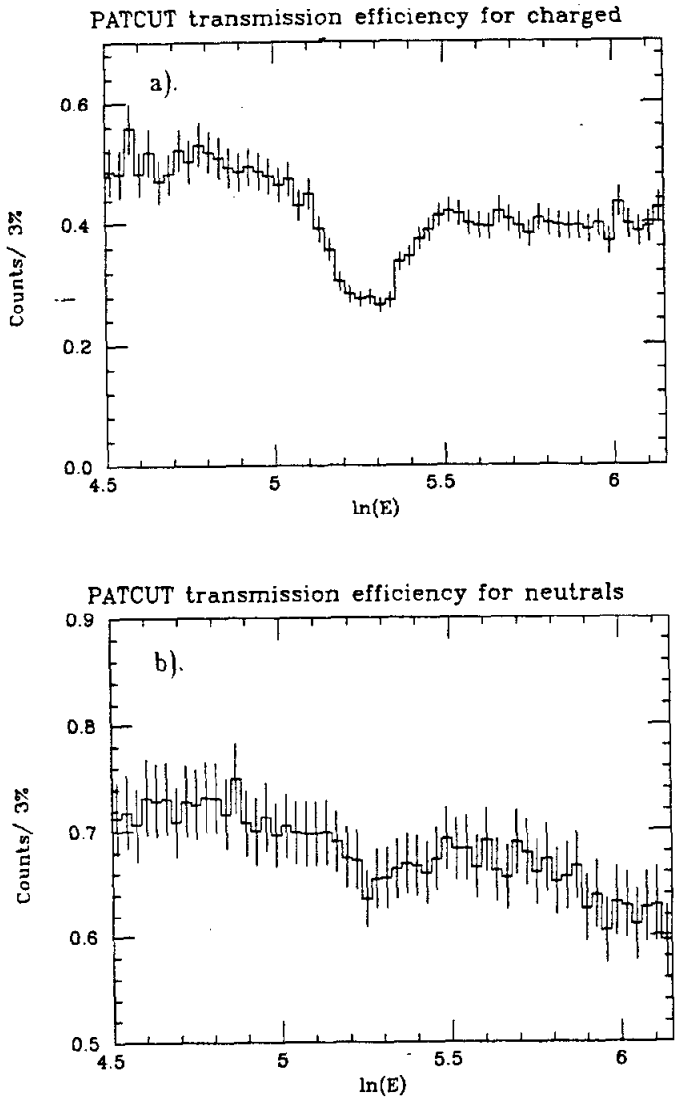

Figure 69. Pattern cut transmission efficiency as a function of the track energy.

a). charged IR-tracks. b). neutral tracks.

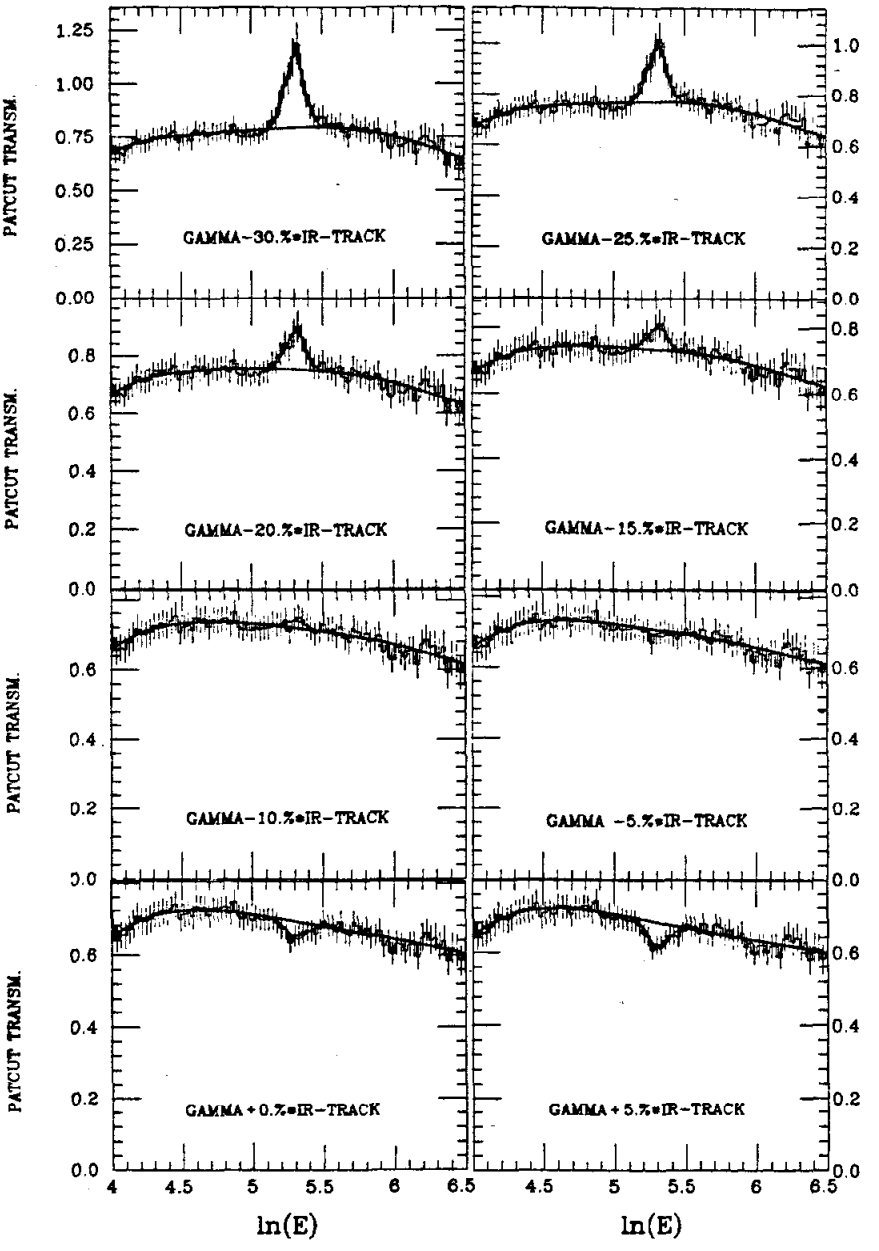

Figure 64. Transmission efficiencies for neutral spectrum with various fractions of charged spectrum subtracted.

The corresponding plot of the transmission efficiency for the observed neutral spectrum is shown in Figure 63b . There is still a small dip visible around an energy of $\approx 210\,\mathrm{MeV}$ that is due to the charged particle track contamination in the neutral spectrum. A pure spectrum of γ's has a smooth transmission curve since the electromagnetic showering process is the same over the whole energy region .

The fraction of charged particle contamination was measured by creating a whole series of plots with an increasing fraction of the charged IR-track spectrum being subtracted from the neutral spectrum. Figure 64 shows the corresponding transmission curves that were obtained for 5% increments. The dips at $E_{track} \approx 210\,\mathrm{MeV}$ were then fit with gaussians of fixed position and width . Finally ,the obtained amplitudes were plotted in Figure 65 , and the zero crosssing was determined. Knowing the relative population of the IR-track spectrum used for subtraction to the neutral spectrum ,one can then obtain the correct charged particle contamination in the neutral track spectrum.

Figures 65-67 were all obtained from the Fall 81 data at $E_{cm} = 4.33\,\mathrm{GeV}$. For this data the fraction of charged particle contamination was determined as $5.2\% \pm 1.4\%$. This number will be used for the analysis of the inclusive γ spectrum at $E_{cm} = 4.33\,\mathrm{GeV}$.

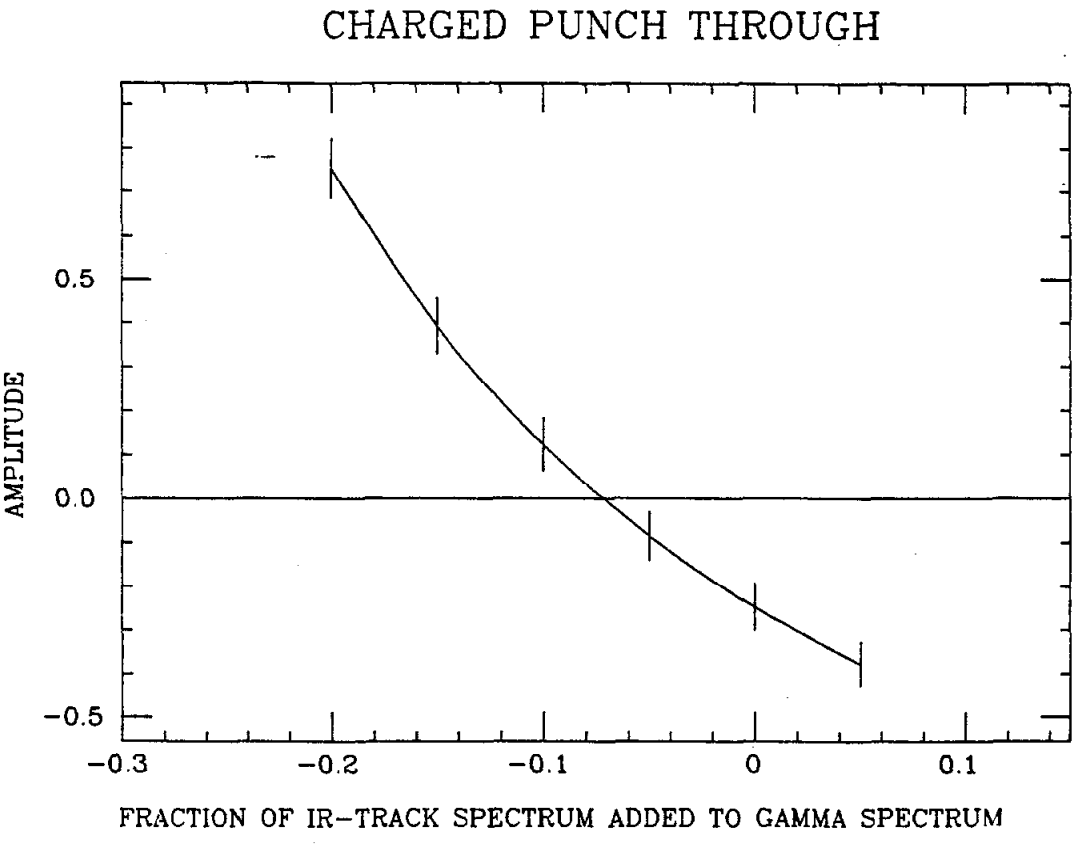

Figure 65. Fit amplitude as a function of the fraction of charged spectrum subtracted from neutral spectrum . The zero crossing allows to calculate the charged "punch through".